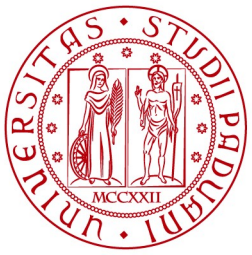

UNIVERSITÀ
DEGLI STUDI
DI PADOVA

Sede Amministrativa: Università degli Studi di Padova

Dipartimento di Scienze Chimiche

---

CORSO DI DOTTORATO DI RICERCA IN: SCIENZE MOLECOLARI

CURRICOLO: SCIENZE CHIMICHE

CICLO XXXVI

# HARNESSING SOLAR LIGHT: LESSONS FROM PHOTOSYNTHESIS FOR BIO-INSPIRED SOLUTIONS

**Coordinatore**: Ch.mo Prof. Stefano Corni

**Supervisore**: Ch.ma Prof.ssa Elisabetta Collini

**Dottorando**: Francesco Tumbarello

# Abstract

Although photosynthetic systems are known for the astonishing efficiency with which they collect and transform sunlight, the molecular mechanisms that regulate photoinduced processes in such systems have only been partially explained. The works described in this thesis aim to deepen our understanding of key events in the biological function of two interesting case studies: the transfer of energy from carotenoids to chlorophylls that occurs in the "antenna" proteins of dinoflagellate algae and the adaptation of the photosynthetic apparatus of alveolate algae to red light. The research was mainly conducted using two-dimensional electronic spectroscopy, a state-of-the-art technique that is particularly suited to the study of crowded systems of chromophores, such as photosynthetic proteins. The analyses performed shed new light on the regulatory mechanisms that allow these systems to survive, even after point mutations or varying environmental conditions. Understanding the strategies underlying the efficiency and robustness of photosynthetic machinery could provide the key to designing bio-mimetic systems able to utilize light energy with better performance than currently available artificial systems. In light of this long-term goal, preliminary investigations on artificial and bio-mimetic systems, designed to exploit light energy in innovative ways, have been carried out using transient absorption spectroscopy.

# Abstract (italiano)

Seppure i sistemi fotosintetici siano noti per la sorprendente efficienza con cui raccolgono e trasformano la luce solare, i meccanismi molecolari che regolano i processi fotoindotti in tali sistemi sono stati spiegati solo in parte. I lavori esposti in questa tesi hanno l'obiettivo di approfondire la conoscenza di eventi chiave nella funzione biologica di due interessanti casi di studio: il trasferimento di energia dai carotenoidi alle clorofille che avviene nelle proteine "antenna" delle alghe dinoflagellate e l'adattamento dell'apparato fotosintetico delle alghe alveolate alla luce rossa. Le ricerche sono state condotte principalmente tramite spettroscopia elettronica bidimensionale, una tecnica allo stato dell'arte che risulta particolarmente adatta allo studio di sistemi con molti cromofori, quali le proteine fotosintetiche. Le analisi effettuate hanno portato alla luce nuovi dettagli sui meccanismi di regolazione che permettono la sopravvivenza di questi sistemi anche a seguito di mutazioni puntuali o a condizioni ambientali variabili. La comprensione delle strategie alla base dell'efficienza e la robustezza dei meccanismi fotosintetici potrebbe fornire la chiave per il design di sistemi biomimetici che riescano ad utilizzare l'energia luminosa con performance migliori rispetto a quelle dei sistemi artificiali attualmente disponibili. Alla luce di tale obiettivo a lungo termine, sono state effettuate delle indagini preliminari, tramite spettroscopia di assorbimento transiente, su sistemi artificiali e biomimetici progettati in modo da sfruttare in modo innovativo l'energia luminosa.

# List of Abbreviations

| | |
|---|---|
| 2DES | Two Dimensional Electronic Spectroscopy |
| 4WM | Four Wave Mixing |
| AOPDF | Acousto-Optic Programmable Dispersive Filter |
| BBO | Beta Barium Borate |
| Car | Carotenoid |
| CCD | Charge-Coupled Device |
| Chl | Chlorophyll |
| CI | Conical Intersection |
| CLH | Chromera Light Harvesting |
| CP | Cross Peak |
| DAS | Decay-Associated Spectrum |
| DOE | Diffractive Optical Element |
| DSM | Donut-shaped Spherical Mirror |
| ESA | Excited State Absorption |
| ET | Energy Transfer |
| FCP | Fucoxanthin Chlorophyll a/c-binding Protein |
| FROG | Frequency Resolved Optical Gating |
| FTO | Fluorine-doped Tin Oxide |
| FWHM | Full Width at Half Maximum |
| GSB | Ground State Bleaching |
| ICT | Intramolecular Charge Transfer |
| Ifx-l | Isofucoxanthin-like |
| LH | Light Harvesting |
| LO | Local Oscillator |
| NCG | Non-Conductive Glass |
| NOPA | Non-collinear Optical Parametric Amplifier |

| | |
|---|---|
| NR | Non Rephasing |
| OPE | Oligophenylenethylene |
| PCP | Peridinin Chlorophyll *a* Protein |
| Per | Peridinin |
| QNC | Quinacridone |
| R | Rephasing |
| RC | Reaction Center |
| rCLH | red CLH |
| RF | Rotating Frame |
| RFPCP | Refolded PCP |
| RWA | Rotating Wave Approximation |
| sCMOS | scientific Complementary Metal-Oxide Semiconductor |
| SE | Stimulated Emission |
| T | Total |
| TA | Transient Absorption |
| TL | Transform Limited |
| TPP | Tetraphenylporphyrin |
| Vlx | Violaxanthin |
| WT | Wild-Type |

# Contents

# Chapter 1

# Introduction

Every year, the Sun irradiates Earth with millions of exajoules (1 EJ = $10^{18}$ J) of light energy [1]. This enormous amount of energy exceeds of several orders of magnitude the world primary energy consumption, which, in 2022, was slightly above 600 EJ [2]. Basically, harnessing sunlight alone could put an end to humanity's energy problem. Despite this optimistic vision, converting solar energy into forms that can be easily employed by humans is not that simple. Indeed, the most recent reports have shown that the energy generated starting from the Sun accounts for no more than a few percent of the energy consumed annually [2]. Firstly, solar energy is mainly used after being converted into electricity in photovoltaic panels, the most common of which exhibit conversion efficiencies that hardly reach 20% [3]. Moreover, human activities require energy to be concentrated in only a few places on Earth's surface and continuously available, whereas the sun is an intermittent source, subject to alternating night and day and fluctuating weather conditions. There are two possible approaches to improving the performance of technologies based on the use of solar energy, including photovoltaics. On the one hand, we can continue working on optimizing the performance of the devices currently in use, effort that has enabled great progress to be made in this field over the years, leading to the improvement of technologies that are part of our lives [4, 5]. On the other hand, however, we can wonder what alternatives there are, in other words, whether devices based on different premises can be developed.

One possible answer in this regard is: how does nature harness solar energy? The natural systems that more directly exploit solar energy are photosynthetic organisms: plants, algae and cyanobacteria produce the nutrients essential for their survival starting

from sunlight, water and $CO_2$. In photosynthetic organisms, the complex sequence of events that converts solar energy into biochemical fuels begins with the photo-oxidation of the chlorophylls (Chls) of the Reaction Centers (RCs). However, only a negligibly small amount of the light energy needed for this photoactivated process is collected directly by the RCs. The duty of absorbing light is entrusted to specialized antenna proteins, called Light Harvesting (LH) complexes, which capture light in a wide spectral range by binding rich pools of pigments. Among these, Chls often play the main role, but also other "accessory" pigments, such as carotenoids (Cars), are co-present in these antennae to ensure photoprotection and capture blue-green light, which Chls poorly absorb [6]. In order for the absorbed light to be converted into chemical energy, the LH complexes must then transfer the excitation to the Chls of the RCs. This is done by exploiting a downward energy gradient: the excitation collected in different regions of the visible spectrum is transferred to electronic states at progressively lower energy via a series of Energy Transfer (ET) steps culminating in the low-energy Chls of the RC. This is done in less than a billionth of a second and with >90% efficiencies [7].

With the goal of adapting natural strategies for manipulating light energy to artificial devices, the first obstacle encountered is our insufficient knowledge of the finely tuned machinery that photosynthetic systems employ to transport and convert light. To gain a deeper understanding of this field, we should be able to follow and characterize phenomena occurring on time scales that, as mentioned, may be in the picoseconds ($10^{-12}$ s) or femtoseconds ($10^{-15}$ s) domains. Moreover, photosynthetic antennae are extremely delicate macromolecular assemblies, which may lose their structural - and therefore functional - characteristics if the sensitive network of interactions that holds them up is perturbed. Any investigation must therefore be as unobtrusive as possible in order to obtain results that reflect the native features of such systems.

To investigate how excitation is transferred between the pigments of a photosynthetic antenna, we can use the very property that defines the function of pigments: their interaction with light. Light proves to be an extremely respectful investigative tool and enables to follow, even in real time, the dynamics of the excited states. Technological advancement has led to the generation of light pulses of increasingly shorter duration, down to femtoseconds and even attoseconds ($10^{-18}$ s) [8, 9], unleashing time resolutions that allow us to decode the details of the electronic structure of atoms and molecules and to map the paths traveled by excitation also in complex systems. Two-Dimensional

Electronic Spectroscopy (2DES) stands out as one of the most promising spectroscopic techniques, delivering compelling results in the study of photosynthetic systems over the past two decades. [10, 11, 12]. In a 2DES experiment, the response of a sample to a sequence of light pulses of ∼10 fs duration is detected; this time resolution has turned out to be typically sufficient to observe the cooling of excitation through manifolds of electronic and vibrational states and energy exchanges between pigments. The 2DES response is in the form of two-dimensional frequency-frequency spectra from which the spectroscopic information can be extracted more easily than from a one-dimensional spectrum, simplifying the interpretation of signals produced by complexes that may easily contain tens of pigments. Chapter 2 of this thesis briefly describes the theoretical background underlying 2DES and the more popular Transient Absorption (TA) spectroscopy, which I used in parallel with 2DES during my PhD. Chapter 3, instead, addresses the experimental setups through which 2DES and TA are implemented in our laboratory.

The following chapters present the results of investigations on biological antennae that were considered particularly interesting for the peculiar strategies to exploit sunlight. Chapter 4 is focused on Peridinin Chlorophyll *a* Protein (PCP) [13, 14], an antenna that allows the survival of dinoflagellate algae in underwater environments, enriched in blue-green light, by binding a pigment cluster in which Cars outnumber Chls. The energy absorbed by the Cars is immediately transferred to the Chls via an ET process that has aroused the most curiosity in the study of photosynthesis for its remarkable optimization and still unclear mechanisms. PCP exemplifies how nature was able to build a multi-chromophoric complex refined to work under peculiar light conditions with a slow process of evolutionary selection. On the other hand, some photosynthetic systems are able to adapt their antennae apparatus in response to variations in ambient light on time scales of days or hours, a process called chromatic adaptation [15]. The alveolate alga *Chromera Velia* (*C. velia*) gives an elegant example of this, by expressing far-red absorbing antennae when cultivated under red light [16]. In *C. velia*, the acclimation to light changes seems to occur by exploiting different tactics from those, more documented and understood, of other organisms, as discussed in Chapter 5.

Overall, these investigations attempt to unveil the energetic and structural requirements that enable photosynthetic systems to harness sunlight so efficiently, with the

ultimate aim of assessing whether similar strategies could be implemented in artificial systems for the conversion of solar energy. This aim cannot be achieved without acknowledging the main potentiality and challenges of such systems. In my PhD project, the study of biological systems was therefore flanked by spectroscopic investigations of artificial systems designed to capture and exploit light energy. Chapter 6 presents preliminary characterizations of two systems that were found to be particularly interesting from this perspective: dye-sensitized photoanodes capable of using visible light to trigger chemical reactions [17] and self-assembling functionalized porphyrins designed to mimic the ability of natural systems to transport excitation along specific paths [18].

# Chapter 2

# Theory

This chapter examines the theoretical foundations of the spectroscopic methods applied for the research work presented in this thesis. The formalism that will be presented is the one proposed by Mukamel [19] and based on the semi-classical approach and the time-dependent perturbation theory for the light-matter interaction. A full treatment is beyond the scope of this thesis and can be found in several books [20, 21, 22, 23, 24] and papers [25, 26].

First, the semiclassical approach will be introduced and the difference between linear and non-linear spectroscopies will be clarified. Then, a significant portion of the following sections will focus on the density operator, which is the most convenient operator for the description of macroscopic ensembles. After defining it, the equations that express its temporal evolution will be discussed. In this way, it will be possible to describe, at the microscopic level, what happens in a sample when it interacts with light. Finally, third-order optical phenomena, on which TA and 2DES are based, will be presented.

## 2.1 Light-Matter Interaction

A typical spectroscopic problem requires the description of the interaction between a sample and an electromagnetic wave. In a fully quantum treatment, the Hamiltonian operator of the macro-system formed by the sample and the electromagnetic radiation would include the sample term $\hat{H}_S$, the light field term $\hat{H}_L$ and a term $\hat{H}_{SL}$ accounting

for the interaction between the two:

$$\hat{H} = \hat{H}_S + \hat{H}_L + \hat{H}_{SL} \tag{2.1}$$

The solution of the full quantum problem would require simultaneously accounting for the degrees of freedom of both matter and light, which may be a difficult task even for simple systems. However, given the high number of photons emitted by the sources commonly used in spectroscopy, the light field interacting with the sample tends to the classical limit; in addition, the wavelength of the radiations employed is considerably greater than the typical atomic distances, making the spatial dependence of the electromagnetic field negligible. Therefore, a classical description of the electromagnetic radiation based on Maxwell's equations is convenient, while maintaining a quantum description of the sample. Within the framework of this semi-classical approximation, the total Hamiltonian is thus

$$\hat{H} = \hat{H}_S + \hat{H}_{SL} \tag{2.2}$$

To understand what happens in a material as a consequence of the interaction with the electric field, it is useful to imagine the matter as a collection of interacting charged particles that are perturbed by the presence of an electromagnetic wave. Permanent dipoles are reoriented and induced dipoles are formed to minimize the interaction energy between the electric field and the particles. At a macroscopic level, this causes the generation of a net dipole moment, that is, a polarization $\vec{P}$. In the most general case, the polarization should be written as an expansion in powers of the electric field $\vec{E}$:

$$\vec{P} = \epsilon_0 \left( \chi^{(1)} \cdot \vec{E} + \chi^{(2)} : \vec{E}\vec{E} + \chi^{(3)} : \vec{E}\vec{E}\vec{E} + \dots \right) = \vec{P}^{(1)} + \vec{P}^{(2)} + \vec{P}^{(3)} \dots \tag{2.3}$$

where $\chi^{(n)}$ and $\vec{P}^{(n)}$ are the n$^{th}$-order electric susceptibility and polarization and $\epsilon_0$ is the dielectric constant in vacuum (hereafter the vector notation will be omitted for simplicity). In isotropic media, like solutions, all even-order susceptibilities vanish, so the lowest order nonlinearity is the third order one. If the excitation comes from a source of ordinary intensity, the expansion in Eqn. 2.3 can be truncated at the linear term. The linear polarization is responsible for the phenomena of refraction and reflection, as well as absorption of radiation. When the incoming electric fields are intense, like those generated by laser sources, the non-linear terms of Eqn. 2.3 become non-negligible. Non-linear effects may be used to manipulate the properties of light. For example, the second order polarization of non-isotropic media, such as $\beta$-barium borate (BBO) crystals, can

be employed to double the frequency of a light beam, or to mediate the interaction between light beams, generating light with new frequencies and amplitudes. Moreover, the non-linear polarization is at the base of a series of spectroscopic techniques that have several advantages with respect to the linear experiments, like the possibility to observe couplings between states and characterize processes which are more complex than simple absorption [19, 20].

As the electric field of the electromagnetic wave is oscillating, the polarization itself is modulated in time, resulting in a net motion of charges in time. The time-dependent polarization $P(t)$ thus acts as a source of an electromagnetic field, as predicted by Maxwell's equations. This field is the spectroscopic signal $E_{sig}(t)$, which, according to classical electrodynamics, is 90° phase shifted with respect to the macroscopic polarization:

$$E_{sig}(t) \propto iP(t) \tag{2.4}$$

Describing the spectroscopic signal in terms of a field emitted by the sample seems counter-intuitive when discussing phenomena like the simple absorption of radiation. However, one can think of absorption as a process in which the signal emitted by the sample cancels out the light transmitted by the sample, being out of phase with it, thus causing a decrease in transmittance [22].

The semi-classical approach splits the description of the spectroscopic problem into two steps. The first step is the calculation of the polarization, which can be done quantum-mechanically as illustrated in the following sections; once the polarization is known, it is connected to the signal by classical electrodynamics, as summarized in Eqn. 2.4.

## 2.2 Quantum Mechanical Calculation of the Polarization

In the previous section, the polarization was defined as a net dipole moment in a macroscopic sample. In quantum-mechanical terms, the polarization is the expectation value of the dipole moment operator $\hat{\mu}$:

$$P(t) = \langle \hat{\mu}(t) \rangle \tag{2.5}$$

The expectation value acts as a bridge between microscopic world and macroscopic observation, but its estimate depends on how the system is described at the microscopic level.

The most common description of quantum systems (atoms, molecules,...) relies on the time-dependent wavefunction $\psi(t)$. In absence of radiation, the (semi-classical) total Hamiltonian of Eqn. 2.2 coincides with the system Hamiltonian $\hat{H}_S$; the eigenstates of $\hat{H}_S$ ($|0\rangle$, $|1\rangle$, $|2\rangle$,..., with energies $E_0$, $E_1$, $E_2$,...) can be used as a basis of the quantum-mechanical space and the wavefunction can be written as a linear combination of them:

$$|\psi(t)\rangle = \sum_n c_n(t)\,|n\rangle \tag{2.6a}$$

$$\langle\psi(t)| = \sum_n c_n^*(t)\,\langle n| \tag{2.6b}$$

Here the Dirac notation is employed, with the wavefunction $\psi(t)$ written as the ket $|\psi(t)\rangle$ and its complex conjugated $\psi^*(t)$ written as the bra $\langle\psi(t)|$. The system may be in the ground state ($|\psi\rangle \propto |0\rangle$) or in an excited state ($|\psi\rangle \propto |1\rangle, |2\rangle, ...$). Alternatively, the system may be in a superposition state; for example, it could be described by a superposition of the ground and the first excited state:

$$|\psi(t)\rangle = c_0(t)\,|0\rangle + c_1(t)\,|1\rangle \tag{2.7}$$

The square moduli of the coefficients $c_0(t)$ and $c_1(t)$ represent the probability to obtain $E_0$ and $E_1$ upon measurement of energy. Finally, the expectation value can be calculated as

$$\langle\hat{\mu}(t)\rangle = \langle\psi(t)|\hat{\mu}|\psi(t)\rangle = \int d\boldsymbol{x}\psi^*(t)\hat{A}\psi(t) \tag{2.8}$$

where $\boldsymbol{x}$ are the spatial coordinates.

The wavefunction formalism is adequate to describe a single quantum system or a pure state, that is, a collection of replicas of a quantum system that are all in the same state and are thus characterized by a single $|\psi(t)\rangle$. However, in the condensed phase it is common to deal with a macroscopic ensemble of quantum systems in different states, called mixed state. It is clear that Eqn. 2.8 cannot be used to calculate the expectation value in this case, as there is not a single $|\psi(t)\rangle$ that describes the ensemble completely. The determination of an expectation value in a mixed state can be performed more conveniently by using the density operator $\hat{\rho}(t)$. This has a very useful property: the

expectation value of a physical observable can be calculated as the trace of the product between the operator corresponding to that observable and the density operator itself. In the case of the polarization:

$$\langle \hat{\mu}(t) \rangle \propto Tr \{ \hat{\mu} \hat{\rho}(t) \} \tag{2.9}$$

The density operator contains information on a macroscopic ensemble and its time evolution during the spectroscopic experiment. Once the density operator of the system is known, the calculation of the polarization is straightforward.

### 2.2.1 Density Operator Dynamics in the Absence of Radiation

In a mixed state, each molecule of the ensemble has a probability $P^{(k)}$ to be found in a certain quantum state $|\psi^{(k)}(t)\rangle$ described by the wavefunction

$$|\psi^{(k)}(t)\rangle = \sum_n c_n^{(k)}(t) \, |n\rangle \tag{2.10}$$

The various states $|\psi^{(k)}(t)\rangle$ differ for the coefficients $c_n^{(k)}(t)$ of the linear combination. Such an ensemble can be conveniently represented by using the formalism of the density operator $\hat{\rho}(t)$, defined as

$$\hat{\rho}(t) = \sum_k P_k \, |\psi^{(k)}(t)\rangle \, \langle \psi^{(k)}(t)| \tag{2.11}$$

The density operator can be expressed as a matrix based on the eigenstates of the Hamiltonian:

$$\hat{\rho}(t) = \begin{pmatrix} \rho_{00}(t) & \rho_{01}(t) & \dots \\ \rho_{10}(t) & \rho_{11}(t) & \dots \\ \vdots & \vdots & \ddots \end{pmatrix} \tag{2.12}$$

with elements

$$\rho_{nm}(t) = \sum_k P^{(k)} c_n^{(k)}(t) c_m^{(k)*}(t) \tag{2.13}$$

Diagonal terms $\rho_{nn}(t)$ represent populations in the various energy levels of the system; off-diagonal terms $\rho_{nm}(t)$ are called coherences and represent superpositions between couples of states. For example, a superposition like the one in Eqn. 2.7 is associated with coherences $\rho_{01}$ and $\rho_{10}$.

If the density matrix at an initial time $t_0$ is known, the density matrix at any succeeding instant $t$ can be determined by solving the Liouville-Von Neumann equation:

$$\frac{\partial}{\partial t}\hat{\rho}(t) = -\frac{i}{\hbar}\left[\hat{H}, \hat{\rho}(t)\right] \tag{2.14}$$

It is useful to consider, in the first place, the evolution in the absence of radiation. The total Hamiltonian $\hat{H}$ coincides with the system Hamiltonian $\hat{H}_S$, which is generally time-independent, and the solution of Eqn. 2.14 is in the form:

$$\hat{\rho}(t) = \hat{U}_S\left(t, t_0\right)\hat{\rho}\left(t_0\right)\hat{U}_S^{\dagger}\left(t, t_0\right) \tag{2.15}$$

where $\hat{U}_S(t, t_0)$ is the time-evolution operator, which propagates the system from time $t_0$ to time $t$ under the effect of $\hat{H}_S$. Considering a two-level system composed of ground state $|0\rangle$, with energy $E_0$, and excited state $|1\rangle$, with energy $E_1$, the time-evolution operator can be written as

$$\hat{U}_S\left(t, t_0\right) = e^{-i\frac{\hat{H}_S}{\hbar}(t-t_0)} = \begin{pmatrix} e^{-i\frac{E_0}{\hbar}(t-t_0)} & 0 \\ 0 & e^{-i\frac{E_1}{\hbar}(t-t_0)} \end{pmatrix} \tag{2.16}$$

Under the effect of $\hat{H}_S$, the density matrix of the two-level system evolves in time as follows:

$$\begin{aligned} \hat{\rho}(t) &= \begin{pmatrix} e^{-i\frac{E_0}{\hbar}(t-t_0)} & 0 \\ 0 & e^{-i\frac{E_1}{\hbar}(t-t_0)} \end{pmatrix} \begin{pmatrix} \rho_{00}(t_0) & \rho_{01}(t_0) \\ \rho_{10}(t_0) & \rho_{11}(t_0) \end{pmatrix} \begin{pmatrix} e^{i\frac{E_0}{\hbar}(t-t_0)} & 0 \\ 0 & e^{i\frac{E_1}{\hbar}(t-t_0)} \end{pmatrix} \\ &= \begin{pmatrix} \rho_{00}(t_0) & \rho_{01}(t_0)e^{i\omega_{10}(t-t_0)} \\ \rho_{10}(t_0)e^{-i\omega_{10}(t-t_0)} & \rho_{11}(t_0) \end{pmatrix} \end{aligned} \tag{2.17}$$

with $\omega_{10} = (E_1 - E_0)/\hbar$. According to Eqn. 2.17, diagonal and off-diagonal elements of the density matrix show different time dependences: populations remain constant in time, whereas coherences oscillate with frequency proportional to the energy separation between the two states.

If the expression of the density matrix just found is inserted into Eqn. 2.9, the polarization results:

$$\hat{\mu}\hat{\rho}(t) = \begin{pmatrix} 0 & \mu_{01} \\ \mu_{10} & 0 \end{pmatrix} \begin{pmatrix} \rho_{00}(t) & \rho_{01}(t) \\ \rho_{10}(t) & \rho_{11}(t) \end{pmatrix} = \begin{pmatrix} \mu_{01}\rho_{10}(t) & \mu_{01}\rho_{11}(t) \\ \mu_{10}\rho_{00}(t) & \mu_{10}\rho_{01}(t) \end{pmatrix}$$

$$P(t) \propto Tr\left\{\hat{\mu}\hat{\rho}(t)\right\} = \mu_{01}\rho_{10}(t_0)e^{-i\omega_{10}(t-t_0)} + \mu_{10}\rho_{01}(t_0)e^{i\omega_{10}(t-t_0)} \tag{2.18}$$

Hence, only oscillating coherences give rise to a macroscopic polarization and emit a light field, just as in the classical description, the net oscillation of charges caused by the electric field is responsible for the emission of the signal.

In an ensemble at thermal equilibrium, populations follow the Boltzmann distribution and there are no coherences, therefore the equilibrium density matrix assumes a diagonal form:

$$\hat{\rho}_{eq} = \frac{1}{Q}\begin{pmatrix} e^{-E_0/k_BT} & 0 & \dots \\ 0 & e^{-E_1/k_BT} & \dots \\ \vdots & \vdots & \ddots \end{pmatrix} \tag{2.19}$$

where $Q$ is the partition function $Q = \sum_n e^{-E_n/k_BT}$. Due to the absence of coherent superpositions, as expected, no spectroscopic signal is emitted by an ensemble at equilibrium.

As it will be demonstrated in the following sections, when the system is subjected to a light field, the latter drives the ensemble out of equilibrium, changing the populations and generating coherences. Once the field is turned off, in absence of other effects, populations would remain out of equilibrium and the new generated coherences would oscillate under the effect of $\hat{H}_S$ *ad infinitum*. However, a crucial aspect has been so far ignored: the interaction between the ensemble and its bath causes the relaxation back towards the equilibrium condition; the effect of the bath is superimposed on the time evolution caused by the Hamiltonian $\hat{H}_S$ and can be incorporated via relaxation parameters [23]. Populations relax to their equilibrium value with a time constant $T_1$:

$$\rho_{nn}(t) = \rho_{nn,eq} + \left[\rho_{nn}\left(t_0\right) - \rho_{nn,eq}\right] e^{-(t-t_0)/T_1^{(nn)}} \tag{2.20}$$

where $T_1^{(nn)}$ is the relaxation time characteristic of state $|n\rangle$. In Eqn. 2.20, as well as in the rest of this chapter, it is assumed for simplicity that the temporal evolution of the populations can be described by single exponential functions; more generally, the evolution of populations can be multi-exponential, as will be seen in Chapters 4-6. In contrast to populations, coherences, while oscillating under the effect of $\hat{H}_S$, are progressively damped to zero as a result of fluctuating interactions with the bath. This phenomenon, known as homogeneous dephasing, is captured by the time constant $T_2$.

If $T_2^{(nm)}$ is the dephasing time constant of the coherence $\rho_{nm}$:

$$\rho_{nm}(t) = \rho_{nm}(t_0)\, e^{-i\omega_{nm}(t-t_0)} e^{-(t-t_0)/T_2^{(nm)}} \tag{2.21}$$

Different phenomena contribute to homogeneous dephasing, as summarized in the following equation:

$$\frac{1}{T_2} = \frac{1}{2T_1} + \frac{1}{T_2^*} \tag{2.22}$$

The term associated with population relaxation $1/2T_1$ refers to the amplitude decay of the coherence as a result of the finite lifetime of the excited state(s) involved in the superposition. The term $1/T_2^*$, instead, represents the contribution of pure-dephasing, namely the gradual loss of the phase relationships of oscillations among the members of the ensemble as a result of molecular interactions (collisions, fluctuations induced by the solvent,...).

As highlighted by the description given above, homogeneous dephasing is a dynamic effect. However, it should also be taken into account that the existence of slightly different local environments around the molecules spreads the transition frequencies on a distribution of width $\Delta$. Such a static frequency distribution is the origin of inhomogeneous dephasing, which causes the damping of coherences with a gaussian trend:

$$\rho_{nm}(t) = \rho_{nm}(t_0)\, e^{-i\omega_{nm}(t-t_0)} e^{-\Delta^2 (t-t_0)^2/2} \tag{2.23}$$

Every system of the ensemble has an instantaneous frequency $\omega_i(t)$ which evolves in time due to the interaction with the surroundings, causing the phenomenon known as spectral diffusion. Homogeneous and inhomogeneous dephasing can be thought as limiting regimes for the fluctuations of a frequency $\omega_i(t)$ through a distribution of frequencies of width $\Delta$. Every real system lies between these two limits [27].

So far, the behavior of a system at equilibrium has been described, as well as the relaxation of a perturbed system to the equilibrium condition. What is still missing is the description of the evolution of the ensemble when an interaction with the light field takes place. For a molecule with no net charge, the interaction Hamiltonian can be written as

$$\hat{H}_{SL}(t) = -\hat{\mu} E(t) \tag{2.24}$$

where $\hat{\mu}$ is the component of the dipole moment operator parallel to the electric field.

To describe the evolution of the density matrix during the interaction with the electromagnetic wave, the Liouville-Von Neumann equation with a time-dependent total Hamiltonian $\hat{H}(t) = \hat{H}_S + \hat{H}_{SL}(t)$ should be solved. However, it is more convenient to perform a perturbative expansion of the density operator.

### 2.2.2 Density Operator Dynamics in the Presence of Radiation

In general, the interaction with an electric field is much weaker than the internal fields of the molecule and can therefore be treated as a perturbation of the energy of the system. In a perturbative approach, the eigenstates $|n\rangle$ of the Hamiltonian $\hat{H}_S$ are still considered eigenstates of the total Hamiltonian $\hat{H}(t)$ and used as base of the quantum space. The density matrix can be expressed with a perturbative expansion in which the unperturbed density matrix $\hat{\rho}^{(0)}$ (which is equal to $\hat{\rho}_{eq}$ if the system was at equilibrium before the perturbation) is corrected to a certain order

$$\hat{\rho}(t) = \hat{\rho}^{(0)}(t) + \hat{\rho}^{(1)}(t) + \hat{\rho}^{(2)}(t) + ... = \hat{\rho}_{eq} + \sum_{n=1}^{\infty} \hat{\rho}^{(n)}(t) \tag{2.25}$$

It is useful to perform the perturbative expansion within the framework of the interaction picture, which is an alternative representation of the quantum world. In the typical Schrödinger picture used so far, the temporal evolution of the system is contained in the wavefunctions $|\psi(t)\rangle$ while operators $\hat{O}$ are time-independent; instead, in the interaction picture, the evolution under $\hat{H}_S$ is embedded in a new set of wavefunction $|\psi_I(t)\rangle$ and operators $\hat{O}_I(t)$ defined as:

$$|\psi_I(t)\rangle = \hat{U}_S^{\dagger}(t, t_0)\,|\psi(t)\rangle \tag{2.26a}$$

$$\hat{O}_I(t) = \hat{U}_S^{\dagger}(t, t_0)\hat{O}\hat{U}_S(t, t_0) \tag{2.26b}$$

In this representation, the density operator $\hat{\rho}_I(t)$, defined as

$$\hat{\rho}_I(t) = \hat{U}_S^{\dagger}\,(t, t_0)\,\hat{\rho}(t)\hat{U}_S\,(t, t_0) \tag{2.27}$$

obeys to an equivalent of the Liouville-Von Neumann equation in which the system-light Hamiltonian in the interaction picture $\hat{H}_{SL}^I(t)$ takes the place of the total Hamiltonian:

$$\frac{\partial}{\partial t}\hat{\rho}_I(t) = -\frac{i}{\hbar}\left[\hat{H}_{SL}^I(t), \hat{\rho}_I(t)\right] \tag{2.28}$$

The interaction picture thus highlights the evolution caused by the interaction with the electric field. It is possible to solve this equation by integrating over time and plugging iteratively the expression obtained for $\rho_I(t)$ into itself:

$$\hat{\rho}_I(t) = \hat{\rho}\left(t_0\right) + \sum_{n=1}^{\infty}\left(-\frac{i}{\hbar}\right)^n \int_{t_0}^{t} d\tau_n \cdots \int_{t_0}^{\tau_2} d\tau_1 \left[\hat{H}_{SL}^I\left(\tau_n\right), \left[\hat{H}_{SL}^I\left(\tau_{n-1}\right), \ldots, \left[\hat{H}_{SL}^I\left(\tau_1\right), \hat{\rho}\left(t_0\right)\right] \ldots\right]\right] \quad (2.29)$$

Recalling that $\hat{H}_{SL}(t) = -\hat{\mu}E(t)$, one obtains

$$\hat{\rho}_I^{(n)}(t) = \left(\frac{i}{\hbar}\right)^n \int_{t_0}^{t} d\tau_n \cdots \int_{t_0}^{\tau_2} d\tau_1 E\left(\tau_n\right) \ldots E\left(\tau_1\right) \left[\hat{\mu}_I\left(\tau_n\right), \left[\hat{\mu}_I\left(\tau_{n-1}\right), \ldots, \left[\hat{\mu}_I\left(\tau_1\right), \hat{\rho}\left(t_0\right)\right] \ldots\right]\right] \quad (2.30)$$

Reformulating in the Schrödinger's picture, the expression for the n$^{th}$ correction to the density matrix is obtained:

$$\hat{\rho}^{(n)}(t) = \hat{U}_S\left(t, t_0\right) \hat{\rho}_I^{(n)}(t) \hat{U}_S\left(t, t_0\right)^{\dagger} \quad (2.31)$$

This expression can now be conveniently used to calculate the polarization.

### 2.2.3 Response Function Formalism

Substituting Eqn. 2.25 in Eqn. 2.9:

$$P(t) = Tr\left\{\hat{\mu}\hat{\rho}_{eq}\right\} + \sum_{n=1}^{\infty} Tr\left\{\hat{\mu}\hat{\rho}^{(n)}(t)\right\} = \sum_{n=1}^{\infty} Tr\left\{\hat{\mu}\hat{\rho}^{(n)}(t)\right\} \quad (2.32)$$

because the off-diagonal elements of the equilibrium density operator are zero. Comparing this equation with Eqn. 2.3 the following expression for the n$^{th}$-order polarization is obtained:

$$P^{(n)}(t) = Tr\left\{\hat{\mu}\hat{\rho}^{(n)}(t)\right\} = Tr\left\{\hat{\mu}_I(t)\hat{\rho}_I^{(n)}(t)\right\} \quad (2.33)$$

For the last equivalence, Eqns. (2.26) and (2.27) have been used together with the invariance of the trace to cyclic permutation. Using for $\hat{\rho}_I^{(n)}(t)$ the expression specified

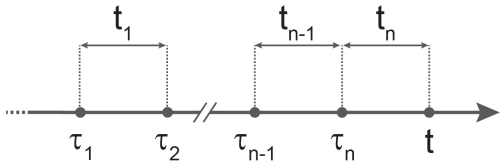


**Figure 2.1:** Relation between two sets of time variables: absolute times at which light-field interactions occur ($\{\tau_j\}$) and time delays between interactions ($\{t_j\}$)

in Eqn. 2.30 and supposing that $\hat{\rho}\left(t_0\right) = \hat{\rho}_{eq}$:

$$P^{(n)}(t) = \left(\frac{i}{\hbar}\right)^n \int_{t_0}^{t} d\tau_n \cdots \int_{t_0}^{\tau_2} d\tau_1 E\left(\tau_n\right) E\left(\tau_{n-1}\right) \ldots E\left(\tau_1\right) \\ Tr\left\{\hat{\mu}_I(t)\left[\hat{\mu}_I\left(\tau_n\right), \left[\hat{\mu}_I\left(\tau_{n-1}\right), \ldots, \left[\hat{\mu}_I\left(\tau_1\right), \hat{\rho}_{eq}\right] \ldots\right]\right]\right\} \quad (2.34)$$

The final step is to perform a change of variables, in order to write the polarization in terms of delays $\{t_j\}$ between the light interactions. Making the substitutions depicted in Fig. 2.1

$$\begin{aligned} \tau_n &= t - t_n \\ \tau_{n-1} &= t - t_n - t_{n-1} \\ &\vdots \\ \tau_1 &= t - t_n - \ldots - t_1 \end{aligned} \quad (2.35)$$

and choosing $\tau_1 = 0$, the following expression for the n$^{th}$-order polarization is obtained:

$$P^{(n)}(t) = \int_0^{\infty} dt_n \cdots \int_0^{\infty} dt_1 E\left(t - t_n\right) E\left(t - t_n - t_{n-1}\right) \ldots \\ E\left(t - t_n - \ldots - t_1\right) S^{(n)}(t_n, t_{n-1}, \ldots, t_1) \quad (2.36)$$

where $S^{(n)}(t_n, t_{n-1}, ..., t_1)$ is the n$^{th}$-order response function:

$$S^{(n)}(t_n, t_{n-1}, ..., t_1) = \left(\frac{i}{\hbar}\right)^n Tr\left\{\hat{\mu}_I\left(t_n + t_{n-1} + ... + t_1\right)\right. \\ \left.\left[\hat{\mu}_I\left(t_{n-1} + ... + t_1\right), \ldots, \left[\hat{\mu}_I(0), \hat{\rho}_{eq}\right] \ldots\right]\right\} \quad (2.37)$$

Since both the polarization $P(t)$ and the electric field $E(t)$ are real physical observables, $S^{(n)}$ is in turn a real observable. The response function carries the complete microscopic information necessary for the calculation of the optical signal: it describes how an equilibrium ensemble changes in response to an applied external agent (in a spectroscopy

problem, the electric field), insofar as the latter causes a small perturbation of the equilibrium condition. The response function does not depend on the absolute arrival times of the interactions, but on the temporal delays between them, as expressed by the change of variable $\{\tau_j\} \rightarrow \{t_j\}$ made above.

Below, the calculation of the third-order response function will be addressed, as it provides the microscopic justification of the optical signal measured in third-order techniques like TA spectroscopy or 2DES. However, before that, it is useful to introduce some concepts and approximations that will be used to calculate $S^{(3)}(t_3, t_2, t_1)$, discussing first the simpler case of the linear response.

### 2.2.4 First Order Response

The first order response function is

$$S^{(1)}(t_1) = \left(\frac{i}{\hbar}\right) Tr\left\{\hat{\mu}_I(t_1)\left[\hat{\mu}_I(0), \hat{\rho}_{eq}\right]\right\} \tag{2.38}$$

The evaluation of the commutator in the expression of $S^{(1)}(t_1)$ reveals the presence of two terms that are the complex conjugate of each other:

$$\begin{aligned} S^{(1)}(t_1) &= \left(\frac{i}{\hbar}\right)\left[Tr\left\{\hat{\mu}_I\left(t_1\right)\hat{\mu}(0)\hat{\rho}_{eq}\right\} - Tr\left\{\hat{\rho}_{eq}\hat{\mu}(0)\hat{\mu}_I\left(t_1\right)\right\}\right] \\ &= \left(\frac{i}{\hbar}\right)\left[J(t_1) - J^*(t_1)\right] \end{aligned} \tag{2.39}$$

Each of the two terms represents a specific sequence of light-matter interactions causing a specific time evolution of the density matrix, known as a Liouville pathway. To understand the physical meaning of a Liouville pathway, it is useful to calculate explicitly the first term. Firstly, $J(t_1)$ can be rewritten in the Schrödinger representation

$$J\left(t_1\right) = Tr\left\{\hat{\mu}_I\left(t_1\right)\hat{\mu}(0)\hat{\rho}_{eq}\right\} = Tr\left\{\hat{\mu}\hat{U}_S\left(t_1, 0\right)\hat{\mu}\hat{\rho}_{eq}\hat{U}_S^{\dagger}\left(t_1, 0\right)\right\} \tag{2.40}$$

The system is initially at thermal equilibrium, described by $\hat{\rho}_{eq}$; for simplicity, only population in the ground state is considered, which means that only the matrix element $\rho_{00}$ is non-null.

$$\hat{\rho}_{eq} = \begin{pmatrix} 1 & 0 \\ 0 & 0 \end{pmatrix} \tag{2.41}$$

At time $t = 0$, an interaction with the field (the dipole moment operator acting on the ket of the density operator) transforms the population $\rho_{00}$ in a coherence $\rho_{10}$, thus generating a nonequilibrium density matrix $\hat{\rho}(0)$

$$\hat{\rho}(0) = \hat{\mu}\hat{\rho}_{eq} = \begin{pmatrix} 0 & \mu_{01} \\ \mu_{10} & 0 \end{pmatrix} \begin{pmatrix} 1 & 0 \\ 0 & 0 \end{pmatrix} = \begin{pmatrix} 0 & 0 \\ \mu_{10} & 0 \end{pmatrix} \tag{2.42}$$

During $t_1$, the ensemble freely propagates under the effect of $\hat{H}_S$, leading to an oscillation of the coherence at frequency $\omega_{10}$:

$$\hat{\rho}(t_1) = \hat{U}_S(t_1, 0)\,\hat{\rho}(0)\hat{U}_S^{\dagger}(t_1, 0) = \begin{pmatrix} 0 & 0 \\ \mu_{10}e^{-i\omega_{10}t_1} & 0 \end{pmatrix} \tag{2.43}$$

The effect of dephasing is neglected for simplicity. Eventually, the perturbed ensemble returns to the equilibrium condition as a population in the ground state $\rho_{00}$. This last step corresponds to the last interaction and the calculation of the trace:

$$\hat{\mu}\hat{\rho}(t_1) = \begin{pmatrix} 0 & \mu_{01} \\ \mu_{10} & 0 \end{pmatrix} \begin{pmatrix} 0 & 0 \\ \mu_{10}e^{-i\omega_{10}t_1} & 0 \end{pmatrix} = \begin{pmatrix} |\mu_{10}|^2 e^{-i\omega_{10}t_1} & 0 \\ 0 & 0 \end{pmatrix}$$

$$J(t_1) = Tr\{\hat{\mu}\hat{\rho}(t_1)\} = |\mu_{10}|^2 e^{-i\omega_{10}t_1} \tag{2.44}$$

$J^*(t_1)$ will not be calculated explicitly, as it is just the complex conjugate of Eqn. 2.44. The Liouville pathway $J^*(t_1)$ differs from $J(t_1)$ because the interaction with the field occurs on the bra of the density matrix and thus the coherence created in $t_1$ is $\rho_{01}$ instead of $\rho_{10}$.

The first order polarization is

$$P^{(1)}(t) = \int_0^{\infty} dt_1 E(t - t_1)\, S^{(1)}(t_1) \tag{2.45}$$

As demonstrated in Eqn. 2.39, $S^{(1)}(t_1)$ is the sum of two terms. Moreover, the electric field arriving at time $\tau_1 = t - t_1$ can be written as a sum of two terms with positive and negative frequencies:

$$E(\tau_1) = \varepsilon(\tau_1) + \varepsilon^*(\tau_1) = \varepsilon_0(\tau_1)\left[e^{i(\vec{k}\cdot\vec{r} - \omega\tau_1)} + e^{-i(\vec{k}\cdot\vec{r} - \omega\tau_1)}\right] \tag{2.46}$$

Therefore, in principle, $P^{(1)}(t)$ would contain $2 \cdot 2 = 4$ terms:

$$\begin{aligned} P^{(1)}(t) = \left(\frac{i}{\hbar}\right) \Bigg[ & \int_0^\infty dt_1 \varepsilon(t-t_1) J(t_1) \\ & + \int_0^\infty dt_1 \varepsilon^*(t-t_1) J(t_1) \\ & - \int_0^\infty dt_1 \varepsilon(t-t_1) J^*(t_1) \\ & - \int_0^\infty dt_1 \varepsilon^*(t-t_1) J^*(t_1) \Bigg] \end{aligned} \tag{2.47}$$

Substituting Eqns. 2.44 and 2.46 in the last expression and neglecting for simplicity the spatial dependence of the field, it is possible to write in a more explicit way the four terms of Eqn. 2.47:

$$\begin{aligned} P^{(1)}(t) = \left(\frac{i}{\hbar}\right) |\mu_{10}^2| \Bigg[ & e^{-i\omega t} \int_0^\infty dt_1 \varepsilon_0(t-t_1) e^{i(\omega-\omega_{10})t_1} \\ & + e^{i\omega t} \int_0^\infty dt_1 \varepsilon_0^*(t-t_1) e^{-i(\omega+\omega_{10})t_1} \\ & - e^{-i\omega t} \int_0^\infty dt_1 \varepsilon_0(t-t_1) e^{i(\omega+\omega_{10})t_1} \\ & - e^{i\omega t} \int_0^\infty dt_1 \varepsilon_0^*(t-t_1) e^{-i(\omega-\omega_{10})t_1} \Bigg] \end{aligned} \tag{2.48}$$

Assuming that the laser field is resonant with the transition ($\omega \approx \omega_{10}$), the second and third integrals, associated with the combinations $\varepsilon^* J$ and $\varepsilon J^*$, contain terms that oscillate rapidly, at frequency $2\omega_{10}$, and can be therefore neglected. This is called Rotating Wave Approximation (RWA). One can think of the meaning of the RWA in this way: in the Liouville pathway $J(t_1)$, it is the $\varepsilon$ component of the field that creates the coherence $\rho_{10}$; instead, when considering $J^*(t_1)$, the coherence $\rho_{01}$ is created by the $\varepsilon^*$ component.

### 2.2.5 Double-Sided Feynman Diagrams

The explicit calculation of a Liouville pathway may require a complicated mathematical notation, especially for orders higher than the first. However, a graphical and more intuitive representation of a sequence of interactions between the sample and the electric fields can be provided by the double-sided Feynman diagrams. The construction of Feynman diagrams relies on a simple set of rules:

(i) the time evolution of the ket and of the bra of the density matrix is represented

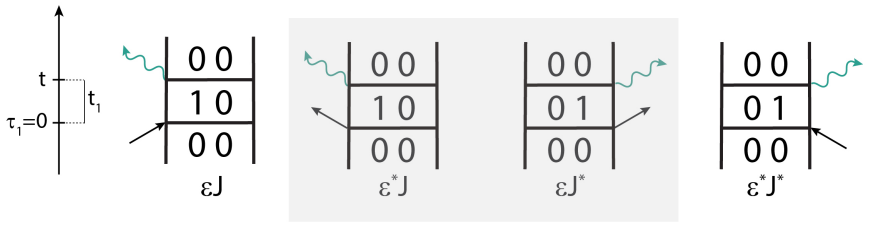


**Figure 2.2:** Feynman diagrams corresponding to the four terms that contribute to linear polarization (Eqn. 2.47). The shaded area indicates the contributions that are excluded by the rotating wave approximation.

by a left and a right vertical line respectively, with the time running from the bottom to the top;

(ii) interactions with the electric fields are represented by arrows: an arrow pointing to the right (left) depicts an interaction with the $\varepsilon$ ($\varepsilon^*$) component of the electric field;

(iii) the last arrow represents the emission of the signal from the sample and is therefore indicated with a different kind of arrow (a wavy arrow in the diagrams shown in this thesis);

(iv) an arrow pointing towards (away from) the density matrix represents an absorption (emission) interaction;

(v) the density matrix is initially in an equilibrium state, usually the ground state, and after the emission of the signal it reaches again a population state, ground or excited.

The diagrams representing the four contributions to the linear polarization are shown in Fig. 2.2. In these diagrams, the physical intuition behind the RWA is made even clearer. The first two diagrams from the left represent the Liouville pathway $J(t_1)$, in which the interaction occurs on the ket of the density matrix, transforming the ground state population $\rho_{00}$ into the coherence $\rho_{10}$. In the first diagram, this is obtained with a field $\varepsilon$ that causes an excitation of the ket, while in the second one the same process would be obtained with a field $\varepsilon^*$ that causes a de-excitation of the ket. This second diagram is physically unreasonable and is excluded by the RWA. As for each Liouville pathway the complex conjugate exists, for each diagram there is a mirrored diagram with all the right and left choices reversed. The diagrams for $J^*(t_1)$ are the last two in Fig. 2.2. By convention, only the diagrams with the emission of the signal from the left

are shown.

### 2.2.6 Third Order Response Function

The most common third-order techniques are related to four-wave mixing (4WM), in which the interaction of three laser pulses with the material system generates third-order polarization that acts as a source of a fourth signal field. The third-order polarization is given by

$$P^{(3)}(t) = \int_0^\infty dt_3 \int_0^\infty dt_2 \int_0^\infty dt_1 \\ E\left(t-t_3\right) E\left(t-t_3-t_2\right)\left(t-t_3-t_2-t_1\right) S^{(3)}\left(t_3,t_2,t_1\right) \quad (2.49)$$

where the third-order response function is

$$S^{(3)}\left(t_3,t_2,t_1\right) = \left(\frac{i}{\hbar}\right)^3 Tr\left\{\hat{\mu}_I\left(t_3+t_2+t_1\right)\left[\hat{\mu}_I\left(t_2+t_1\right),\left[\hat{\mu}_I\left(t_1\right),\left[\hat{\mu}_I(0),\hat{\rho}_{eq}\right]\right]\right]\right\} \quad (2.50)$$

Writing the commutators explicitly for the third-order response function generates $2^3 = 8$ terms, complex conjugate in pairs:

$$S^{(3)}\left(t_3,t_2,t_1\right) = \left(\frac{i}{\hbar}\right)^3 \sum_{\alpha=1}^{4}\left[R_\alpha\left(t_3,t_2,t_1\right) - R_\alpha^*\left(t_3,t_2,t_1\right)\right] \quad (2.51)$$

with

$$R_1\left(t_3,t_2,t_1\right) = Tr\left\{\hat{\mu}_I\left(t_1+t_2+t_3\right)\hat{\mu}(0)\hat{\rho}_{eq}\hat{\mu}_I\left(t_1\right)\hat{\mu}_I\left(t_1+t_2\right)\right\} \quad (2.52a)$$

$$R_1^*\left(t_3,t_2,t_1\right) = Tr\left\{\hat{\mu}_I\left(t_1+t_2+t_3\right)\hat{\mu}_I\left(t_1+t_2\right)\hat{\mu}_I\left(t_1\right)\hat{\rho}_{eq}\hat{\mu}(0)\right\} \quad (2.52b)$$

$$R_2\left(t_3,t_2,t_1\right) = Tr\left\{\hat{\mu}_I\left(t_1+t_2+t_3\right)\hat{\mu}_I\left(t_1\right)\hat{\rho}_{eq}\hat{\mu}(0)\hat{\mu}_I\left(t_1+t_2\right)\right\} \quad (2.52c)$$

$$R_2^*\left(t_3,t_2,t_1\right) = Tr\left\{\hat{\mu}_I\left(t_1+t_2+t_3\right)\hat{\mu}_I\left(t_1+t_2\right)\hat{\mu}(0)\hat{\rho}_{eq}\hat{\mu}_I\left(t_1\right)\right\} \quad (2.52d)$$

$$R_3\left(t_3,t_2,t_1\right) = Tr\left\{\hat{\mu}_I\left(t_1+t_2+t_3\right)\hat{\mu}_I\left(t_1+t_2\right)\hat{\rho}_{eq}\hat{\mu}(0)\hat{\mu}_I\left(t_1\right)\right\} \quad (2.52e)$$

$$R_3^*\left(t_3,t_2,t_1\right) = Tr\left\{\hat{\mu}_I\left(t_1+t_2+t_3\right)\hat{\mu}_I\left(t_1\right)\hat{\mu}(0)\hat{\rho}_{eq}\hat{\mu}_I\left(t_1+t_2\right)\right\} \quad (2.52f)$$

$$R_4\left(t_3,t_2,t_1\right) = Tr\left\{\hat{\mu}_I\left(t_1+t_2+t_3\right)\hat{\mu}_I\left(t_1+t_2\right)\hat{\mu}_I\left(t_1\right)\hat{\mu}(0)\hat{\rho}_{eq}\right\} \quad (2.52g)$$

$$R_4^*\left(t_3,t_2,t_1\right) = Tr\left\{\hat{\mu}_I\left(t_1+t_2+t_3\right)\hat{\rho}_{eq}\hat{\mu}(0)\hat{\mu}_I\left(t_1\right)\hat{\mu}_I\left(t_1+t_2\right)\right\} \quad (2.52h)$$

These terms result from the fact that each interaction can occur either on the ket or on the bra of the density operator; for example, in $R_1$ the first interaction acts on

| | 0 | $t_1$ | $t_1 + t_2$ | | 0 | $t_1$ | $t_1 + t_2$ |
|---|---|---|---|---|---|---|---|
| $R_1$ | ket | bra | bra | $R_1^*$ | bra | ket | ket |
| $R_2$ | bra | ket | bra | $R_2^*$ | ket | bra | ket |
| $R_3$ | bra | bra | ket | $R_3^*$ | ket | ket | bra |
| $R_4$ | ket | ket | ket | $R_4^*$ | bra | bra | bra |

**Table 2.1:** Sequences of interactions on the density matrix in the case of third-order processes.

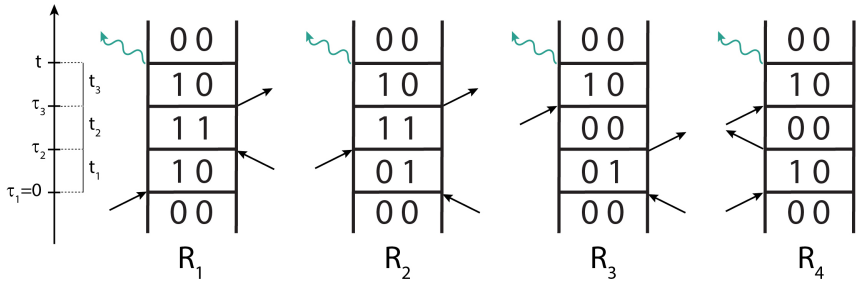


**Figure 2.3:** Feynman diagrams representing different paths contributing to the third order response of a two-level system. Only the diagrams with the emission of the signal from the left are shown.

the ket of the density operator, whereas the second and the third on the bra. There are 8 possible sequences of left/right interactions, as summarized in Tab. 2.1. The number of Liouville pathways (and corresponding Feynman diagrams) that can be excited by the pulse sequence depends on the number of accessible energy levels and the spectral bandwidth of the pulses. In the case of a two-level system, only four possible diagrams (and their complex conjugates) can be written, as shown in Fig. 2.3. In the diagrams corresponding to $R_1$ and $R_2$, the first two pulses generate an excited state population and the third one creates the coherence with the ground state, which is responsible for the emission of the signal. These two diagrams correspond to Stimulated Emission (SE) pathways. The expression for $R_1$ and $R_2$ can be calculated starting from Eqns. 2.52 or by inspection of the corresponding diagrams:

$$R_1\left(t_3, t_2, t_1\right) \propto |\mu_{10}|^4 e^{-i\omega_{10}t_1} e^{-i\omega_{10}t_3} \tag{2.53}$$

$$R_2\left(t_3, t_2, t_1\right) \propto |\mu_{10}|^4 e^{i\omega_{10}t_1} e^{-i\omega_{10}t_3} \tag{2.54}$$

$R_2$ is a rephasing term, as it evolves in conjugate coherences during $t_1$ and $t_3$, so the phase acquired in $t_1$ is reversed in $t_3$; instead, $R_1$ is a non-rephasing term, as it evolves in the same coherence state during $t_1$ and $t_3$ and the phase is acquired continuously during both intervals. In the diagrams corresponding to $R_3$ and $R_4$, the first two pulses cause a depletion of the ground state population and then the third creates a coherence

with the excited state and therefore the optical signal. These two diagrams correspond to Ground State Bleaching (GSB) pathways. For the same reasons outlined above, $R_3$ is a rephasing pathway, while $R_4$ is a non-rephasing pathway.

Each Liouville pathway generates a different contribution to the overall response function; in the expression of the polarization, each of these contributions is multiplied by the term

$$E(t-t_3)E(t-t_3-t_2)E(t-t_3-t_2-t_1)$$

If the incoming field consists of three laser pulses ($E_1$, $E_2$ and $E_3$), each field $E(\tau_k)$ in Eqn. 2.49 is the sum of six terms:

$$E(\tau_k) = \sum_{j=1}^{3} E_j(\tau_k) = \sum_{j=1}^{3} [\varepsilon_j(\tau_k) + \varepsilon_j^*(\tau_k)] \tag{2.55}$$

Therefore, each Liouville pathway would contribute with 6·6·6 terms to the polarization. However, the number of terms can be lowered considerably by considering a series of experimental boundaries.

First of all, in time-resolved spectroscopy, it is common to operate within the semi-impulsive limit: the laser pulses are assumed to be short compared with the separation between them and any time scale of the system, but long compared with the oscillation period of the light field. This means that they do not overlap in time and that there is strict time ordering: the first interaction at time $\tau_1$ originates exclusively from pulse $E_1$, the second at time $\tau_2$ from pulse $E_2$ and the third at time $\tau_3$ from pulse $E_3$ ($E(\tau_k) = E_k(\tau_k)$).

Each of the 8 Liouville pathways would still be split into $2 \cdot 2 \cdot 2$ terms, each carrying a wavevector $\vec{k}_S$ and a frequency $\omega_S$ given by a specific combination of the wavevectors and frequencies of the incoming fields:

$$\vec{k}_s = \pm\vec{k}_1 \pm \vec{k}_2 \pm \vec{k}_3 \tag{2.56a}$$

$$\omega_s = \pm\omega_1 \pm \omega_2 \pm \omega_3 \tag{2.56b}$$

The positive/negative sign comes from the fact that, in principle, each arrow in the diagrams can point to the right (component $\varepsilon$ with wavevector $+k_j$ and frequency $+\omega_j$) or to the left (component $\varepsilon^*$ with wavevector $-k_j$ and frequency $-\omega_j$). However,

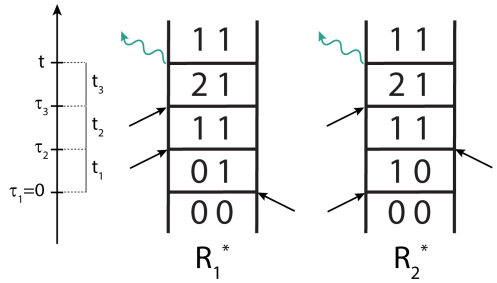


**Figure 2.4:** Feynamn diagrams representing ESA pathways

not all the combinations in Eqn. 2.56 are compatible with the RWA, as discussed in the previous section. For example, in $R_1$, the first two interactions should represent excitation of the ket ($\varepsilon$) and the bra ($\varepsilon^*$), while the last one should represent a de-excitation of the bra ($\varepsilon$). For each Liouville pathway, only one set of signs survives the RWA, namely $+\vec{k}_1 - \vec{k}_2 + \vec{k}_3$ for the non-rephasing terms $R_1$ and $R_4$ and $-\vec{k}_1 + \vec{k}_2 + \vec{k}_3$ for the rephasing terms $R_2$ and $R_3$. This also means that rephasing and non-rephasing signals are emitted in different directions (phase matching) and can therefore be measured separately from each other by properly tuning the geometry of the setup.

Real systems are generally more complicated than the simple two-level systems considered so far and other contributions to the overall signal should be taken into account. For example, if a higher excited state $|2\rangle$ is accessible, the first two pulses could drive the system in a first excited state and the third could probe a second excited state. Pathways of this kind, represented by the diagrams in Fig. 2.4, are called Excited State Absorptions (ESA):

$$R_1^*(t_3, t_2, t_1) \propto |\mu_{10}|^2 |\mu_{21}|^2 e^{i\omega_{10}t_1} e^{-i\omega_{21}t_3} \tag{2.57}$$

$$R_2^*(t_3, t_2, t_1) \propto |\mu_{10}|^2 |\mu_{21}|^2 e^{-i\omega_{10}t_1} e^{-i\omega_{21}t_3} \tag{2.58}$$

The rephasing term $R_1^*$ will contribute to the signal emitted in the $-\vec{k}_1 + \vec{k}_2 + \vec{k}_3$ direction, whereas the non-rephasing term $R_2^*$ term will contribute to the signal emitted in the $\vec{k}_1 - \vec{k}_2 + \vec{k}_3$ direction.

In all the examples discussed so far, the first two interactions excited the same transition, creating a population in an excited state (or a bleached ground state). When relaxations are included, Liouville pathways of this type evolve during the time interval $t_2$ following an exponential trend, with a time constant reflecting the lifetime of the

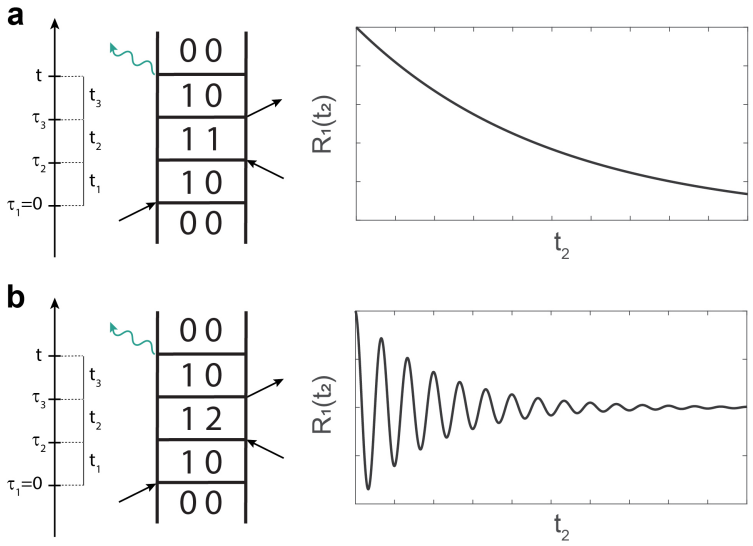


**Figure 2.5:** Examples of (a) non-oscillating and (b) oscillating contributions to the third order signal, graphically represented by double-sided Feynman diagrams.

excited state (Fig. 2.5a). If instead two different states were excited by the first two pulses, a coherence would be created, with the characteristic oscillatory pattern in $t_2$. For example, the calculation of the coherent $R_1$ pathway shown in Fig. 2.5b would return:

$$R_1\left(t_3, t_2, t_1\right) \propto |\mu_{10}|^2 |\mu_{20}|^2 e^{-i\omega_{10}t_1} e^{(-1/T^{(21)} - i\omega_{21})t_2} e^{-i\omega_{10}t_3} \tag{2.59}$$

Here phenomenological relaxation ($T^{(21)}$) was added to highlight dynamics during $t_2$.

It is clear that, as the complexity of the system increases, the number of processes that can contribute to third-order polarization increases accordingly. The various third-order spectroscopic techniques, some of which are outlined in the following chapter, are therefore extremely rich in information and prove to be a powerful tool in the hands of the spectroscopic investigator who knows how to handle the complexity of the data they provide.

# Chapter 3

# Experimental Techniques

This chapter focuses on spectroscopic techniques that exploit the linear and third-order phenomena that were theoretically described in the previous chapter. While linear absorption is a widespread technique that can be performed using commercial instrumentation, TA and 2DES are less popular and will be more extensively discussed. The experimental setups used to implement these two techniques in our laboratory will also be presented.

## 3.1 Steady-State Absorption

UV-Vis absorption spectroscopy is a linear optical technique that measures the intensity of the light absorbed by the sample at different wavelengths. In a UV-Vis spectrometer, a specific wavelength of the light source is selected by a monochromator and sent to the sample; then the intensity of the transmitted light $I(\lambda)$ is measured and compared to the intensity of the incident light $I_0(\lambda)$ to calculate the absorbance $A(\lambda)$ at that specific wavelength:

$$A(\lambda) = -\log\left(\frac{I(\lambda)}{I_0(\lambda)}\right) = \epsilon(\lambda)Cl \tag{3.1}$$

where $\epsilon(\lambda)$ is the molecular extinction coefficient, $C$ is the sample concentration and $l$ is the sample thickness. By scanning over a desired range of wavelengths, the absorption spectrum is obtained. In our laboratory, absorption measurements are performed with a Varian Cary 5 spectrometer. Absorption spectroscopy was used to identify the main electronic transitions in the samples, adjust the concentration to obtain optimal ab-

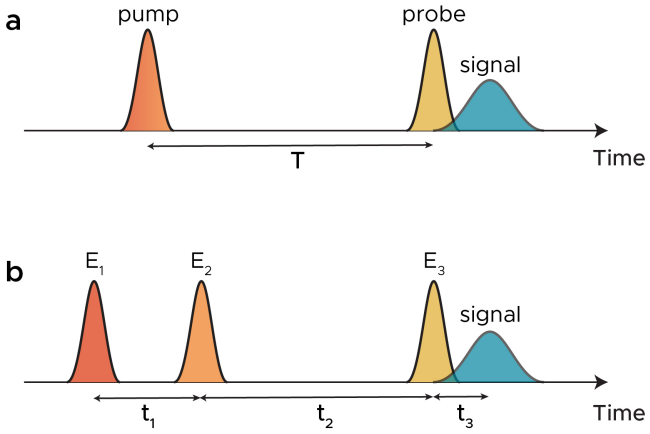


**Figure 3.1:** (a) Pulse sequence for a transient absorption experiment; $T$ is the time delay between the pump and the probe. (b) Pulse sequence for a two-dimensional electronic spectroscopy experiment; $t_1$, $t_2$ and $t_3$ are the time intervals between the first and the second pulse, the second and the third pulse and the third pulse and the emission of the signal, respectively.

sorbance for TA and 2DES measurements and check whether the sample has degraded after irradiation with laser pulses.

## 3.2 Transient Absorption Spectroscopy

Among the third-order methods, TA spectroscopy [28, 29], also called pump-probe spectroscopy, is one of the most popular techniques to study the dynamics of excited electronic states. A TA experiment is based on the pulse sequence depicted in Fig. 3.1a: an ultrafast light pulse (the "pump") prepares an excited state and, after a time delay $T$, a spectrally-broadened, white light pulse (the "probe") is sent to the sample to measure the absorption spectrum of the excited state. The transient spectrum is given by the differential absorption $\Delta A(\lambda, T)$, namely the difference between the absorbance at time $T$ after pump excitation and the absorbance in absence of the pump pulse:

$$\Delta A(\lambda, T) = A(\lambda, T) - A(\lambda, -\infty) = -\log\left(\frac{I(\lambda, T)}{I(\lambda, -\infty)}\right) \tag{3.2}$$

where $I(\lambda, T)$ and $I(\lambda, -\infty)$ are the intensity of the transmitted probe in the presence and absence of pump excitation, respectively. As introduced in the previous chapter, typical signals that are observed in excited-state spectra are:

- GSB: it is the reduction in the absorbance of a specific electronic transition as a consequence of the depletion of the ground state caused by the pump. It is

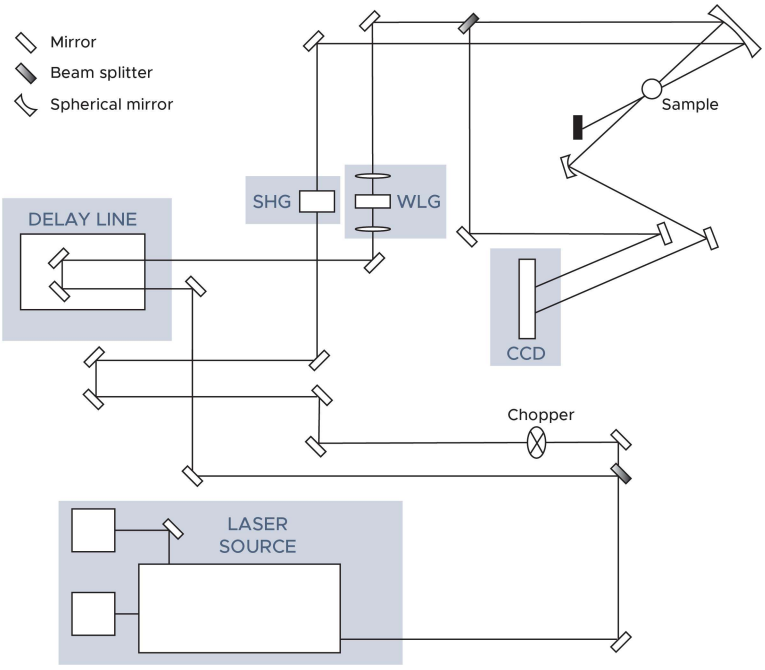


**Figure 3.2:** Schematic representation of the experimental setup used for transient absorption measurements. SHG = Second Harmonic Generation; WLG = White Light Generation; CCD = Charge-Coupled Device camera.

characterized by a negative $\Delta A$.

- SE: the probe triggers the emission from an excited state prepared by the pump. The light emitted adds to the transmitted probe, resulting in a higher intensity for the transmitted beam and therefore in a reduction of the absorbance (negative $\Delta A$).

- ESA: the pump prepares an excited state and the probe excites a transition from that state to a higher excited state. This causes a growth in the absorbance (a positive $\Delta A$) at the wavelengths corresponding to the energetic separation between the two excited states.

If the experiment is repeated for different values of the time delay $T$, it is possible to characterize the time evolution of the TA spectra.

The formalism already introduced for third-order phenomena can be applied to this technique by considering that the pump accounts for the first two interactions ($t_1 = 0$), the time delay $T$ corresponds to the time interval $t_2$ and the frequency axis is the Fourier-transform of the time interval $t_3$.

The experimental setup used for pump-probe measurements is already described in

several works [30, 31, 32] and will be briefly outlined here. The source is an amplified Ti:Sapphire laser system (Mai-Tai and Spitfire, Spectra Physics) that emits pulses at 800 nm, with energy of 0.6 mJ per pulse, repetition rate of 1 kHz, and 150 fs pulse duration. The output laser beam is split by a 4% beam splitter into two paths. The weaker one is sent to a thin sapphire plate to generate a white-light continuum probe. The second portion is used to obtain the pump pulse at 400 nm via Second Harmonic Generation (SHG) in a BBO thin crystal. The polarizations of the pump and probe pulses are made parallel by using two polarizers and the pump fluence is tuned between 100 and 1000 $\mu J/cm^2$, depending on the photostability of the sample, by using OD filters. The repetition rate of the pump is halved to 500 Hz through an optical chopper to collect, alternatively, pumped and unpumped signals. Before the sample, the probe is split into two beams, one directed to the sample and the other sent directly to the detector and used as a reference. A spherical mirror focuses pump and probe pulses on the sample, where their diameters are measured to be in the range of tens of $\mu m$; the beam waist of the pump is kept at least two times larger than that of the probe beam in order to ensure good spatial overlap. The transmitted probe is spectrally resolved and directed to a Charge-Coupled Device (CCD) camera for detection. Experiments are repeated by scanning the time delay $T$ between pump and probe pulses with a motorized linear stage. The signal-to-noise ratio is improved by repeating and averaging between multiple measurements. The obtained spectra are processed to minimize white light chirping effects by using a home-made Matlab routine, which applies a polynomial correction to determine the $t_0$ of the different wavelength components.

Pump and probe spectroscopy suffers from a limited signal-to-noise ratio, because the signal is not background-free. Indeed, the phase-matching condition for the pump-probe experiment is $\vec{k}_{sig} = \pm\vec{k}_{pump} \mp \vec{k}_{pump} + \vec{k}_{probe} = \vec{k}_{probe}$. Therefore, the signal is detected in the same propagation direction as that of the probe pulse. Another potential limitation of the TA technique is the interdependence between time and excitation frequency resolution, due to the time-frequency indetermination principle: the narrow-band pulses needed for a selective excitation have long envelopes in the time domain, making this technique suitable for the study of phenomena occurring in sufficiently long time scales (from hundreds of femtoseconds to hundreds of picoseconds). Conversely, if a higher temporal resolution was needed, selectivity in excitation would be partially sacrificed. Both these drawbacks are bypassed in 2DES.

## 3.3 Two-Dimensional Electronic Spectroscopy

A TA signal shows the transient spectrum of a sample after excitation at a specific wavelength. Especially when multichromophoric systems need to be studied, however, a complete information about the excited-state dynamics can be reconstructed by looking at the TA response obtained at different excitation frequencies. One could think to add a second excitation frequency dimension to a TA response by simply scanning the frequency of a narrow-band exciting pulse; however, this would compromise the time resolution. 2DES overcomes the problem by decoupling excitation frequency and time resolution by following a different approach, based on a Fourier transform methodology [10, 11, 12, 33, 34].

Fig. 3.1b schematizes the pulse sequence used for 2DES following the same notation introduced in Chapter 2 for a generic 4WM technique. A new time interval is introduced by splitting the pump in two pulses delayed by a time $t_1$; the probe arrives a time $t_2$ (corresponding to the time interval $T$ of the TA technique) after the second pump pulse and triggers the emission of the signal. The signal is acquired during the time interval $t_3$, which is Fourier-transformed by a spectrograph during detection, so that a spectrum as a function of $\omega_3$ is registered. The pulses used for 2DES are ultrashort ($\sim$10 fs) and have a broad spectrum. Thus the first pump pulse excites all the coherences between the ground state and the electronic states that fall within its spectral band. By scanning the delay between the first two pulses it is possible to reconstruct the evolution during the time interval $t_1$: this turns out to be the sum of a series of coherences oscillating at different frequencies. The Fourier transform along $t_1$ spectrally resolves these contributions and spreads the pathways arising from excitation of different states in a new $\omega_1$ axis. The result is a 2D spectrum $(\omega_1, \omega_3)$ that shows the transient responses arising from excitation in different energy levels of the sample. Moreover, by scanning the time delay $t_2$, it is possible to study the excited state dynamics with a time resolution that can be as short as tens of femtoseconds. This allows to characterize processes that couple electronic states, like energy transfer or relaxations, with unprecedented level of detail.

However, all these advantages do not come without the price of a complex optical setup. A series of fine experimental expedients must be employed to tackle the main challenges of this technique: guaranteeing accurate time delays between the pulses, iso-

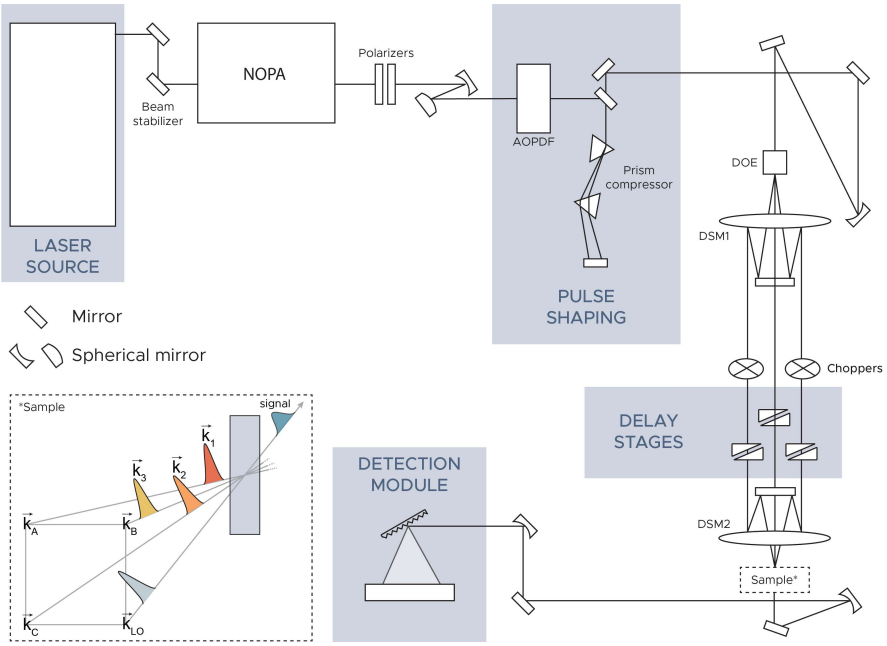


**Figure 3.3:** Schematic representation of the experimental setup used for two-dimensional electronic spectroscopy. NOPA = Non-collinear Optical Parametric Amplifier; AOPDF = Acousto-Optic Programmable Dispersive Filter; DOE = Diffractive Optical Element; DSM = Donut-shaped Spherical Mirror. The inset shows a zoom on the sample and represents the propagation of the pulses ($\vec{k}_1$, $\vec{k}_2$ and $\vec{k}_3$) along the directions corresponding to the vertices of an ideal square ($\vec{k}_A$, $\vec{k}_B$ and $\vec{k}_C$), according to the BOXCARS geometry. The case represented is that of rephasing experiments ($\vec{k}_A = \vec{k}_1$, $\vec{k}_C = \vec{k}_2$ and $\vec{k}_B = \vec{k}_3$). The Local Oscillator (LO) propagates along the fourth vertex of the square.

lating and detecting the weak third-order signal and keep the phase difference between the pulses constant. In the following sections, the fully non collinear 2DES setup used in our laboratory, as well as the main aspects of calibration, data acquisition and processing procedures will be summarized. A more detailed description can be found in the work of Bolzonello *et al.* [35]

### 3.3.1 2DES Setup

The experimental setup is schematically illustrated in Fig. 3.3.

**Light source and conversion.** The pulse sequence for the 2DES measurements is generated starting from an amplified pulsed laser source (Libra Coherent, Santa Clara, CA, US), whose output is a train of 100 fs pulses centered at 800 nm, with a repetition rate of 3 kHz. Through a couple of piezoelectric mirrors (Newport Guide Star II, Irvine, CA, US), the beam is stabilized and delivered to a non-collinear optical parametric amplifier (TOPAS White Light Conversion, Vilnius, Lithuania), which tunes

the central wavelength of the pulse in the Vis range; each pulse has an energy of ∼10 μJ, but the output power can be regulated through a broadband half-waveplate/polarizer system coupled with a beam splitter that reflects and discards part of the light.

**Compression and shaping.** Whenever a broadband pulse passes through a transmissive optic, its different frequency components are retarded differently, causing phase distortions. At the end of the setup, the pulse would be affected by a chirp that would compromise the time resolution desired for the 2DES experiment. A stage of compression and shaping is thus needed to approach as closely as possible the Transform Limited (TL) pulse, namely the shortest pulse for a given bandwidth. This is accomplished through the synergistic work of a prism compressor and an Acousto-Optic Programmable Dispersive Filter (AOPDF, Dazzler Fastlite, Antibes, France). The acousto-optic interaction occurring within the AOPDF [36, 37] allows for complete control over the phase of the pulses via software and correction of the chirp. However, the AOPDF suffers from a self-induced chirp that is compensated by the prism compressor [38].

**BOXCARS.** A diffractive optic element splits the pulse into four identical replicas, three of which (hereafter indicated with their wavevectors $\vec{k}_1$, $\vec{k}_2$, and $\vec{k}_3$) are used for the 2DES pulse sequence, while the remaining one is attenuated with a neutral density filter and used as a local oscillator (LO) for heterodyne detection. With the use of a donut-shaped spherical mirror (DSM), the four replicas are parallelized and arranged in a BOXCARS geometry, with pulses $\vec{k}_1$, $\vec{k}_2$, and $\vec{k}_3$ along three vertices of an ideal square (directions $\vec{k}_A$, $\vec{k}_B$, and $\vec{k}_C$) and the LO along the fourth vertex (see inset in Fig. 3.3). Pulses $\vec{k}_1$, $\vec{k}_2$, and $\vec{k}_3$ are directed onto couples of antiparallel $CaF_2$ wedges; in each wedge pair, one wedge is kept fixed while the other one is moved with a translation stage (Ant95 Aerotech, Pittsburgh, PA, US). The motion of the stages via software regulates the thickness of the medium crossed by each pulse and thus imposes a time delay $t_1$ between $\vec{k}_1$ and $\vec{k}_2$ and a time delay $t_2$ between $\vec{k}_2$ and $\vec{k}_3$. A calibration of the stages, aimed at finding the relation between position of the stage ad time delay provided by the wedge pair, ensures sub-femtosecond precision of the time delays for the entire time windows, as large as 2 ps. This, together with the choice of $CaF_2$, which induces less phase distortions in the pulse with respect to common fused silica, helps maintaining phase stability during the scan. Finally, with a second DSM, the pulse sequence is focused on the sample.

**Detection.** The third-order signal is emitted in the phase-matched direction $\vec{k}_s =$

$-\vec{k}_A+\vec{k}_B+\vec{k}_C$, which coincides with the fourth vertex of the BOXCARS square, where the LO propagates. In this "heterodyne detection" scheme, the actual signal arriving in the detection module is an interference between the signal and LO:

$$I_{HET} = |E_s + E_{LO}|^2 + |E_s|^2 + |E_{LO}|^2 + 2Re\left\{E_s^*(t)E_{LO}(t)\right\} \tag{3.3}$$

The "homodyne" third order signal emitted by the sample is typically extremely low and even more so is its intensity, as it depends on the second power of the field ($I_{HOMO} \propto |E_s(t)|^2$). After subtraction of the LO intensity and removal of the homodyne signal, which is done during the post-processing steps, the interference between the signal and LO results linear with the electric field. The heterodyne detection thus ensures higher sensitivity and signal-to-noise ratio. Eventually, the signal is separated into its frequency components by a spectrograph (Shamrock 303i Andor) and recorded via a scientific Complementary Metal–Oxide Semiconductor (sCMOS) camera (Zyla Andor, Oxford Instruments, Belfast, Northern Ireland).

**Measurement of Pulse Duration.** Before the experiment, it is important to check that the pulse duration is as near as possible to the TL condition. The measurement of the pulse duration is made through Frequency Resolved Optical Gating (FROG) [39]. This technique detects the third-order response of a non-resonant sample, usually a solvent like DMSO, and uses the same setup geometry as 2DES. The time delays between two pulses ($\vec{k}_1$ and $\vec{k}_2$) is set to zero, while the third one ($\vec{k}_3$) is delayed by a time $T$, which is scanned between -25 and 25 fs. At the sample position, the interference between the first two pulses acts as an optical grating that produces a signal when the third pulse arrives; the signal decays when the pulse is moved away from the superposition condition. The intensity of the FROG signal is plotted against the time axis $T$ and fitted with a gaussian function, whose full width at half maximum (FWHM) is related to the time duration of the pulse. In order to fulfill the TL condition, the prism compressor alignment and the AOPDF correction must be optimized through an iterative procedure guided by repeated FROG experiments.

**Data Acquisition.** The signal detected in a single scan is a $S_{t_1,t_2}(\omega_3)$ spectrum, where $\omega_3$ is the frequency dimension read directly by the sCMOS camera, corresponding to the Fourier transform of the third time interval $t_3$. To acquire the full data matrix $S(t_1, t_2, \omega_3)$, the experiment is conducted by scanning the time delays $t_1$ and $t_2$. By controlling the relative arrival time of the pulses, two types of experiments are

performed: in the rephasing (R) experiments, the pulse propagating along the direction $\vec{k}_A$ arrives first ($\vec{k}_A = \vec{k}_1$, $\vec{k}_C = \vec{k}_2$ and $\vec{k}_B = \vec{k}_3$, thus $\vec{k}_S = -\vec{k}_1 + \vec{k}_2 + \vec{k}_3$); in the non-rephasing (NR) experiments, the pulse propagating along the direction $\vec{k}_C$ arrives first ($\vec{k}_C = \vec{k}_1$, $\vec{k}_A = \vec{k}_2$ and $\vec{k}_B = \vec{k}_3$, thus $\vec{k}_S = +\vec{k}_1 - \vec{k}_2 + \vec{k}_3$). The experiment on each sample was repeated to ensure reproducibility and averaged to reduce noise. The acquisition routine is based on the double lock-in modulation method proposed by Augulis et al. [40]: the exciting pulses $\vec{k}_2$ and $\vec{k}_3$ are modulated by two optical choppers at frequencies $\nu_{E_2}$ and $\nu_{E_3}$, and the signal is therefore modulated at both sum and difference frequencies, $\nu_s^+ = \nu_2 + \nu_3$ and $\nu_s^- = \nu_2 - \nu_3$. After a Fourier Transform operation, the signal modulated at frequency $\nu_s^+$ or $\nu_s^-$ can be isolated from the majority of other contributions, which reach the detector with no modulation or with the modulation frequency of a single chopper.

The raw data acquired by the camera is prepared for analysis with a series of processing steps that includes:

- Application of a Rotating Frame (RF) approach in $t_1$. By taking the central frequency of the laser bandwidth $\omega_{lsr}$ as a reference, the signal results slowly modulated in $t_1$, with the maximum modulation frequency corresponding to half of the laser bandwidth (a few thousands of $\mathrm{cm}^{-1}$). The RF, introduced *a posteriori* during processing, allows to reduce the sampling frequency in $t_1$ and therefore to shorten greatly the time needed for data collection. Although this does not improve the quality of a single dataset, it gives the opportunity to increase the signal-to-noise ratio by averaging multiple measurements.
- Filtering out remaining spurious contributions. With this aim, an inverse Fourier transform is performed along the $\omega_3$ axis and a time filter along the resulting $t_3$ dimension is applied. The filter consists of a super-Gaussian function, whose parameters are chosen in such a way that spurious contributions can be excluded without introducing artifacts deriving from the truncation of a not completely decayed signal [35].
- Fourier transform along $t_1$; the resulting frequency axis $\omega_1$ is shifted by $\omega_{lsr}$ to account for the RF.

The resulting rephasing $S_R(\omega_1, t_2, \omega_3)$ and non-rephasing $S_{NR}(\omega_1, t_2, \omega_3)$ data are two-dimensional, complex-valued spectra that contain absorptive and dispersive contribu-

tions both in the real and in the imaginary parts. A purely absorptive spectrum can be obtained by summing R and NR data, thus obtaining the total (T) signal $S_T(\omega_1, t_2, \omega_3)$, and taking the real part of it. By integrating the purely absorptive signal along $\omega_1$, one obtains a mono-dimensional projection of the 2DES data onto $\omega_3$, which, in principle, should match the TA spectrum (projection-slice theorem [41]). However, the complex-value 2DES data bear an arbitrary phase that may cause a mismatch between the projection and the TA signal. Therefore, a proper phase correction is applied to R and NR data to fulfill the projection-slice theorem and extract meaningful information from the 2D spectrum.

### 3.3.2 Analysis of 2DES Maps

Several methods, largely examined in literature [42, 43, 44, 45], have been proposed to analyze the 2DES signals. As extensively discussed in the following chapters, the most suitable strategy of analysis depends on the nature of the data and on the kind of information one wants to extract. Here, only a general overview of the structure of 2DES data and of the information they offer is presented.

An intuitive way to visualize 2DES data is to plot the purely absorptive signal as a stack of two-dimensional frequency-frequency maps $S_{t_2}(\omega_1, \omega_3)$ referred to succeeding $t_2$ times. The frequency axis $\omega_1$, called "excitation frequency" defines the electronic transition excited by the first pulse of the sequence. The $\omega_3$ axis, called "detection (or emission) frequency", provides the information on the excited states probed by the third pulse. The intervals covered by the two frequency axes depend on the central frequency and the width of the pulse spectrum. Since in our setup the pulses in the exciting sequence are replicas of the same pulse, the two frequency dimensions span the same spectral interval. By properly choosing the pulse bandwidth it is possible to focus the attention on a specific subset of electronic states of the system and retrieve only the spectroscopic signatures of photo-triggered processes of interest. On the other hand, by increasing the bandwidth of the pulse it is possible to gather greater amount of information at the same time, at the price of a more challenging analysis.

The various pathways that can be excited by the pulse sequence contribute to the 2D spectrum at different coordinate combinations $(\omega_1, \omega_3)$ and with different time evolutions. To better understand how to interpret a peak in a 2DES spectrum, it is

useful to consider the contribution of a generic pathway to the third order response function. As exemplified in Eqns. 2.53 - 2.54 and 2.57 - 2.59, this can be written as:

$$S(t_1, t_2, t_3)_{R,NR} \propto e^{\pm i\omega_{ij}t_1} e^{-(1/T_{kl}+i\omega_{kl})t_2} e^{-i\omega_{mn}t_3} \tag{3.4}$$

where the positive sign is for the rephasing pathway and the negative sign for the non-rephasing counterpart. Eqn. 3.4 describes the following generic sequence of events:

1. The first pulse creates a coherence $\rho_{ij}$, which oscillates at frequency $\omega_{ij}$ during the time interval $t_1$.

2. After the second pulse, the system reaches a state $\rho_{kj}$ or $\rho_{ik}$, depending on whether the interaction occurs on the ket or on the bra of the density matrix. To remain general, we will consider that, after the second pulse, the system is in state $\rho_{kl}$. This could be either a coherence ($k \neq l$) with oscillation frequency $\omega_{kl}$ and dephasing time $T_{kl}$, or a non-equilibrium population state ($k = l$), which relaxes exponentially ($\omega_{kk} = 0$) with time constant $T_{kk}$ during $t_2$. Eqn. 3.4 gives a simplified description of the evolution during $t_2$, as multi-exponential relaxations of populations, as well as population or coherence transfers [46], may occur during this time interval.

3. The last pulse creates the coherence $\rho_{mn}$, which oscillates at frequency $\omega_{mn}$ during $t_3$.

The contribution of this pathway to the 2DES signal can be retrieved by performing a two-dimensional Fourier transform of Eqn. 3.4:

$$S_{R,NR}(\omega_1, t_2, \omega_3) = \int_0^\infty dt_1 \int_0^\infty dt_3 S(t_1, t_2, t_3) e^{\mp i\omega_1 t_1} e^{i\omega_3 t_3} \tag{3.5}$$

In this case, the negative sign is for rephasing and the positive one for non-rephasing. In the purely absorptive signal, this procedure results in a peak centered at $(\omega_1, \omega_3) = (\omega_{ij}, \omega_{mn})$:

$$S_{abs}(\omega_1, t_2, \omega_3) \propto \delta(\omega_1 - \omega_{ij}) e^{-(1/T_{kl}+i\omega_{kl})t_2} \delta(\omega_3 - \omega_{mn}) \tag{3.6}$$

If the state excited by the first pulse is the same probed by the last pulse, the ensemble is in the same coherence state $\rho_{ij} = \rho_{mn}$ during $t_1$ and $t_3$; excitation and detection frequencies are equal and the signal is a diagonal peak. If instead the state probed

by the last pulse is different from the state initially excited, the ensemble evolves in different coherent states $\rho_{ij} \neq \rho_{mn}$ during the two time intervals and a cross peak is created. Therefore, 2DES provides a direct way to detect coupling between states through the observation of off-diagonal peaks. It should be noticed that, in 2DES, the sign of the signals follows an opposite convention to that seen for TA: GSB and SE signals have positive sign, while ESA signals are negative.

The lineshape of the peak in Eqn. 3.6 is a delta function along the two frequency dimensions because dephasing was not taken into account. In real systems, however, the peaks are broadened due to dephasing processes occurring during time intervals $t_1$ and $t_3$: inhomogeneous dephasing causes an elongation along the diagonal direction, while homogeneous dephasing is quantified by the width of the peak along the anti-diagonal direction. For long enough waiting times $t_2$ between excitation and detection, the lineshape of the peaks gradually becomes more symmetric and rounded because spectral diffusion destroys the correlation between excitation and detection frequencies.

The evolution of the 2D maps along $t_2$ delivers salient information about relaxation dynamics. As mentioned above, if the system reaches a population state after the first two interactions, the signal evolves in $t_2$ following the relaxation dynamics of the excited states. If, on the contrary, a coherent superposition of states is created, the signal shows an oscillating and decaying trend in $t_2$. These superpositions can be electronic or vibrational in nature, and the ultrafast time resolution of 2DES should in principle allow to follow their temporal behavior, as well as to distinguish between them. Also, the signals arising from electronic and vibrational coherences appear in the 2DES maps according to different amplitude patterns [47, 48, 49, 50], thus providing a reliable strategy to assign them.

The analysis of cross peaks appearing in 2DES maps is an impressively powerful tool to investigate the energy flow within crowded systems. Donor and acceptor counterparts of an ET process can be directly revealed by the coordinates at which a cross peak appears; moreover, by determining the rate at which the intensity of a cross peak rises or decays, it is possible to unveil the timescale of an ET. Even more interestingly, cross peaks can sometimes uncover the dynamics of dark states coupled with bright states. Considerations of this kind will often be made in the coming chapters, showing how 2DES can reveal new insights on systems whose photophysics were found to be elusive to other techniques.

# Chapter 4

# Carotenoid-to-Chlorophyll Energy Transfer in Peridinin Chlorophyll *a* Protein[1]

Cars are pigments that are ubiquitously present in the LH apparatus of photosynthetic organisms, where they usually play the role of "accessory" pigments that ensure photoprotection and enhance the absorption of LH complexes in the green region of the solar spectrum [6]. In order for the energy absorbed by Cars to reach the reaction center, a prior transfer to the nearby Chls must occur; Car-to-Chl ET thus represents a fundamental step in the early events of photosynthesis, and yet many aspects of its mechanism remain unclear, mainly because of the dark character of the lowest excited electronic state, or states, of the Cars.

Due to symmetry considerations, the photophysics of all-trans-Cars is classically interpreted in terms of three states, namely, $S_0$, $S_1$, and $S_2$, with symmetries $1^1A_g^-$, $2^1A_g^-$ and $1^1B_u^+$, respectively [51, 52, 53]. In this picture, the excitation of the $S_2$ state is strongly allowed, while the $S_1$ state is symmetry-forbidden and can only be populated via rapid ($\sim$100 fs [54]) internal conversion. However, symmetry considerations alone do not account for the whole spectral complexity of Cars. First, the strong coupling of electronic and nuclear motions and the presence of possible asymmetric substitutions break the symmetry selection rules [55]. Moreover, some photosynthetic

[1] Chapter based on [14].

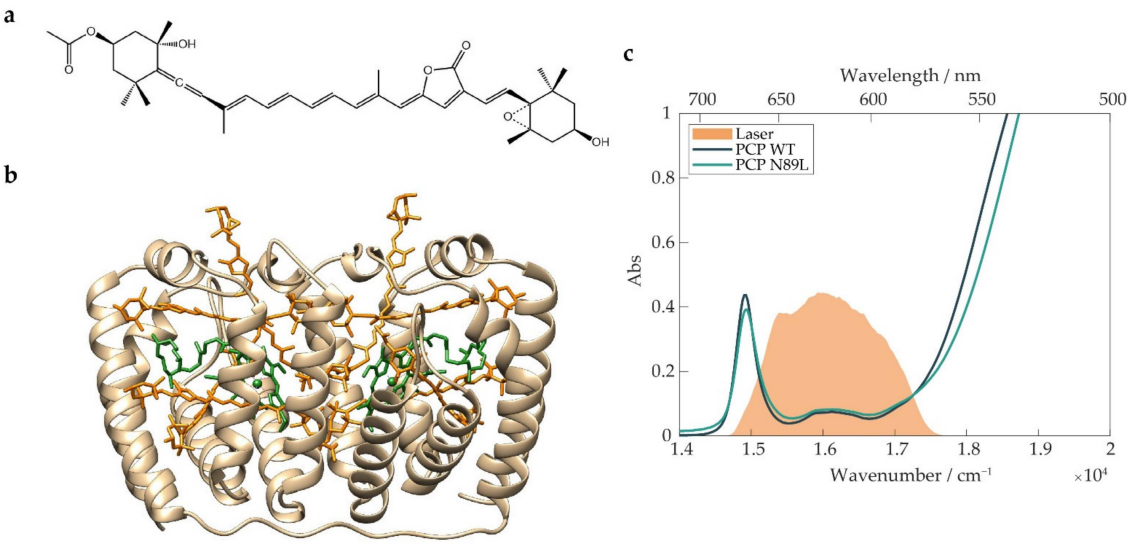


**Figure 4.1:** (a) Structure of the carotenoid Per. (b) Crystallographic structure of WT PCP, with the Per molecules colored in orange and the Chl *a* molecules colored in green. (c) Absorption spectra of WT PCP (blue) and its N89L mutant (green). The spectrum of the exciting pulses used in 2DES measurements is also shown (orange area).

complexes bind peculiar Cars, such as peridinin (Per), shown in Fig. 4.1a, in which an electron-withdrawing carbonyl group conjugated with the $\pi$-electron system stabilizes an intramolecular charge transfer (ICT) state [56, 57, 58, 59]. The relationship between ICT and the other electronic states was extensively discussed in the literature [60, 61, 62, 63, 64, 65], and it was often argued that an ICT character is associated with the dark $S_1$ state. Such an "$S_1$/ICT" state is believed to have an enhanced capability to act as an energy donor in photosynthetic ETs [66, 67, 68]. The picture was made even more intricate by the detection of further intermediate states between $S_2$ and $S_1$ [69, 70, 71, 72, 73], the most debated of which being the so-called "$S_x$" state. Some works interpret $S_x$ as an additional electronic state of ${}^1B_u^-$ symmetry [69, 74, 75, 76, 77, 78], while others describe $S_x$ as a distorted conformer on the $S_2$ potential energy surface, located in a local minimum [79] or near a transition state barrier between a planar and a twisted geometry [80, 81, 82, 83]. Whether $S_x$ also exists in free Cars in solution or only in Cars embedded in LH complexes, these works seem to converge on the interpretation of $S_x$ as a potential ET channel to the Chls.

## 4.1 Wild Type PCP and Refolded N89L Mutant

Intending to provide new pieces of evidence for the comprehension of Car-to-Chl ET, we focused our attention on PCP, a soluble antenna of dinoflagellate algae, which developed a unique strategy to maximize the efficiency of underwater photosynthesis [67, 13]. The wild-type (WT) form of PCP from *Amphidinium carterae* (Fig. 4.1b) is a heterodimer that binds a cluster of Per and Chl *a* molecules in an unusual 4:1 ratio [84] and aggregates into a trimeric quaternary structure. By exploiting the strong $S_2$ absorption of Per, PCP captures the green light that survives the overlying water column and then transfers energy to the Chl *a* with an ∼95% efficiency [85]. Per is thus the principal absorber in PCP, and the energy flow from Per to Chl *a* is the crucial step in the function of this complex. Early TA studies on PCP with an ∼100 fs time resolution showed that most of the energy is transferred to the $Q_y$ state of the Chl *a* in 2-3 ps [66, 67, 68, 85] via a Förster-like ET from the $S_1$/ICT state after internal conversion from $S_2$ has occurred. The same studies also demonstrated that a significant portion (∼25%) of the energy is delivered directly by the $S_2$ state of Per [86] before the internal conversion, possibly to the $Q_x$ state of Chl *a*. More recently, 2DES measurements have unveiled new details on the direct ET pathway from $S_2$, generating a debate on a possible coherent contribution to the ET [79, 87, 88, 89, 90].

The relative weights of the different ET channels, the factors affecting their efficiencies, and the involvement of further intermediate states of the Car in the ET are all open questions on the workflow of this one-of-a-kind antenna. A promising strategy to survey the photophysics of the PCP complex is to compare its WT form with refolded mutant complexes and assess whether and how the modification of specific structural and energetic features perturbs the energy flow between the pigments.

We carried out a comparative analysis of WT PCP and the refolded N89L mutant, in which asparagine-89, a residue close to the conjugated chain of Per-614, is replaced with leucine. The N89L mutant is a homodimer reconstituted from the N-terminal half of the PCP polypeptide. The comparison between the crystallographic structures of the N89L protein and the refolded PCP homodimer (RFPCP), which is the basis for the N89L variant, showed that the mutation does not affect the structure of the complex [91, 92]. Given the structural and spectroscopic equivalence between WT and RFPCPs [88, 93], the WT PCP itself can be used for a meaningful comparison with the N89L

mutant.

Per-614 is believed to be the Per of the cluster with the reddest energy site and the one showing the strongest interaction with Chl *a* [91]. The mutation shifts the red tail of the $S_2$ absorption band toward higher frequencies. This can be clearly seen by comparing the absorption spectra in Fig. 4.1c. A significant part of the oscillator strength of the band above 17000 $cm^{-1}$, which is associated with the $S_2$ transition, is blue-shifted in the mutant protein. Magnetic spectroscopies already demonstrated that the photoprotective function of Per-614 is preserved in the mutant despite the different energy sites of this pigment [93].

We investigated the excitation energy flow in the WT and N89L proteins in the ultrafast (<1 ps) time regime using 2DES. Thanks to a time resolution of about 10 fs and the inherent multidimensionality, 2DES overcomes most of the difficulties connected to the short time scales of photosynthetic ETs and the spectral congestion that is typical of multichromophoric systems. The work discussed in this chapter presents the first comparison of the WT PCP with its N89L mutant at the level of detail and with the temporal resolution offered by 2DES. Our approach confirmed that the study of specific mutations can be effectively used to extract crucial information on the photophysics of protein-bound Cars. Moreover, this comparison sheds new light on the Car-to-Chl ET mechanism; as will be extensively discussed in the next sections, the cooperation of multiple ET channels may be a key factor in ensuring the well-known, but hardly understood, efficiency of this process.

## 4.2 Results and Discussion

The laser spectrum used for 2DES measurements, shown in Fig. 4.1c, was tuned to cover (i) the $Q_y$ transition of Chl *a* (670 nm, 15000 $cm^{-1}$); (ii) the band at 620 nm (16100 $cm^{-1}$), which includes the contributions from the $Q_x$ transition of the Chl *a* and a vibronic $Q'_y$ transition; and (iii) the red tail of the $S_2$ transition of the carotenoid (<580 nm, >17000 $cm^{-1}$ ). The chosen bandwidth allowed us to capture possible signatures of coupling between Per and Chl *a* directly as cross-peaks in the 2DES maps. Moreover, this bandwidth acts as a spectral filter to specifically select the photophysics of the reddest Per within the cluster. We were thus able to selectively study the energy flow from the reddest Per to the Chl *a* and exclude from the analysis the processes through

which the excitation descended from the higher energy Pers to the lowest energy one. In this way, it was possible to focus our attention on the spectral region that is most affected by the mutation.

In Schulte et al. [91], the major contribution to the shift of the $S_2$ absorption band toward higher energies in N89L was associated with a destabilization of the two lowest lying excited states of Per-614 as a result of the lower-polarity environment around this pigment in the mutant. It was also suggested that this blue shift could be such that Per-614 is no longer the reddest in the cluster [91]. However, the attribution of the reddest $S_2$ transition to Per-614 provides only a simplified interpretation of the spectroscopic data: a more accurate description of the electronic structure of the cluster requires considering the formation of delocalized excitonic states [94], with the lowest energy one being localized mostly on Per-614 [90, 95]. In any case, it is worth highlighting that the interpretation of 2DES data is not affected by this attribution since the final aim was to provide information on the relaxation dynamics following photoexcitation of the reddest states of the Per cluster manifold.

Absorptive 2DES maps at selected values of the population time $t_2$ recorded at room temperature (295 K) are shown in Fig. 4.2. The diagonal signal centered at 15100 $cm^{-1}$ and the cross-peak at (16100, 15100) $cm^{-1}$ are the typical spectral signatures of the Chl *a*, as already discussed in previous work [89]. The former is assigned to GSB and SE of the $Q_y$ transition, while the latter is due to an internal conversion from the $Q_x$ to the $Q_y$ state, as well as a coupling of the $Q_y$ electronic transition with vibrational modes at $\sim$1000 $cm^{-1}$ [89, 96, 97]. In the following paragraphs, attention will be focused on the signals appearing at the excitation frequency of Per (17066 $cm^{-1}$), as these contain the information about the processes through which the excitation migrates from the $S_2$ state initially prepared down to the lower-lying states of Car, and eventually, to the Q bands of Chl *a* (Fig. 4.3a). Two signals appearing at this excitation frequency were of particular interest. First, the broad negative bands at the detection frequency >15500 $cm^{-1}$ (pinpointed with the square and the circle markers in Fig. 4.2), were attributed to ESA signals of Per. Second, the positive cross-peak at detection frequency of the $Q_y$ state of Chl *a* (15100 $cm^{-1}$ , triangle), which was direct evidence of the ET from Per to the $Q_y$ state of Chl *a*. When qualitatively comparing the spectra of the WT protein to those of the N89L mutant, no appreciable discrepancies could be observed in the positions of the signals. We then looked for possible differences in the dynamic

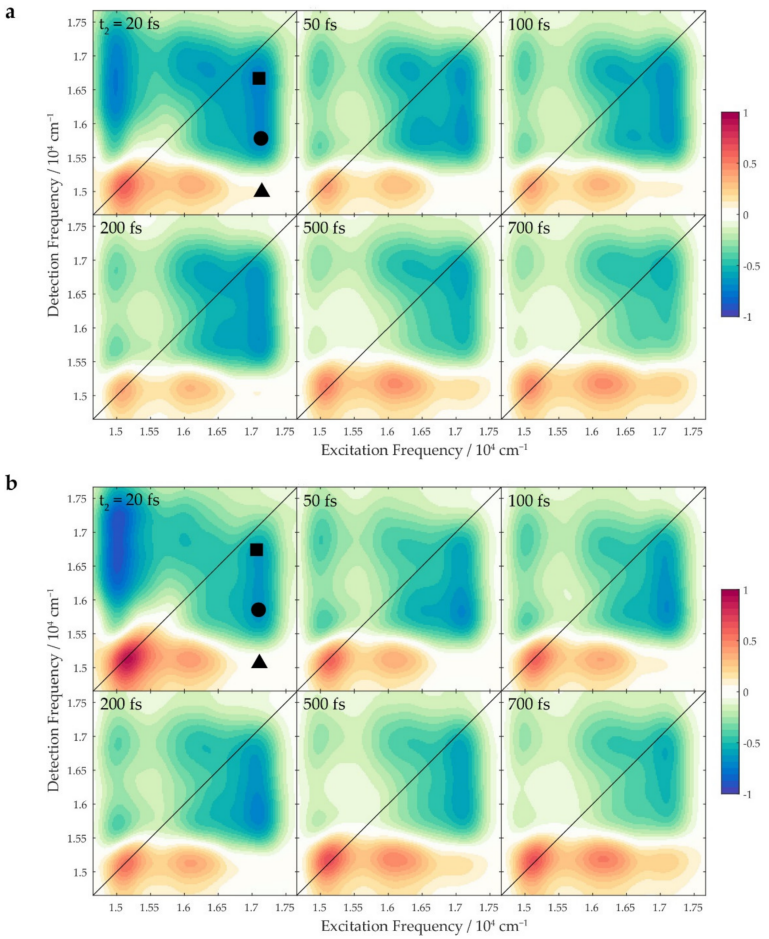


**Figure 4.2:** Absorptive 2DES maps of (a) WT PCP and (b) N89L PCP at different population times ($t_2$); to make the evolution of the populations more evident, the oscillating contributions to the signal were attenuated using a Savitzky–Golay filter. The markers pinpoint relevant coordinates discussed in the main text.

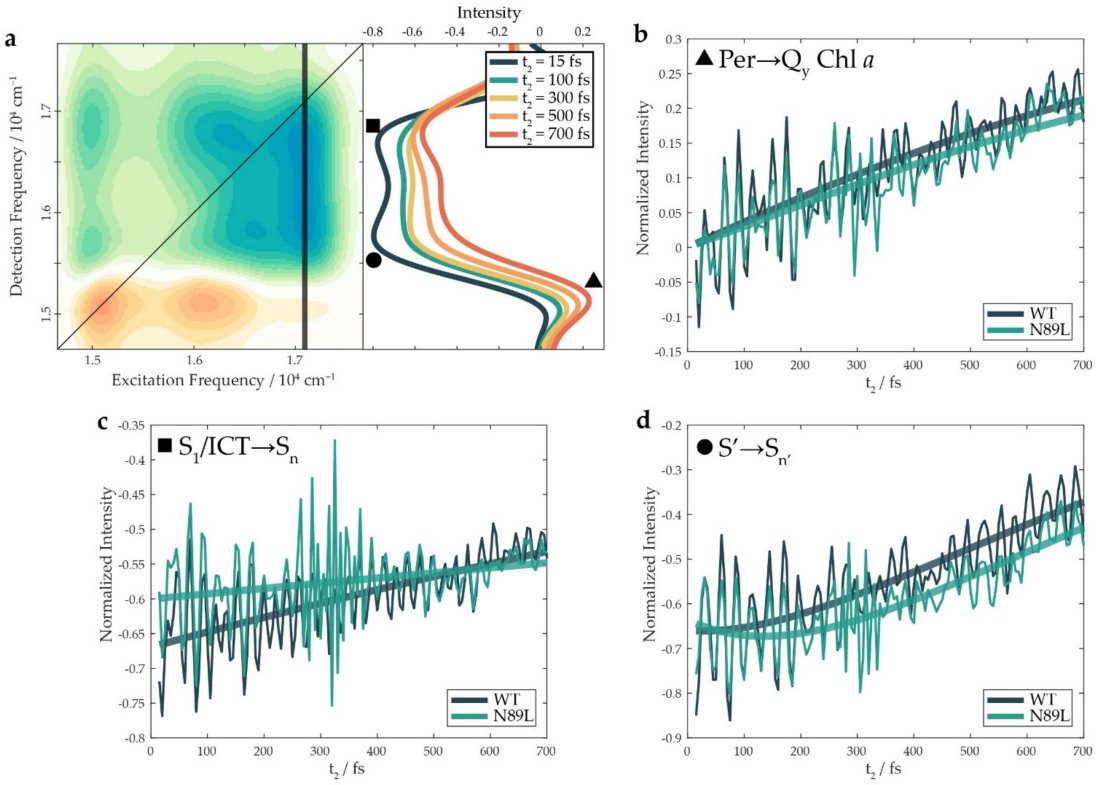


**Figure 4.3:** (a) Vertical cuts of the 2DES maps of WT PCP at excitation frequency 17066 cm$^{-1}$ (indicated with the black line) at different population times ($t_2$); to ease the visualization of the signal trends, the oscillating contributions to the signal were attenuated using a Savitzky–Golay filter. Temporal traces of (b) the ET signals (extracted at (17066, 15100) cm$^{-1}$, triangle), (c) the higher frequency ESA signals (extracted at (17066, 16700) cm$^{-1}$, square) and (d) the lower frequency ESA signals (extracted at (17066, 15850) cm$^{-1}$, circle) for the WT and the mutant samples. Thick solid lines represent the fittings performed according to a multi-exponential model (only the non-oscillating components are shown for clarity). The traces of the N89L sample shown in panels (b)-(d) exhibit a fast oscillation near 300 fs due to the interference between the scattering of the laser pulse and the local oscillator.

behavior of the signals.

The temporal traces shown in Fig. 4.3b–d were obtained by sampling the 2DES map at different combinations of excitation and detection frequencies and plotting the signal as a function of $t_2$. These traces show an intense beating behavior superimposed on the exponential trends: the analysis results presented below first show the population dynamics, while the oscillating components are addressed afterwards.

First, we studied the time evolution of the signal at the excitation frequency of Per and detection frequency of the $Q_y$ state of Chl *a* ((17066, 15100) cm$^{-1}$, triangle in Fig. 4.2). This signal can be associated with the ET from Per to the $Q_y$ state of Chl *a*, as graphically represented by the Feynman diagrams reported in Fig. 4.4. The intensity of the signal at these coordinates was increasing with increasing values of $t_2$, and the

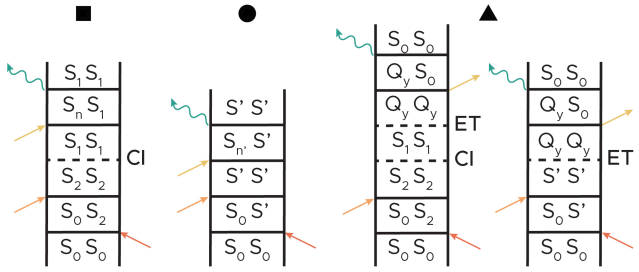


**Figure 4.4:** Double-sided Feynman diagrams contributing to the signals discussed in the text: ET from Per to Chl *a* (indicated by a triangle), higher ESA (square) and lower ESA (circle).

| | A1 | | T1/fs | | A2 | | T2/fs | |
|---|---|---|---|---|---|---|---|---|
| | WT | N89L | WT | N89L | WT | N89L | WT | N89L |
| ▲ ET signal | 0.80 | 0.76 | ~ 1900 | ~ 2000 | | | | |
| ■ Higher ESA | −0.70 | −0.62 | ~ 3000 | ~ 8000 | | | | |
| ● Lower ESA | 0.20 | 0.28 | 115 | 112 | −0.67 | −0.65 | 630 | 630 |

**Table 4.1:** Results of the parallel (multi)exponential models used to fit the traces at (17066, 15100) $cm^{-1}$ (triangle, ET signal), (17066, 16700) $cm^{-1}$ (higher ESA, square) and (17066, 15850) $cm^{-1}$ (lower ESA, circle); positive (negative) amplitudes indicate rising (decaying) components.

time constant regulating the signal rise thus provided an estimate of the effective rate of the ET. In the first place, we used a parallel (multi)exponential model to fit the temporal traces of the signals without introducing any a priori choice of a relaxation model. The results of the parallel fitting are summarized in Tab. 4.1. As shown in Fig. 4.3b, single exponential rises correctly reproduced the non-oscillatory dynamics, with time constants of about 1.9 ps and 2 ps for the WT and the N89L protein, respectively. These values are in the lower limit of the range reported in the literature for the $S_1$/ICT $\rightarrow Q_y$ ET [62, 66, 67, 68, 79, 85, 87, 88, 89]. Different from a previous study [89], the ultrafast, possibly coherent, ET pathway from $S_2$ could not be captured because of the different exciting conditions used here. Interestingly, the buildup of the ET signal in the mutant essentially retraced to the one in the WT, implying that the mutation did not induce significant changes in the rate of the ET process, at least in the first picosecond.

Moving the attention to the negative ESA signals, they most likely enclose contributions from different excited states of the Car, which cannot be easily identified based only on the coordinates. Indeed, the excitation frequency of these signals is that of the $S_2$ state initially prepared, but the ESA can take place from dark states reached after the ultrafast internal conversion from $S_2$; moreover, the detection frequency depends on the energy of the arrival state, which is generally unknown. Therefore, the identification of the electronic states contributing to the ESA must be based on the

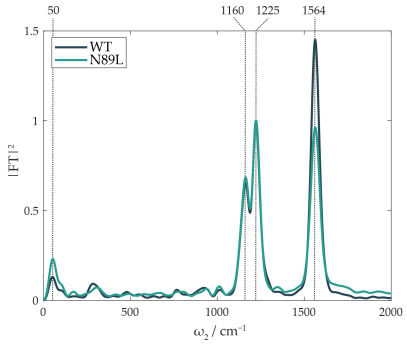


**Figure 4.5:** Fourier transform of the oscillating components of the 2DES signal, mediated along excitation and detection frequency axes. They are plotted as square moduli of the Fourier transform amplitudes and normalized on the intensities of the 1225 $cm^{-1}$ component.

dynamics of the signals. Fig. 4.3a clearly shows that the intensity of the ESA band was distributed in two "lobes": a lower detection frequency signal (indicated with a circle, "lower" ESA) peaking at (17066, 15850) $cm^{-1}$ and a higher detection frequency signal (square, "higher" ESA) peaking at (17066, 16700) $cm^{-1}$. Since the laser spectrum used for these measurements allowed for the excitation of the reddest Per state only, it is highly improbable that the two ESA signals arose from two different Pers. Instead, as is extensively discussed below, the two ESA lobes originated from different electronic states in the manifold of Per, as they showed different temporal dynamics.

The higher ESA signal for both the WT and the mutant proteins appeared within a time window comparable with the temporal resolution of the experiment (tens of fs). Moreover, as highlighted in Fig. 4.3c, this signal had a lower initial intensity for the mutant than for the WT. In agreement with previous evidence [89, 79], we attributed this signal to the $S_1$/ICT$\rightarrow$ $S_n$ ESA. Indeed, the immediate onset of this signal in both samples could be justified by invoking the presence of a Conical Intersection (CI) between the $S_2$ and the $S_1$ states [79]. The sub-10 fs population of the $S_1$ state through the CI from the initially excited $S_2$ explained why this negative signal was recorded immediately after excitation. The difference in the signal intensity at early times (Fig. 4.3c) could instead be associated with a lower quantum yield across this CI for the mutant than for the WT.

To investigate the factors affecting the yield of the crossing between the two electronic surfaces, we focused our attention on the vibrational degrees of freedom that were closely involved in the dynamics of the CI. Theoretical models describing CIs distinguish between coupling modes, which induce electronic coupling, effectively forming

the CI, and tuning modes, which tune the energy gap between the involved electronic states and thus regulate the access to the CI [98, 99, 100, 101]. Paramount information on the vibrational modes active in the CI can be found in the so-called "power spectra", shown in Fig. 4.5, which reveal the main oscillating components contributing to the 2DES signal. They are obtained by Fourier transforming the oscillating residues integrated over the two frequency dimensions [45]. The three most prominent beating components are all easily attributed to vibrational modes of Per; the contribution of the Chl to the power spectra is expected to be marginal due to the lower Huang–Rhys factor of its vibrational modes. The two vibrations at 1160 and 1225 $cm^{-1}$ are attributed to the C-C stretching mode of Per mixed with the C-H in-plane bending mode, while the vibration at 1564 $cm^{-1}$ is associated with the C=C stretching mode of the carotenoid [102, 103, 104]. It is noteworthy that the C=C stretching mode, already indicated as the tuning mode of the CI both in Cars [79, 100] and retinal [99], showed a reduced amplitude in the N89L mutant with respect to the WT protein.

It was argued that the C=C/C-C bond order reversal of the conjugated polyene backbone that accompanies the displacement along the C-C and C=C vibrational coordinates provides an ICT character to Per [60]. Therefore, after optical excitation of the $S_2$ state, the C=C stretching mode should push Per towards the CI in half a period of the vibration (∼10 fs) while developing an ICT character. The lower quantum yield of the CI could, thus, be ascribed to a poorer stabilization of the ICT character assumed by Per at the intersection between $S_2$ and $S_1$ in the lower polarity environment of the mutant. Indeed, the polarity-dependent stability of the ICT state is a well-documented feature [57] and was recently observed by Marcolin *et al.* [61] in the 2DES spectra of fucoxanthin, a carbonyl Car similar to Per.

An alternative interpretation of the higher ESA signal was provided by Beck and co-workers [80, 81, 82, 83, 87, 88, 90], who assigned it to the absorption of a displaced $S_2$ structure with a relatively long intrinsic lifetime labeled $S_x$ [87, 88, 90]. It is worth noting that this assignation is not in contrast with the key arguments discussed above. Indeed, they describe $S_x$ as an $S_2$ conformer with an ICT character, which is formed after the motion along the bond-length alternation coordinate C=C/C-C and initial twisting. In their picture, however, $S_x$ is formed immediately directly through the evolution in the $S_2$ potential energy surface and the CI between the $S_2$ and $S_1$ surfaces is only reached later. It should however be noted that in those works, a bluer excitation

profile was used, likely leading to the excitation of Per transitions that were different from the reddest transition addressed in our experimental conditions and, thus, to a slightly different dynamical evolution.

The second relevant difference between the WT and the mutant in the dynamics at the higher ESA coordinates was the time constants estimated for its decay, corresponding to the $S_1$/ICT relaxation (Tab. 4.1). The values of these constants were affected by a high uncertainty because they were much longer than the time window investigated (700 fs). Nonetheless, it can be clearly seen that the N89L mutant showed a significantly slower decay. Since it is known that the de-excitation of the $S_1$/ICT state is mainly promoted by transfer to the Chl in the ps time regime [66, 67, 68, 85], these data indicated a slower transfer to the $Q_y$ state of Chl *a* for the mutant. This could be reasonably ascribed to the poorer overlap between the $S_1$/ICT and the $Q_y$ band caused by the destabilization of the $S_1$/ICT state in the lower-polarity environment of the mutant. It is significant that because the rise of the ET signal is faster than the decay of the $S_1$/ICT ESA, then the $S_1$/ICT $\rightarrow Q_y$ transfer could not be the only channel exploited in PCP for the overall Per-to-Chl *a* ET.

When compared to the higher ESA, the temporal evolution of the lower ESA signal exhibited a different trend. It can be more properly fitted by using an exponential rise (115 fs) followed by a decay (630 fs). This indicated that the state from which the lower ESA originates was a different excited state in the manifold of Per. As mentioned above, intermediate Car states with different features (and labels) were reviewed in the literature [69, 70, 71, 72, 73, 105, 74, 79, 83]. We labeled the state generating the lower ESA as S' to remain general and postpone the definitive identification of this state to a future, more targeted study. The notable intensity of the lower ESA at early times in Fig. 4.3d suggested that S' could have been directly excited by the laser pulse. A possible assignation of S' would be a distorted $S_2$-like state excited via transitions from twisted ground-state conformations, presumably favored by the protein scaffold and expected to lie in the red-edge of the Per absorption [82, 106, 107].

Moreover, the dynamic behavior in Fig. 4.3d indicated that an additional population could be brought into S' within a few hundreds of fs, possibly via a torsional motion from the "proper" (planar, all-trans) $S_2$ state. Indeed, the population of twisted carotenoid structures through torsional distortion of Per in the $S_2$ state is a hypothesis that is commonly reviewed in the literature [69, 70, 80, 81, 82, 83]. In support of this

hypothesis, we noticed that the peak at ∼50 $cm^{-1}$, which is recognizable in the power spectra of Fig. 4.5, could be attributed to a low-frequency torsional mode. Although the characterization of an oscillating component at such a low frequency is hampered by the narrowness of the time window, it is noteworthy that a vibrational coherence peaking at a similar frequency was detected in retinal, which has an analogous polyene backbone [99, 108]. Such a torsional mode could guide Per to the S' state within half a period of oscillation (∼350 fs), passing through a series of intermediate distorted structures. Our experimental observations on S' agreed with several already recognized properties of the $S_x$ state, above all, its capability to directly transfer energy to Chl [82, 106, 107]. This evidence points toward the assignation of the decay of the lower ESA to the S'→$Q_y$ ET process. In addition, as summarized in Tab. 4.1, the fitting of the lower ESAs highlighted a higher amplitude of the rising component for the N89L mutant. This was compatible with a larger $S_2$ population that survived the CI and underwent torsional distortion to the S' state. The higher intensity of the low-frequency torsional mode in the power spectrum of the mutant (Fig. 4.5) also seemed to correlate with the greater population that reached the distorted S' state.

We want to highlight that an alternative interpretation of S' as a vibrationally "hot" $S_1$/ICT state cannot be excluded. A hot $S_1$/ICT state could be directly excited by borrowing oscillator strength from the almost-resonant $S_2$ transition and further populated by internal conversion. Moreover, the involvement of a vibrationally excited $S_1$/ICT state as an additional channel for the ET process was already proposed [66].

Altogether, these findings suggested the presence of at least two synergic pathways contributing to the overall ET from Per to Chl *a* in the investigated time and frequency range. Indeed, we could exclude the idea that in these conditions, the only channel was the $S_1$/ICT→ $Q_y$ transfer because the rise of the ET signal (triangle, Fig. 4.3b) was faster than the decay of the $S_1$/ICT ESA (square, Fig. 4.3c). Moreover, the overall ET rate, estimated as 1.9 and 2 ps for the WT and the mutant, respectively (4.1), remained practically unchanged in the two samples, despite the slower decay rate of $S_1$/ICT in the N89L mutant. We thus proposed a kinetic model, like the one represented in Fig. 4.6a, in which the $S_1$/ICT and S' states cooperate to transfer energy to the $Q_y$ state of Chl *a*. Based on this kinetic scheme, it was possible to devise a new fitting model that allowed for retrieving the kinetic constants associated with each of the identified transfer pathways and their relative weights for the WT and the mutant, as illustrated

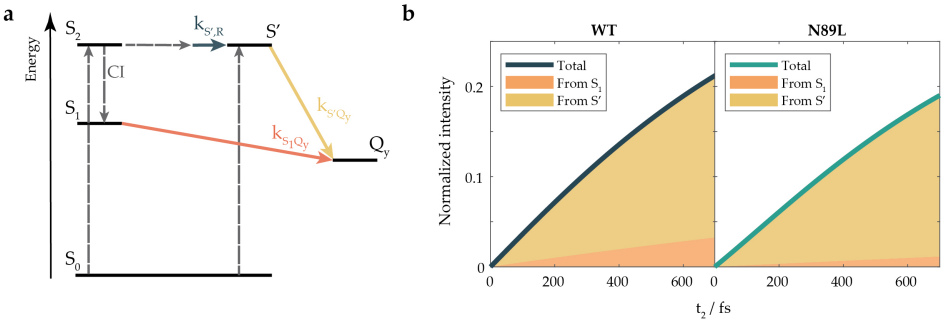


**Figure 4.6:** (a) Energy level diagram illustrating the different dynamic processes included in the kinetic model used to interpret the temporal dynamics of the experimental traces. Dashed lines indicate events occurring on a time scale faster or comparable with the time resolution of the experiment, namely, the initial optical excitation and the decay of the $S_2$ state via (i) the CI that transferred the population from $S_2$ to $S_1$ and (ii) the initial torsional movements that promoted the formation of distorted structures. $k_{S',R}$, $k_{S_1Q_y}$ and $k_{S'Q_y}$ represent the kinetic constants for the rise of S', the $S_1$/ICT$\rightarrow$ $Q_y$ ET, and the S'$\rightarrow$ $Q_y$ ET, respectively. (b) Contributions to the rise of the ET signal, as determined by the fitting of the experimental data using the kinetic model in panel (a).

in Fig. 4.6b. The results obtained after applying this kinetic model clearly outlined that the mutation did not alter the kinetic constants relevant for the ET; instead, the ET rate was preserved thanks to a redistribution of the relative weights of the two ET channels.

Indeed, according to the model in Fig. 4.6a, once the reddest Per was excited in the $S_2$ state, part of the $S_2$ population was transferred to the $S_1$ state through a CI in a timescale comparable with the temporal resolution of the experiment. The CI exhibited a lower yield in the mutant, possibly because of polarity or steric effects affecting the vibrational mode that regulated access to it. The excitation energy was then transferred from $S_1$ to the $Q_y$ state of Chl *a* in a few ps ($k^{-1}_{S_1Q_y} \sim 3$ ps in the WT protein, ~8 ps in the mutant). In parallel, the population in $S_2$ was pushed via torsional motions through a series of distorted structures. Eventually, this led to the rise of a state labeled S' on a time scale of $K^{-1}_{S',R} = 409$ fs (395 fs in the N89L mutant). From S', the excitation energy could be efficiently transferred to the Chl *a*, with a calculated time constant of $k^{-1}_{S'Q_y} =$ 501 (503) fs for the WT (N89L) sample. Altogether, during the first 700 fs, in the WT, ~85% of the excitation was transferred to the Chl *a* starting from the S' state, while

the remaining 15% came from the $S_1$ state, as shown in Fig. 4.6b; the contribution from S' was more significant in the mutant (∼94%) due to the larger population that survived in $S_2$ and moved to S'. Overall, the ET process in the N89L mutant suffered only a slight slowdown thanks to the compensating effect of the S' channel.

## 4.3 Final Remarks

The comparison of the ultrafast dynamic behavior of the WT PCP and a refolded N89L mutant allowed unveiling important information about the workflow of this light-harvesting complex. While previous studies have already shown that the N89L mutation does not affect the ET efficiency [91], here we shed light on the mechanisms underlying such robustness. By exploiting the multidimensionality of the 2DES technique, two parallel channels for the ET could be identified: along with the well-documented pathway from the $S_1$/ICT state, transferring excitation to the $Q_y$ band of the Chl *a* in a few ps [66, 67, 68, 85], we recognized the crucial role of a further intermediate state donating energy in the first hundreds of fs after photoexcitation. This second channel becomes more relevant in the mutant, where the $S_1$/ICT channel was partially undermined because of the mutated energy landscape. These findings suggest that the cooperation of multiple pathways might be decisive in ensuring high ET performance even if a pathway is compromised to a certain degree. Although this conclusion was drawn from data collected in specific experimental conditions, recent evidence in the literature seems to indicate that, in effect, it might have more general validity.

First, other works have demonstrated the robustness of the ET in PCP against the replacement of Chl *a* with different Chls [90, 109]. Second, the overview of the most recent 2DES works on PCP revealed that different exciting conditions might favor specific deexcitation pathways above others by preparing different initial states of the Per donor. The exciting conditions used in this work placed a magnifying glass on the photophysics of Per structures in the red edge of the spectrum, which can be reasonably associated with distorted carotenoid geometries, possibly designed by the protein environment. Their contributions to the spectroscopic signal would have been elusive with a bluer laser band. Indeed, with a more significant excitation of the $S_2$ state, the direct $S_2 \rightarrow Q_y$ ET channel and the population of the $S_1$/ICT state from $S_2$ via CI would have become the dominant de-excitation pathways. The strong sensitivity

of the spectroscopic response to the exciting conditions also justifies, for example, the multifarious interpretations proposed for the "$S_x$" state and its role in the ET, and the number of different possible ET pathways so far identified [79, 87, 88, 89, 90]. Upcoming analyses with a greater focus on the amplitude and phase distribution of the Car vibrational modes over the 2DES map could provide more definitive evidence on the identity of the states detected in 2DES measurements.

Beyond implying that particular care must be paid in the comparison of literature data, this vast wealth of investigations is progressively unveiling the complexity and multiplicity of the mechanisms regulating the efficiency of ET in the PCP antennae. The photophysical properties of PCP have carefully evolved to be robust against mutations potentially threatening its light-harvesting function.

From a broader perspective, it is likely that the diversity and complementarity of channels available for the ET may be a common strategy affecting the robustness of photosynthesis on a biologically relevant scale. Future investigations on other natural antennae would help understand whether Car-to-Chl ET mechanisms similar to the one described in this work for PCP are also relevant in LH complexes different from PCP.

# Chapter 5

# Chromatic Adaptation of *Chromera velia*

The alveolate alga *C. velia* provides a fascinating example of chromatic adaptation, namely the capability of sensing and responding to changes in the environmental light. The principal antenna from *C. velia*, called Chromera Light Harvesting (CLH) complex, is a transmembrane protein which binds Chl *a*, an isofucoxanthin-like (Ifx-l) carotenoid and Violaxanthin (Vlx) in a 5-7:2:1 ratio [110]. The structure of CLH has not been determined yet. Based on sequence homology, CLH is supposed to be similar to the light harvesting complexes of other unicellular algae, in particular Fucoxanthin Chlorophyll $a/c$-binding Protein (FCP), whose crystallographic structure was recently published [111].

The CLH complex cannot absorb light in the far-red ($> 700$ nm). However, when grown under far-red light, *C. velia* expresses an oligomer with enhanced capability of absorbing light above 700 nm, which is therefore called red CLH (rCLH) [16]. When it comes to collecting energy in the far-red, photosynthetic proteins often use Chl *d* and *f* [112, 113], which have more red-shifted absorption spectra if compared to Chl *a*. Nevertheless, like CLH, rCLH only contains Chl *a* and therefore the presence of red-shifted states has to rely on different strategies. For example, the protein scaffold can finely-tune the energy site of a bound pigment via pigment-protein interactions; alternatively, lower energy states can be obtained by exploiting excitonic or Charge-Transfer (CT) interactions between the pigments [113]. The absence of a crystal structure makes it more challenging to understand the origin of the far-red absorption in rCLH. Far-red

states in antenna proteins that do not contain Chls *d* or *f* were already characterized in the LH complex Lhca4 of photosystem I from higher plants [114, 115, 116]. In that case, the far-red shift was shown to be due to an intermolecular CT interaction within a specific Chl dimer. The establishment of such interaction was ascribed to the presence of an Asn residue as a ligand for one of the two Chls of the dimer, in place of a His residue which is conserved in all other higher plant antenna complexes [114]. As a consequence of their CT nature, the emission from these far-red Chl states is characterized by a large (∼25 nm) Stokes shift [117, 115]. With respect to the red forms of Lhca4, the emission from the far-red absorbing state of rCLH exhibits a considerably smaller Stokes shift (absorption at 708 nm, emission at 717 nm [16]); moreover, the His-to-Ans substitution which was proven to be necessary for the CT interaction in Lhca4 is absent in the rCLH antenna [15]. Hence, the emergence of far-red states in rCLH can be expected to stem from a different mechanism from the one documented for the antennas of higher plants.

With the aim of gaining additional clues on the nature of far-red absorbing state (or states) of rCLH, 2DES experiments were performed. To avoid degradation of the antenna, the sample was measured at cryogenic temperatures (77 K), in a solution consisting of 60% of degassed glycerol and 40% of a buffer containing $\beta$-dodecyl maltoside. We investigated a time window that included the first picosecond from photoexcitation, with a time resolution of ∼10 fs.

## 5.1 Results and Discussion

The 77 K absorption spectrum of the CLH complex, in Fig. 5.1a, exhibits the Chl *a* Soret transitions at 420 and 436 nm, while the $S_2$ transitions of the carotenoids can be found at longer wavelengths, up to 600 nm; at 625 nm, the $Q_x$ bands and the vibronic sidebands of the $Q_y$ transitions of Chls *a* can be found, while the $Q_y$ transition band peaks at 677 nm.

The rCLH antenna expressed as a result of adaptation to red light contains the same pigments, albeit in different proportions, with Vlx being more abundant than Ifx-l [16]. The major change in the absorption spectrum, apart from different relative intensities of the peaks in the carotenoid region, is the presence of an absorption peak in the far red, at 708 nm, as evident in Fig. 5.1b. For the measurements discussed in this chapter,

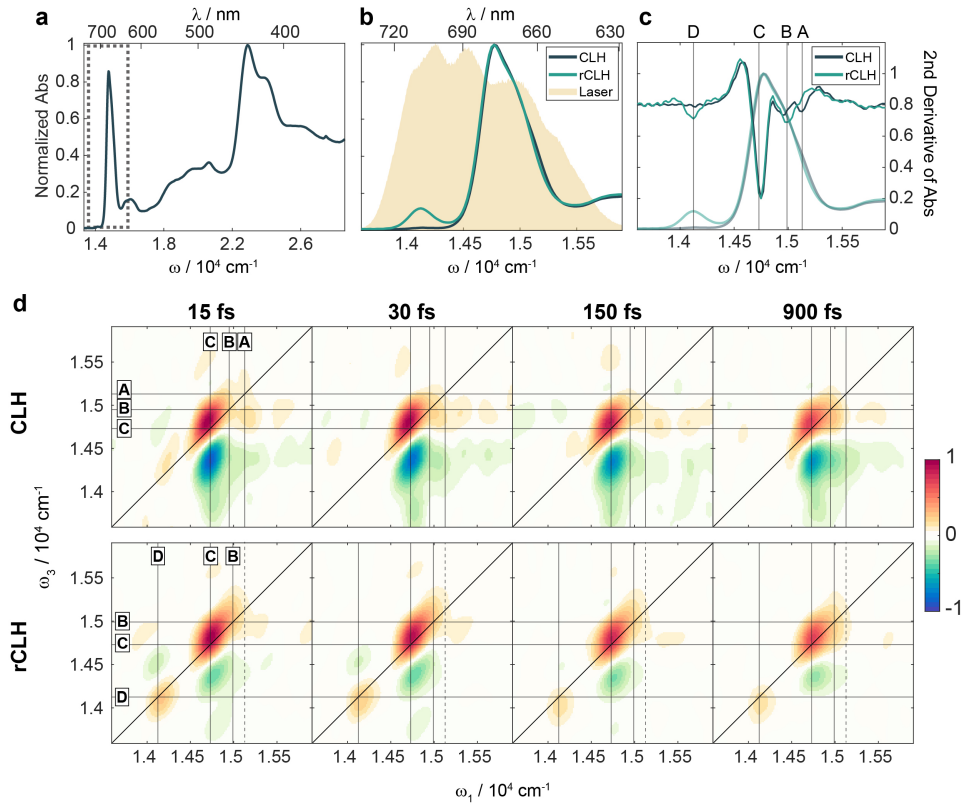


**Figure 5.1:** (a) 77 K absorption spectrum of CLH. The dashed rectangle highlights the region of the spectrum magnified in panel (b). (b) Comparison between the 77 K absorption spectra of CLH and rCLH in the spectral region investigated via 2DES; the laser spectrum is shown as a yellow area superimposed on the absorption spectra. (c) Second derivative of the 77 K absorption spectra of CLH and rCLH. Vertical lines indicate the positions of the local minima, corresponding to the central frequencies of a series of pools of Chl states, as listed in Tab. 5.1. (d) 2DES maps of CLH and rCLH at 77 K for selected $t_2$ times. Vertical and horizontal lines indicate the central frequencies of the pools of Chl states identified as in panel (c) and listed in Tab. 5.1. The dashed vertical lines indicate the excitation frequency at which the contributions of pool A would be expected if this pool was present in rCLH.

| | A | B | C | D |
|---|---|---|---|---|
| **CLH** | 15130 | 14950 | 14730 | - |
| **rCLH** | - | 14990 | 14730 | 14125 |

**Table 5.1:** Central wavenumbers, in $cm^{-1}$, of the pools of Chl states identified via second derivative of absorption spectra of CLH and rCLH at 77 K (Fig. 5.1c).

the laser bandwidth was tuned to cover a spectral region centered at 670 nm and ∼110 nm broad. As illustrated in Figs. 5.1a and b, this choice allowed to focus the analysis on the $Q_y$ bands of the Chls, where the most significant differences between the two protein forms have been identified.

The asymmetrical shape of the $Q_y$ band at 677 nm, in both samples, suggests that this band encloses the contributions of differently absorbing Chls. As for the far-red absorption band, the electronic structure of the Chl pools contributing to this band is not known, nor is it clear whether couplings exist such that delocalized excitations can be defined. In the following, we will consider that each Chl pool corresponds to a manifold of states, to which we associate an average energy value, based on the analysis of the UV-Vis spectra at 77 K (Fig. 5.1b) and their second derivative (Fig. 5.1c). Firstly, a modest local minimum at 15130 $cm^{-1}$ can be recognized in the second derivative spectrum of CLH, while the same feature is not as noticeable in rCLH: this would suggest the presence, in CLH, of a Chl pool (hereafter indicated as pool A) that could be absent from the acclimated rCLH sample. Moreover, the excitation spectrum of rCLH at 77 K [16] allows to recognize two spectrally distinguishable Chl pools, one peaking at 667 nm (14990 $cm^{-1}$, pool B) and one at 679 nm (14730 $cm^{-1}$, pool C). These values are in agreement with the positions of the local minima of the second derivative spectra shown in Fig. 5.1c. The comparison between the second derivative spectra of CLH and rCLH, however, hints that pool B might be slightly red-shifted (14950 $cm^{-1}$) in the CLH sample. Finally, the far-red (708 nm, 14125 $cm^{-1}$) absorbing Chls, exclusive of the rCLH antenna, will be indicated as pool D. Tab. 5.1 summarizes this nomenclature.

Figure 5.1d compares the 77 K 2DES spectra of CLH and rCLH at selected $t_2$ values. In both samples, it is possible to recognize a positive diagonal band containing the SE and GSB signals of the Chl pools contributing to the absorption band at 677 nm. The appearance of a negative band below the diagonal, attributed to the ESA from the same pools, distorts the shape of the positive signal along the $\omega_3$ direction, in such a

way that it appears slightly tilted above the diagonal, with the intensity maxima being at "pseudo-diagonal" positions for $\omega_3 > \omega_1$. The increased intensity of the ESA around $\omega_1$ ∼15130 cm$^{-1}$ in the map of the CLH sample may be a signature of the exclusive presence of pool A in this sample, as suggested by the second derivative spectra (Fig. 5.1c). The main difference between the 2DES spectra of CLH and rCLH concerns the presence of additional bands at $\omega_1 = 14125$ cm$^{-1}$ in the case of the acclimated rCLH oligomer. These low excitation frequency bands arise from the excitation of the far-red absorbing pool D. It can be noticed that bands peaking at similar frequencies can also be recognized in the 2DES map of the CLH sample at 15 fs (Fig. 5.1d), although their intensity is slightly above noise and they disappear at longer times. A band at ∼15150 cm$^{-1}$ is barely visible also in the absorption spectrum of CLH. These weak spectral features are likely due to the presence of rCLH impurities in the CLH sample: indeed, the rCLH oligomer can also be expressed under natural illumination, albeit to a lesser extent, and it is possible that the purification procedures did not fully separate the rCLH fraction from the CLH sample. Interestingly, only in the case of the rCLH sample, the tail of the ESA at low $\omega_3$ values seems to be partially canceled in a region roughly corresponding to excitation of C and detection of D. This feature allows to indirectly spot a positive cross-peak, which, as extensively discussed below, is likely to arise from an Energy Transfer (ET) from C to D.

The inspection of 2DES maps of rCLH at different $t_2$ values makes evident that the low excitation frequency band, associated with pool D and highlighted by the rectangle in Fig. 5.2a, broadens below the diagonal already in the first tens of fs. The broadening of the low-energy band D below the diagonal is analyzed in detail in Fig. 5.2b, where the intensity of the signals extracted at $\omega_1 = 14125$ cm$^{-1}$ and different values of $\omega_3 < \omega_1$ is plotted against $t_2$. Near the diagonal, the signals decay rapidly, with a time constant of 42 fs, while below the diagonal the signals rise with the same time constant. An additional exponential decay, with a much longer time constant (» 1 ps), was added to the fittings to account for processes occurring on a time scale exceeding the investigated time window. The information on the above-mentioned ultrafast process can be retrieved in a more consistent way by performing a global fitting of the lower excitation energy region of the map, enclosed in the rectangle in Fig. 5.2a. In a global analysis, all the temporal traces extracted from a specific area are fitted using a set of shared time constants and variable amplitudes [45]. The result of the global fitting is a Decay Associated Spectrum (DAS) for each exponential component used for the fitting.

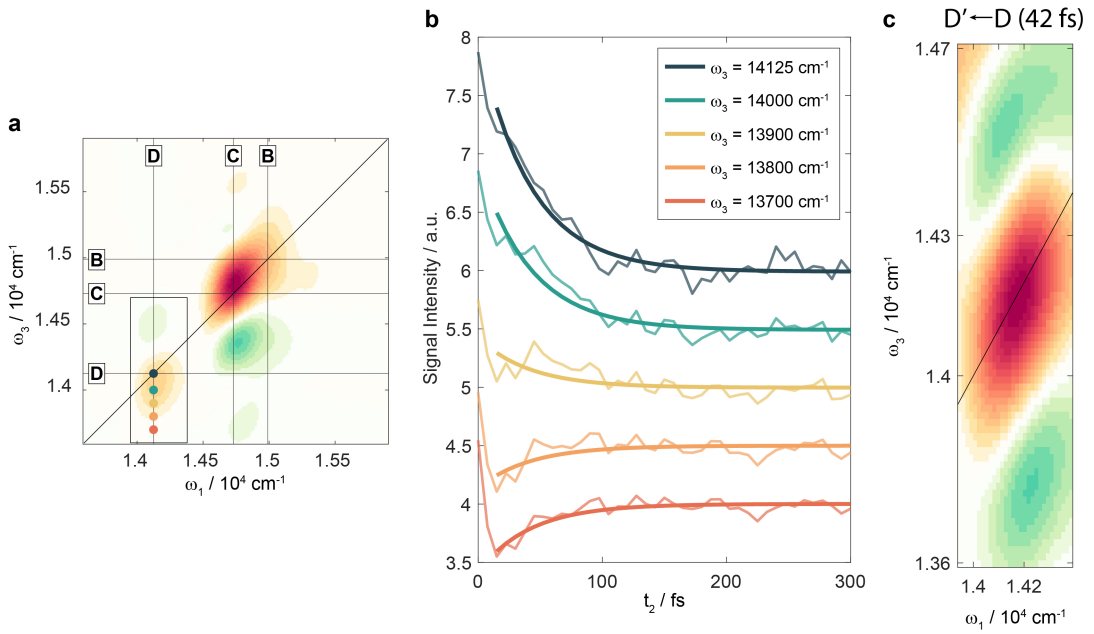


**Figure 5.2:** (a) 77 K 2DES map of rCLH, mediated along $t_2$. Vertical and horizontal lines indicate the central transition frequencies of the Chl pools listed in 5.1. (b) Temporal traces of the signals extracted at coordinates $\omega_1 = 14125$ cm$^{-1}$ and different values of $\omega_3$, corresponding to the circles in panel (a). A vertical offset was added to the traces to ease the visualization. (c) DAS of the 42 fs exponential component, obtained through a global fitting of the region of the 2DES map enclosed in the rectangle in panel (a). The red color indicates positive amplitudes, while the green-blue color indicates negative amplitudes.

A DAS is a two-dimensional plot that shows how the amplitude of a certain exponential component varies within the map. The DAS associated with the 42 fs exponential component is shown in Fig. 5.2c: the red color indicates a positive amplitude, and therefore the decay (rise) of a positive (negative) signal, while the blue color indicates a negative amplitude, and therefore the rise (decay) of a positive (negative) signal. Although the shape of this DAS may be reminiscent of those typically associated with spectral diffusion, in this case the negative signal above the diagonal is likely to arise from the decay of the ESA in that region; moreover, the process described by this DAS is too fast to be interpreted as spectral diffusion [118]. Therefore, it is reasonable to assume that the DAS in Fig. 5.2c shows a partial redistribution of the intensity of the signal from the diagonal position to lower emission frequencies. Similar dynamics in Chl aggregates were attributed to a downhill energy relaxation within excitonic domains [119]. Moreover, the appearance of an ESA band at higher emission energies is characteristic of transitions between exciton levels of Chl aggregates [120]. In fact, in the hypothesis that the states of pool D are excitonic in nature, the energy of the transition from the one-exciton to the two-exciton band, probed by the last pulse, is expected to be higher than the energy of the transition from the ground state to the one-

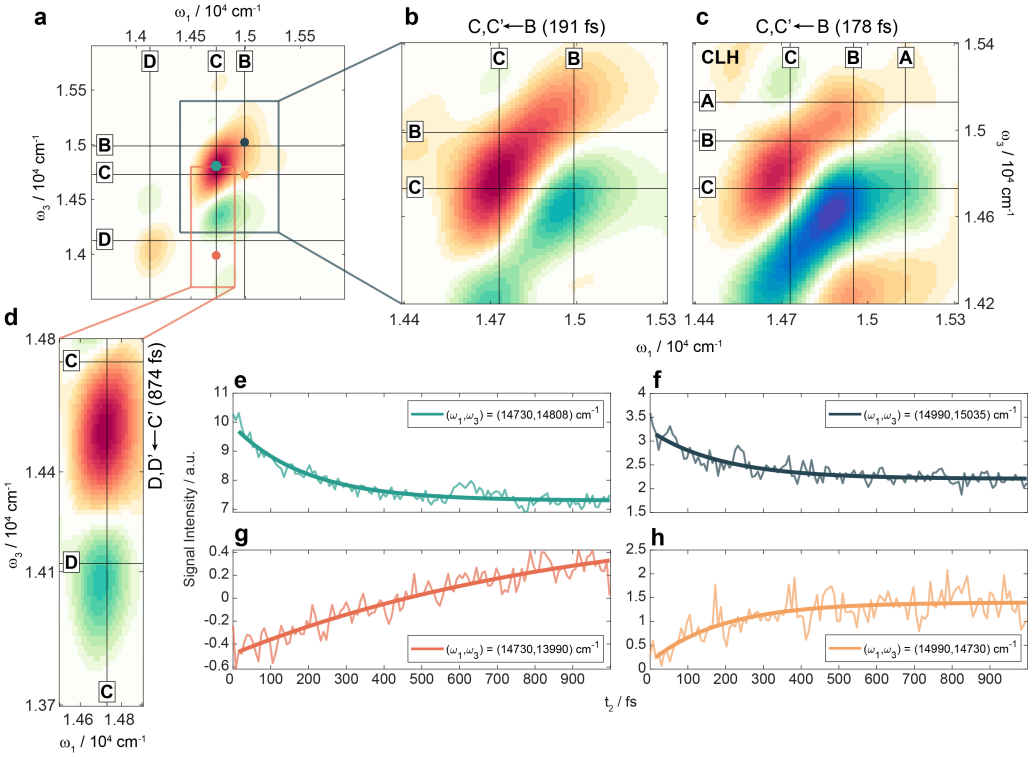


**Figure 5.3:** (a) 77 K 2DES map of rCLH, mediated along $t_2$. Vertical and horizontal lines indicate the central transition frequencies of the Chl pools listed in Tab. 5.1. (b) DAS of the 191 fs exponential component, obtained through global fitting of the region of the map enclosed in the blue rectangle in panel (a). If a global fitting of the CLH sample in the same region of the map is performed, a 178 fs component is retrieved. The corresponding DAS is shown in panel (c). (d) DAS of the 874 fs exponential component, obtained through global fitting of the region of the map enclosed in the orange rectangle in panel (a). The red color indicates positive amplitudes, while the green-blue color indicates negative amplitudes. (e)-(h) Temporal traces of the 2DES signals extracted at selected coordinates, indicated by the circles in panel (a). Thick lines represent the fitting curves obtained via global fitting.

exciton band, excited by the first pulse [121]. Overall, these observations suggest that the far-red absorbing pool D constitutes an exciton manifold and that the population created by direct excitation at 14125 cm$^{-1}$ is redistributed over lower energy states of the manifold (which will be indicated with D') with a time constant $\mathrm{T}_{D' \leftarrow D} = 42$ fs.

The higher excitation energy region of the 2DES maps, containing the signals arising from the excitation of pools A, B and C, is analyzed in Fig. 5.3. Firstly, it is possible to notice that, in contrast to the ESA band from D, the ESA from these pools appears at lower $\omega_3$ values than the corresponding bleaching bands. This might be the consequence of a different orientation of the $\mathrm{Q}_y$ transition dipole moments of the Chls of these pools [122], if compared to the Chls of pool D. Alternatively, it is possible that the observation of an ESA band below the diagonal, rather than above, results from the use of a laser band that does not cover higher energy ESA transitions, which would appear above

the diagonal, and rather highlights ESA transitions which fall in its center.

Valuable pieces of information on Chl pools A-C can be gained through the analysis of the temporal dynamics of the high excitation energy region of the 2DES maps. The colored rectangles in Fig. 5.1a delimit the portions of the 2DES spectra on which global fitting procedures were performed, resulting in the DAS reported in panels (b)-(d); temporal traces at selected points are instead shown in panels (e)-(h), together with the corresponding fitting curves. The global fitting of 2DES data from rCLH, in the region enclosed in the blue rectangle in Fig. 5.3a, revealed a 191±8 fs exponential component, besides a long-time decay (» 1 ps). The DAS of the 191 fs component is shown in Fig. 5.3b. This component well describes the short-time decay of the positive pseudo-diagonal peaks at (14730,14808) $cm^{-1}$ (Fig. 5.3e) and (14990,15035) $cm^{-1}$ (Fig. 5.3f). The long-time component accounts for the fact that the decay is not concluded within the investigated time window, in accordance with the observation of fluorescence at 686 nm, from the $Q_y$ bands of the Chl pools B and C, in the ns time scale [16]. The DAS of the 191 fs component shows a similar structure to the one reported in Fig. 5.2c, with negative features that appear at lower $\omega_3$ values, indicating the rise of positive signals below the diagonal. As already discussed, this could be the signature of a downhill energy relaxation within excitonic manifolds, corresponding to pools B and C. However, in this case, the DAS may also account for other concomitant dynamics. Indeed, the negative feature at (14700,14200) $cm^{-1}$ may be attributed both to the decay of the negative ESA signal from pool C, and to the relaxation of population to lower energy exciton states within the manifold of C (C'). Analogously, the rise of the signal at coordinates (14990,14730) $cm^{-1}$ (Fig. 5.3h) can originate from the relaxation within manifold B, as well as from the ET from pool B to C. Overall, the energy relaxation within each manifold may not be distinguished from the transfer of the excitation between neighboring domains and the DAS for the 191 fs time component may summarize both these phenomena.

The global fitting procedure, performed on the same area of the 2DES maps of CLH, revealed analogous dynamics with a similar time constant (178±20 fs). The corresponding DAS is reported in Fig. 5.3c. This suggests that the relaxation dynamics from B to C and within C are negligibly affected by the structural differences existing between CLH and the oligomeric rCLH sample. In other words, 2DES data hint that the electronic structure of pools B and C is conserved in the two antennae. However,

when comparing the two DAS in Fig. 5.3b and c, it is possible to spot a difference in the positive feature at $\omega_1$ corresponding to excitation of pool B and $\omega_3$ ∼14200-14300 $cm^{-1}$. This feature describes the rise of a negative signal within the time scale that we have associated to the ET from B to C and, even though present in the DAS of both samples, is much more evident in CLH. This signal can be attributed to the rise of an ESA from pool C after excitation of pool B; its lower relative intensity in the case of rCLH may be a consequence of the fact that, in this sample, pool C can be depopulated by ETs to lower-energy states, as previously anticipated. Finally, it should be noticed that, in the DAS of CLH, the peaks have a more asymmetrical shape, being elongated towards higher excitation frequencies, near 15130 $cm^{-1}$, where pool A is supposed to contribute. Thus, in the CLH sample, the dynamics of pool A could not be distinguished from that of pools B and C. Also considering the energetic proximity of pool A to pool B, it cannot be ruled out that pools A and B may be more appropriately described as substructures of a single Chl pool, rather than two separate pools.

It is relevant to notice that the intra-manifold downhill energy relaxation is significantly slower in the case of the higher-energy manifolds B and C than in D (191 vs 42 fs). Since the relaxation dynamics strongly depends on the interaction with the environment [123], it is reasonable to hypothesize that the B and C pools might be more shielded from the fluctuations due to interactions with the environment, if compared to pool D. This in turn would imply that the Chls of pool D may be located in a region of the complex more exposed to the solvent, thus suggesting that this pool originates upon an oligomerization process. In addition, the circular dichroism spectrum of rCLH exhibits a feature at 705 nm which disappears when the oligomer is dissociated into its forming monomers [16]. This supports the hypothesis that the appearance of the far-red absorption band is related to inter-subunits interactions within the oligomer. All these pieces of information point towards the attribution of the far-red absorbing states to Chls at the interface between different subunits of the oligomer.

Then, possible couplings between high energy and low energy pools were analyzed. To this aim, a particularly interesting region was the one highlighted with the orange rectangle in Fig. 5.3a. The ESA from C at $\omega_1 = 14730$ $cm^{-1}$ shows its maximum intensity at $\omega_3 \sim 14400$ $cm^{-1}$ and a broad tail that spans lower $\omega_3$ values, until 13600 $cm^{-1}$. The broadening of the ESA signal along the emission frequency axis arises from the fact that the ESA can culminate in a series of states at different energies and the starting

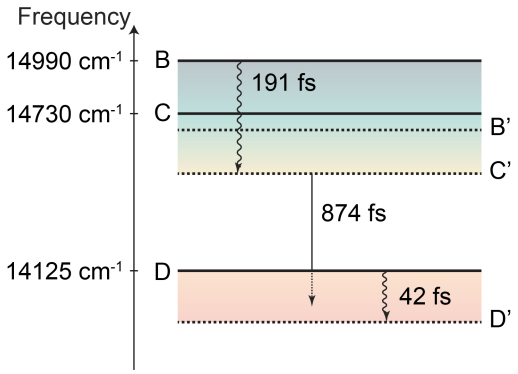


**Figure 5.4:** Pictorial representation of the sequence of processes that, in rCLH, brings the excitation in the manifold of D after photoexcitation of Chls of pools B and C.

pool C is itself a manifold of states. However, as already anticipated, this low energy tail seemed to be partially canceled in an area centered at coordinates (14730,13990) $cm^{-1}$, corresponding to the excitation of pool C and emission from pool D. In correspondence of this cross peak, hereafter indicated as $CP_{CD}$, the spectral signature of the ET from C to D is expected to appear. Therefore, the partial cancellation of the negative ESA signal in that region was attributed to the superposition of a positive signal arising from the ET process. This signal is supposed to rise in time as the ET proceeds, causing a progressive cancellation of the negative ESA as $t_2$ increases. Such a behavior is clearly seen in the temporal trace extracted at $CP_{CD}$ and reported in Fig. 5.3g. It could be argued that a progressive cancellation of the ESA in that point would be expected anyway, because of the relaxation within pool C, from which the ESA signal originates. However, by inspecting the evolution of the maps in Fig. 5.1d, it is clear that the portion of the ESA centered at $CP_{CD}$ has a different dynamics from the rest of the ESA band, as only in that point the ESA has almost completely disappeared after 1 ps. Moreover, the comparison with the 2DES signal of the CLH sample confirms that the cancellation of the ESA in that point is an exclusive feature of the antenna containing the far-red absorbing pool D. Therefore, the decay of the ESA cannot be the only active process and the rise of the ET signal from C to D is very likely to contribute in that region of the map. An exponential fitting of the temporal trace extracted at $CP_{CD}$ and reported in Fig. 5.3g revealed a time constant of 874±195 fs. This should approximately reflect the rate of the ET, even though an accurate determination is hindered by the concomitant decay of the ESA in the same point, as also manifested in the significant error affecting this time constant.

Based on the fitting performed above, it was not possible to determine whether

the ET occurs after relaxation within the manifold of C. To clarify this aspect, a global fitting of the region of the map enclosed in the orange rectangle in Fig. 5.3a was performed using three exponential components: (i) the 191 fs time component, to account for the decay of the ESA caused by the relaxation within manifold C; (ii) the 874 fs time constant, determined as detailed in the previous paragraph; (iii) a » 1 ps decay to account for processes occurring outside the investigated temporal window. The aim of this procedure was not to determine the time constants, but rather to identify the states involved in the ET by looking at the amplitude distribution of component (ii). The DAS of the 874 fs component, shown in Fig. 5.3d, shows a decay of population at $\omega_3$ values corresponding to the bottom of the C manifold (C') and a rise at position $CP_{CD}$. Overall, this plot seems to represent the ET from C' to D or D'. The negative peak in Fig. 5.3d is slightly distorted towards $\omega_3 < 14125$ cm$^{-1}$, which would suggest a direct transfer to D'. However, it should be noticed that the 42 fs time constant was not included in this fitting procedure, because in this region of the map the relaxation within pool D would be masked by other rate-determining processes. Since the downhill energy relaxation within manifold D is much faster than the ET, it is difficult to evaluate if the energy migrates to D and then to D', or directly to D'.

Fig. 5.4 summarizes the sequence of events that, in the rCLH antenna, transports the excitation from B and C to the manifold of D, according to the analyses made so far. The population initially created in Chl pools B and C descends within the two exciton manifolds while relaxing from the higher one to the lower one. Overall, the excitation reaches the energetic bottom of pool C in 191 fs. From there, the excitation is transferred to the manifold D with a time constant of 874 fs. In turn, the excitation created in D by the laser pulse or arrived in D from higher levels relaxes rapidly (42 fs) towards lower exciton states.

Finally, we looked for possible couplings between pools B and D in rCLH. An ultrafast exponential component, which seemed to be active in the first tens of fs after photoexcitation, could be detected at coordinates corresponding to the coupling between Chl pools B and D, both at the upper diagonal position (14125,14940) cm$^{-1}$ (cross peak $CP_{DB}$) and lower diagonal position (14940,13990) cm$^{-1}$ (cross peak $CP_{BD}$). Positions $CP_{DB}$ and $CP_{BD}$ are indicated in Fig. 5.5a, while the temporal traces extracted at these coordinates are shown in Fig. 5.5b. At the $CP_{BD}$ position, the ultrafast feature appeared as a rise (and therefore a cancellation of a negative signal), while at the

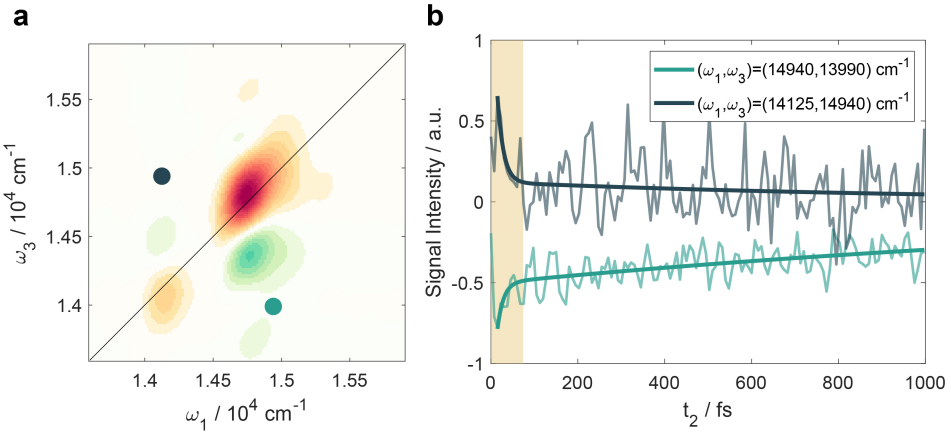


**Figure 5.5:** (a) 77 K 2DES map of rCLH, mediated along $t_2$. (b) Temporal traces of the signals, each mediated on a square of edge 100 cm$^{-1}$ and centered at coordinates indicated by the circles in panel (a). They were tentatively fitted with a two-exponential model, which revealed an ultrafast (∼15 fs) component, besides a long-time decay. The shaded area highlights the temporal interval in which the ultrafast component seems to be active.

$CP_{DB}$ position it appeared as a decay. The presence of a rise below diagonal may be interpreted as an energy transfer from pool B to D, but the very fast time scale of the process and the presence of a decaying feature in the symmetric position above diagonal rule out such an interpretation. Alternatively, this ultrafast feature may result from the localization of an electronic coherence between pools B and D created by the laser pulse. Such a coherence would oscillate with a frequency of ∼860 cm$^{-1}$ (period of ∼40 fs); however, dephasing processes are expected to dampen the oscillation already in the first tens of fs, making the coherent beating appear as an overdamped oscillation. The attribution of the observed ultrafast feature to an overdamped coherent beating would be premature, as the analysis of phenomena occurring on time scales comparable with the time resolution of the experiment hardly allows a precise characterization. Therefore, while awaiting for future more targeted investigations, these observations provide a mere suspicion of a close connection between Chl pools B and D.

## 5.2 Final Remarks

New insight on the red and far-red Chl states of the CLH antenna and the oligomeric rCLH complex from *C. Velia* was gained through the analysis of 2DES data at 77 K. Both the Chl pools contributing to the absorption band at 677 nm (in this thesis indicated with letters A-C) and the far-red absorbing pool (D) exclusive of rCLH showed signatures which are characteristic of excitonic manifolds. The downhill energy relax-

ation within the higher energy manifolds B and C occurs indistinguishably in the two samples, suggesting that these states might be associated with inner Chl pools, poorly affected by the oligomerization. The same process in the D manifold of rCLH occurs much more rapidly, which is compatible with the localization of the far-red absorbing Chl in an outer region of the complex, as suggested by circular dichroism data. The likelihood of a relation between pools B and D remains less clear. Both the second derivative absorption spectrum and the 2DES data hint the presence of an additional pool of states (pool A) which seems to be lost in the oligomer rCLH. Pool D might result from a partial reorganization of pool A as a consequence of the oligomerization. Overall, in the absence of a crystallographic structure, 2DES has revealed to be extremely useful to provide the first indications on the structural arrangement of the chromophores involved in the light harvesting.

# Chapter 6

# Functional and Bio-Mimetic Systems

## 6.1 Self-Assembling Functionalized Porphyrins

The examples discussed in the previous chapters show that biological machines for light energy transport are based on supramolecular architectures of chromophores that combine strong light absorption with the possibility of funneling the absorbed energy through accurately designed routes. Chls are among the most abundant pigments in these systems. Therefore, it is not surprising that bio-mimetic systems that utilize light energy are often based on molecules with an analogous yet simplified chemical structure, i.e., functionalized porphyrins. [124, 125, 126, 127]. In this section, we present the time-dependent spectroscopic characterization of a bio-mimetic system, based on a porphyrin ring functionalized with an oligophenylenethylene (OPE) chain, ending with a $\beta$-D-glucoside group; this system, hereafter indicated as PDP, is represented in Fig. 6.1a. On the one hand, the porphyrin moiety absorbs light on a wide spectral range of the visible and has an intrinsic predisposition to form aggregates in polar solvents. On the other hand, the introduction of a hydrophilic sugar residue linked through the OPE moiety makes the system amphiphilic, helping the formation of ordered structures. Indeed, in a mixture 40/60 water/methanol, nanometer-sized porphyrin aggregates are formed, with the hydrophobic porphyrins in the core of the structure and sugar residues exposed towards water [18]. These self-assembled biocompatible aggregates may be used for several light-activated applications ranging from photodynamic therapy to

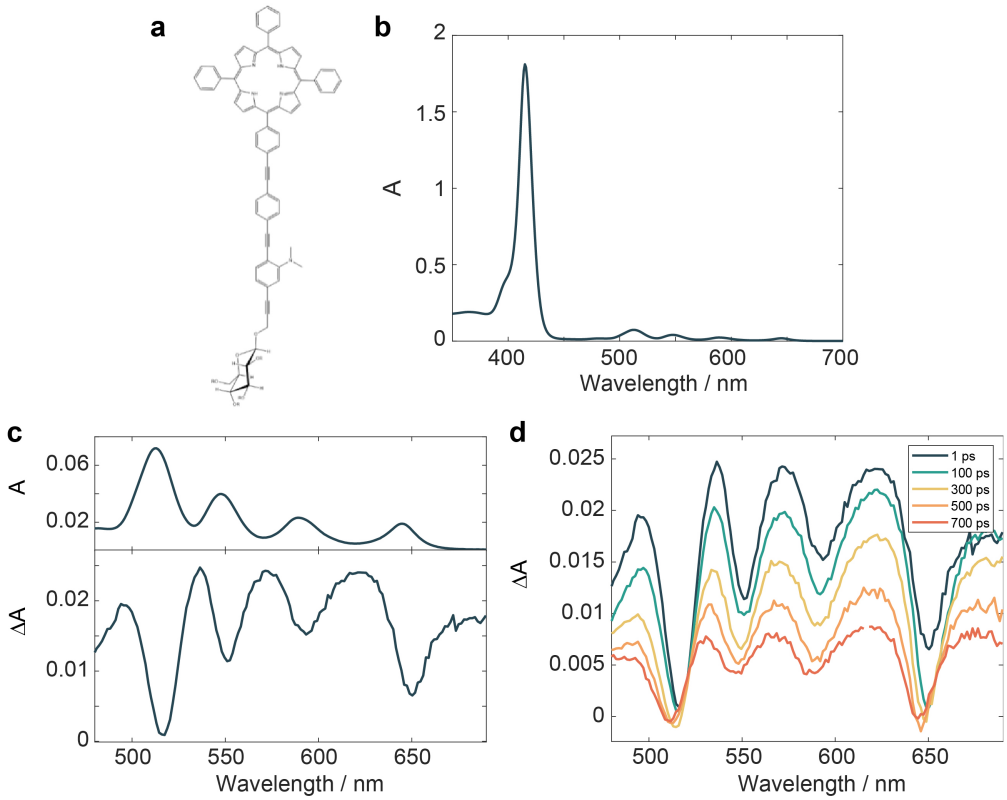


**Figure 6.1:** (a) Structure and (b) absorption spectrum of PDP in methanol. (c) Magnification of the absorption spectrum of PDP in methanol, in the 480-690 nm spectral region, and TA spectrum 1 ps after excitation at 400 nm, in the same spectral region. (c) TA spectra of PDP in methanol, registered at different time delays after excitation.

bioimaging. The spacer between the sugar and the porphyrin has a double function: not only does it help the formation of the supramolecular structures, but also it is itself a chromophore that may bear, in its spectroscopic response, the signatures of possible couplings between the electronic states of the OPE and the porphyrin moieties. Preliminary characterizations of PDP both in its monomeric and aggregated forms were already addressed in the work by Gangemi *et al* [18]. Here we investigate excited state dynamics via TA spectroscopy in the first 800 ps after excitation at 400 nm.

### 6.1.1 Results and Discussion

The UV-Vis absorption spectrum of monomeric PDP (mPDP) in methanol is reported in Fig. 6.1b: it shows the absorption fingerprints typical of the porphyrin moiety, with the B band peaking at 420 nm and Q bands appearing between 500 and 700 nm. The contribution of the OPE is in the form of an increased absorbance at wavelengths $\leq$ 400 nm [18].

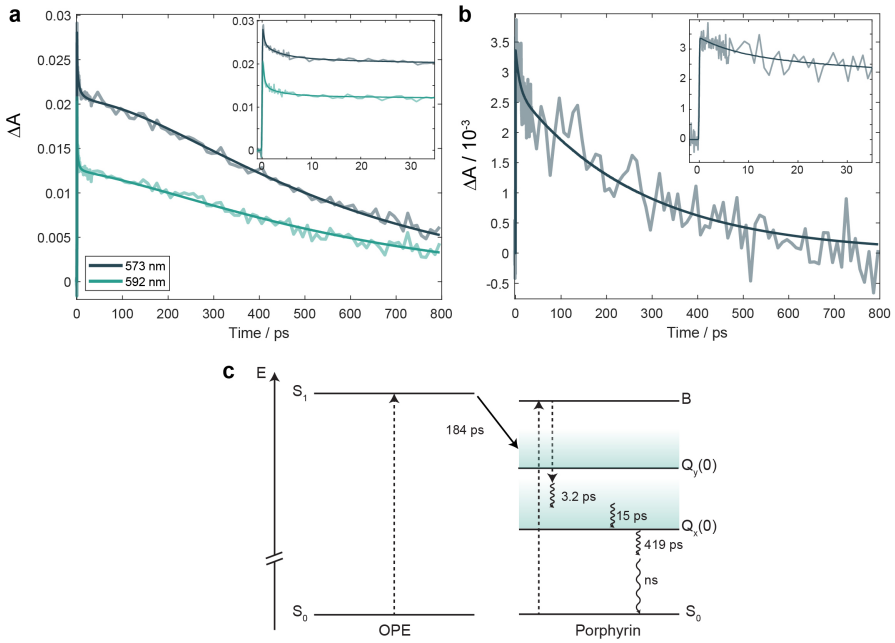


**Figure 6.2:** (a) Time evolution of the TA signal of monomeric PDP in methanol at 573 and 592 nm. The inset shows a zoom on the first 35 ps. (b) Time trace of TPP in methanol/chloroform 50/50 extracted at 539 nm. (c) Schematic representation of the photophysics of the system that summarizes the interpretation of the data. Dashed arrows represent phenomena occurring on a time scale comparable with the time resolution of the experiment; the solid arrow represents the energy transfer; wavy arrows represent relaxation processes.

Fig. 6.1c compares the absorption spectrum of mPDP in the 480-690 nm region with its TA spectrum, in the same spectral region, registered at time delay $T = 1$ ps after photoexcitation. The absorption spectrum in that region exhibits four peaks, attributed to the transitions $Q_x(0)$ (645 nm), its vibrational sideband $Q_x(1)$ (589 nm), $Q_y(0)$ (548 nm) and $Q_y(1)$ (513 nm) of the porphyrin moiety, in agreement with literature [128]. In the same region, the TA spectrum is dominated by a broad positive background, attributed to ESA signals from the Q states. This positive band presents a series of local minima due to the superposition of negative GSB contributions of the Q states, approximately at the same wavelengths at which the Q transitions appear in the absorption spectrum. The local minimum at 650 nm results deeper and slightly red-shifted with respect to what could be expected from the comparison with the absorption spectrum, possibly because of a SE contribution from $Q_x(0)$, as fluorescence emission from that state peaks at 654 nm [18].

The temporal dynamics can be visualized by comparing the TA spectra at different values of the time delay, as in Fig. 6.1d, or by plotting the differential absorption signal $\Delta$A extracted at a specific $\lambda$ against $T$. The time traces extracted at the three local maxima at 536, 573 and 621 nm were fitted with a global multiexponential model, using

a set of shared time constants. As an example, the time trace extracted at 573 nm is shown in Fig. 6.2a, but similar trends are observed also at 536 and 621 nm. The early time (< 100 ps) dynamics is characterized by rapidly decaying components of 0.3, 3.2 and 15 ps. The 0.3 ps time constant can be assigned to the ensemble of phenomena occurring on a time scale comparable to the time resolution of the experiment. Since the internal conversions from the Soret and the $Q_y$ bands of the porphyrin to the $Q_x$ band are expected to occur within this time window [128, 129], the 0.3 ps time constant should include all the processes through which the excitation created by the laser on the porphyrin moiety relaxes to the lowest energy $Q_x$ band. The 3.2 and 15 ps time constants are compatible with vibrational relaxations within the $Q_x$ band, as similar time constants were detected in free-base and substituted tetraphenylporphyrin (TPP) molecules [128, 130, 131]. Overall, these processes bring population to the lowest vibrational level of the $Q_x$ state within tens of ps after photoexcitation in the Soret band.

At longer times, the temporal dynamics is the result of the interplay between two components of opposite signs: a 184 ps rise and a 419 ps decay. Since the lifetime of the $Q_x(0)$ state of the porphyrin is expected to be in the range of several ns [132], the 419 ps decay component may be attributed to a relaxation of the $Q_x(0)$ state preceding the ns emission. Indeed, a relaxation trend with a time constant of the same order of magnitude (272 ps) is also seen in the time evolution of the TA signal of isolated TPP (Fig. 6.2b), used as a reference. This dynamics is too slow to be attributed to solvent relaxation, which is expected to occur within tens of ps [133, 134]. Instead, the time scale of this relaxation could be compatible with conformational changes in the excited-state geometry, which were observed in diacid porphyrins [30]. Alternatively, a decay of the signal in this time scale could be caused by rotational diffusion [135]. While the TA measurements discussed in this section were performed by minimizing the angle between the polarization vectors of the pump and probe beams to maximize the signal, future additional TA measurements on mPDP may be performed by setting an angle of ∼55° ("magic" angle [30]): in this condition, rotational diffusion effects would be limited, which could help to clarify the origin of the 419 ps decay.

The 184 ps rise time was not detected in the time evolution of TPP (Fig. 6.2b). Since in PDP excitation at 400 nm is expected to populate also the $S_1$ state of the OPE moiety, the rise time detected in mPDP may be assigned to an ET process from

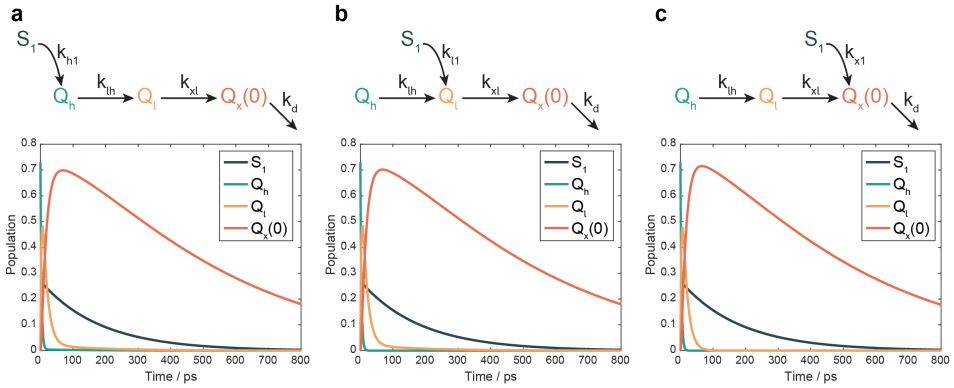


**Figure 6.3:** Comparison between the possible kinetic models that can be used to interpret the time evolution of the TA response. These models differ for the state of the porphyrin which accepts the energy from the OPE moiety. Together with each model, the corresponding time evolution of the kinetic species is shown.

the OPE to the porphyrin moiety. The overall interpretation that results from the multiexponential analysis is schematically summarized in Fig. 6.2c. It should be noticed that a long-time decaying component exceeding the investigated time window, reflecting the emission in the ns, was expected to be present in the signals. However, also given the relatively low fluorescence quantum yield of mPDP (0.033 in $CHCl_3$ [132]), this long-time decay is hidden by the multiple dynamic components that dominate the signals in the investigated time window.

To obtain an estimate of the percentage of population arriving in $Q_x(0)$ after ET from the OPE, with respect to that coming from direct excitation of the B band of the porphyrin, a kinetic model was designed. In this kinetic model, represented in a simplified way in Fig. 6.3a, the time constants retrieved through the previously described parallel multi-exponential fitting were introduced as known parameters. $k_{h1}^{-1} = 184$ ps is the rate of the ET from the $S_1$ state of the OPE to a high-energy state within the Q bands of the porphyrin (indicated as $Q_h$ for generality). Since the excitation in the Q bands of the porphyrin relaxes into the $Q_x$ band within the time resolution of the experiment, it is not possible to know whether $Q_h$ is part of the $Q_y$ band or if it is a vibrationally excited state of the $Q_x$ band. Whatever the identity of $Q_h$, the energy is expected to descend into the $Q_x$ band via relaxation steps that outspeed our time resolution and that, therefore, are not considered in the kinetic model. From $Q_h$, the system undergoes vibrational relaxation to lower energy states in the manifold of $Q_x$ (indicated as $Q_l$) and eventually to $Q_x(0)$ with rate constants $k_{lh}^{-1} = 3.2$ ps and $k_{xl}^{-1} =$

15 ps, respectively. The signal of $Q_x(0)$ decays with rate $k_d^{-1} = 419$ ps. As shown in Fig. 6.3a, the temporal behavior of the kinetic species that corresponds to $Q_x(0)$ matches the long-time trend of the signal registered at 573 nm. The early rise of $Q_x(0)$, resulting from the rapid relaxation of the excitation deposited directly on the porphyrin by the pump pulse, is not directly seen in the time traces at 536, 573 and 621 nm, as it is hidden by the rapidly-decaying ESAs from higher-energy Q bands. The kinetic model allows to estimate in a semi-quantitative way that ∼70% of the population that arrives into the $Q_x(0)$ state comes from the direct excitation of the porphyrin moiety, while the remaining ∼30% is transferred from the OPE. While the use of the time constants obtained by parallel fittings in the kinetic model limits the accuracy of this estimate, this analysis suggests that a non-negligible part of the excitation energy reaching the lowest porphyrin states is initially collected by the OPE.

In developing the kinetic model in Fig. 6.3a, we assumed that the acceptor of the energy from the OPE was a high-energy state within the Q bands, simply based on spectral overlap considerations. However, it could be argued that the choice of the acceptor state was somewhat arbitrary and could affect the results provided by the model. It can be shown, however, that even if the transfer occurred to a lower energy Q state of the porphyrin, the results would remain practically unchanged. Indeed, the comparison with the kinetic models schematically represented in Figs. 6.3b and c, which differ for the choice of the acceptor state, demonstrates that the time behavior of the kinetic species corresponding to $Q_x(0)$ is not significantly affected by the choice of the state to which the OPE transfers the excitation, as the relaxation processes towards $Q_x(0)$ are much faster than the ET.

TA measurements on aggregated PDP (aPDP), prepared using a 60/40 methanol/water mixture, were performed with the same experimental conditions and compared to mPDP. As demonstrated in Fig. 6.4a, the TA spectrum of aPDP shows the same peak pattern as mPDP; only a slight red-shift of the Q band GSB signals is observed, in agreement with the red-shift of the Q transitions also observed in the absorption spectra of porphyrin aggregates [136]. Instead, substantial differences could be detected in the temporal dynamics of the signals, as evident in Figs. 6.4b-d. In fact, when the local maxima at 538, 577 and 623 nm were fitted with a multiexponential model, three distinct decay components of 0.8, 10 and 116 ps were found. These may reflect the same relaxation processes described for mPDP, even though they appear to occur on a faster

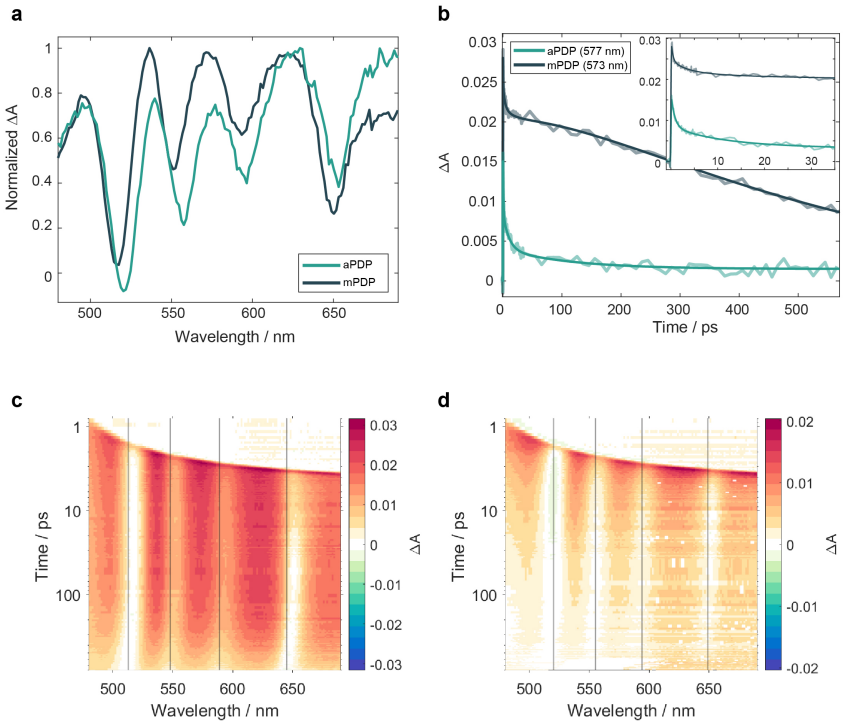


**Figure 6.4:** (a) Normalized TA spectra of monomeric and aggregated PDP 1 ps after photoexcitation at 400 nm. (b) Comparison between the time evolution of the signals of aggregated PDP at 577 nm and monomeric PDP at 573 nm. 2D representation of the data collected by TA experiments on (c) monomeric PDP in methanol and (d) aggregated PDP in methanol/water 60/40, where $\Delta A$ (color scale) is plotted as a function of the probe wavelength (x-axis) and the time delay between pump and probe (y-axis). Solid vertical lines indicate the positions of the Q transitions in the absorption spectra of the two samples: 513, 548, 589 and 645 nm for monomeric PDP and 520, 555, 594 and 649 nm for aggregated PDP.

time scale if compared to the monomer. Moreover, since all the other relevant dynamics were exhausted within the first hundreds of fs, a long-time decaying component (> 800 ps) could be detected in this case, possibly reflecting the emission of the sample in the ns regime. No rise component was found in the dynamics of the aggregated sample. This may imply that the excitation of the OPE follows a different pathway in the aggregated sample and/or that the detection of the spectral signature of the ET is hindered by the overall shortening of the time scales in aPDP.

### 6.1.2 Final Remarks

The TA response of a system composed of a porphyrin ring monosubstituted with a spectroscopically-active group has revealed time-dependent spectroscopic features which could not be detected in the response of the porphyrin moiety alone. This suggests the presence of non-negligible interactions between the two moieties of the system; in particular, the results of the analysis seem to imply an ET from the OPE to the low energy states of the porphyrin. This system could thus effectively mimic the capability of photosynthetic systems to absorb energy in different ranges of the visible spectrum and then funnel it into lower-energy electronic states. While the observations made in the monomeric system provide promising preliminary results, the characterization of the aggregated structures was more elusive because of the shortening of the system's dynamics. To better characterize the faster dynamics of the aggregates, future TA measurements may be conducted by narrowing the investigated time window and focusing the attention in the first 200 ps from the photoexcitation of the aggregates, in which the dynamics of interest are developed.

## 6.2 Dye-sensitized Photoanodes[1]

Dye-sensitized photoelectrochemical cells constitute an appealing tool for exploiting solar light to drive sustainable chemical processes [137, 138]. Yang *et al.* [17] have demonstrated the effectiveness of dye-sensitized photoanodes assembled by vacuum sublimation of quinacridone (QNC) dye onto fluorine-doped tin oxide (FTO), $TiO_2$, and $SnO_2$ slides. QNC is a commercially available, nontoxic chemical with an extended absorption in the visible. Upon absorption of light and excitation into the $S_1$ state,

[1]Section based on [17].

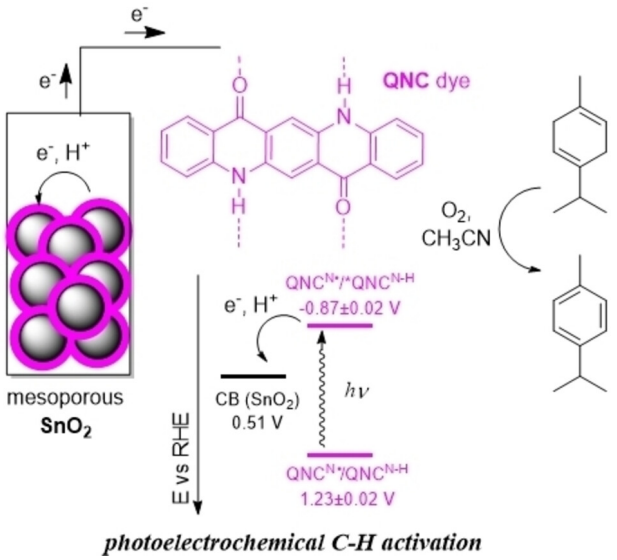


**Figure 6.5:** Photoelectrochemical C-H activation through a QNC-sensitized $SnO_2$ mesoporous semiconductor.

QNC gains reducing properties, with an estimated potential of -0.87±0.02 V for the $QNC^{N\cdot}/{}^*QNC^{N-H}$ couple, suitable for electron injection into the conduction band of most semiconductors [139]. With a proton-coupled electron transfer, the N-H group of QNC is converted into a N centered radical which could be successfully used, for example, to promote oxidative activation of C-H bonds, as schematized in Fig. 6.5.

This section presents the spectroscopic characterization of photoanodes based on thin films of QNC pigments sublimated over FTO slides.

### 6.2.1 Results and Discussion

QNC sensitized electrodes are characterized by absorption peaks at 564, 525 and 485 nm, attributable to $S_0 \rightarrow S_1$ vibronic components of the HOMO→LUMO electronic transition of QNC within an inter-molecular H-bonding network (Fig. 6.6a); the absorption peaks are ca. 40 nm red-shifted with respect to those observed for the QNC dye in dilute solutions [140]. The thickness of the QNC film was estimated to be approximately 40 nm for electrodes with a 0.2 absorbance at 564 nm. The emission of the QNC onto FTO electrodes (FTO|QNC) is characterized by a sharp maximum at 610 nm and by a broad band centered at 690 nm, likely ascribable to differently aggregated forms of QNC [141, 139].

In order to trace photoinduced electron injection, the temporal dynamics of FTO|QNC

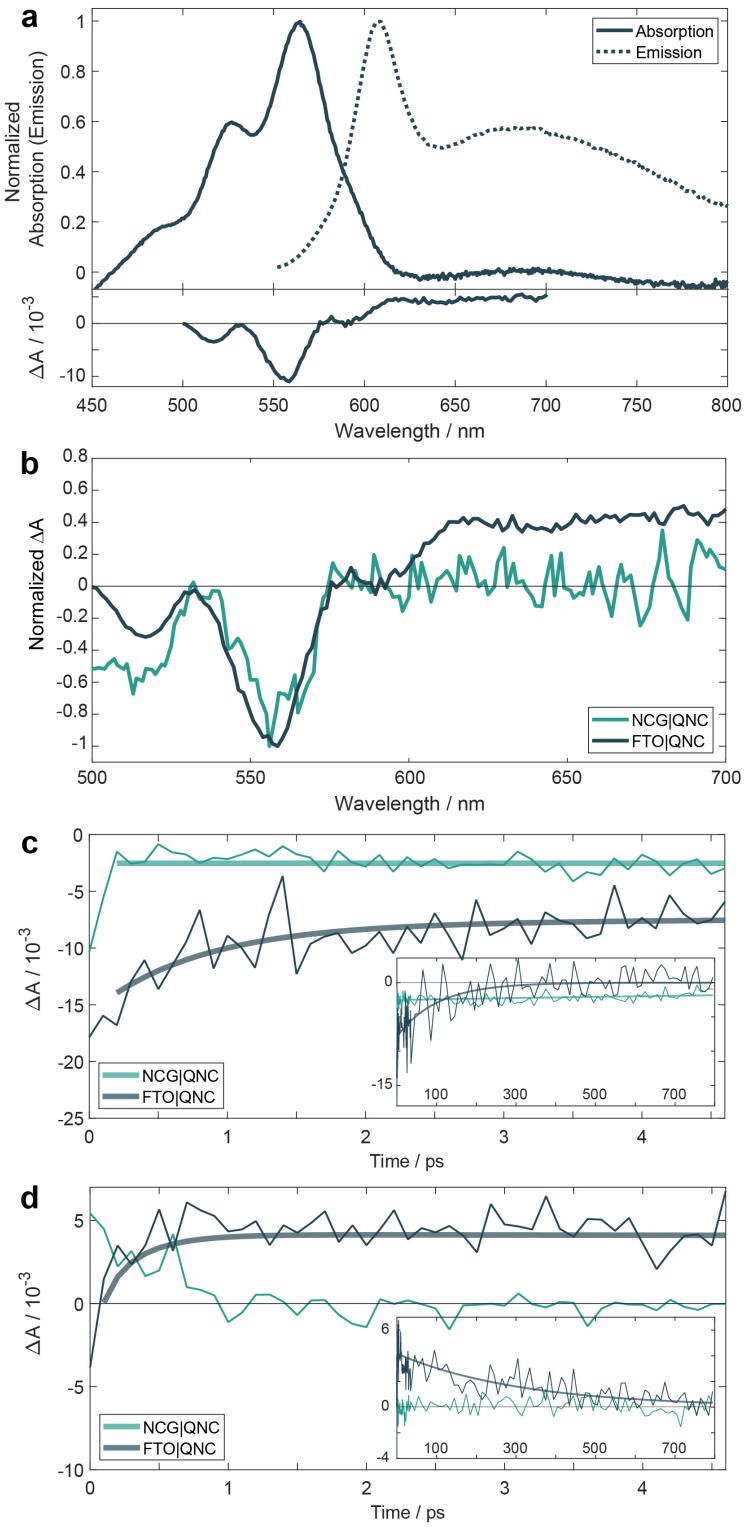


**Figure 6.6:** (a) Upper line: normalized absorption and emission spectra of FTO|QNC. Lower line: TA spectrum of FTO|QNC at a time delay of 3 ps. (b) Comparison between the TA spectra of NCG|QNC and FTO|QNC at a time delay of 3 ps. (c) Time traces, extracted at 559 nm, for NCG|QNC and FTO|QNC. The dynamics at longer times are shown in the inset. (d) Time traces extracted at 664 nm, for NCG|QNC and FTO|QNC. The first 150 fs were neglected in the fitting to avoid pulse overlap effects. The dynamics at longer times are shown in the inset.

electrodes in the first 800 ps after photoexcitation was investigated by means of TA spectroscopy; for comparison, TA measurements on QNC films evaporated on non-conductive glass (hereafter indicated as NCG|QNC) were also performed. Fig. 6.6a shows the TA spectra of FTO|QNC in water at a time delay of 3.0 ps, characterized by a negative GSB at 559 and 518 nm, retracing the absorption spectrum of the dye-sensitized electrode. Similar bleaching features are observed also in TA spectrum of NCG|QNC in Fig. 6.6b. Interestingly, the TA spectrum of FTO|QNC shows also a broad, positive absorption above 600 nm that can be reasonably attributed to the oxidized form of QNC, based on a comparison with a spectroelectrochemistry analysis of FTO|QNC under positive bias [17]. This positive absorption feature is absent in the TA spectrum of NCG|QNC electrodes, where injection is not expected to occur (Fig. 6.6b).

The time evolution of the trace at 559 nm was then analyzed (Fig. 6.6c): while in FTO|QNC its decay is described by two exponential components of 0.8 and 102 ps, in the NCG|QNC reference system, a single exponential decay was obtained with a time constant of around 2.5 ns. Thus, the ultrafast relaxation depleting the excited state in FTO|QNC can be reasonably assigned to the photoinduced electron injection from the QNC excited state into FTO. This attribution was further supported by monitoring the time evolution of the traces at 664 nm in Fig. 6.6d. There, the rise of a positive signal, diagnostic of the formation of the oxidized form of QNC, occurred within the first ps, in good agreement with the time constant of 0.8 ps identified for the recovery of the bleaching at 559 nm, ascribed to the injection process. This signal is then decaying with a time constant of 315 ps, likely attributable to a charge recombination between the oxidized dye and the injected electron. These features are instead absent in the NCG|QNC reference system, where photoinduced electron injection is not occurring.

### 6.2.2 Final Remarks

Overall, this spectroscopic investigation has provided the basis for a better understanding of the photoinduced processes underlying the functioning of dye-sensitized photoanodes. The observation of unique spectral features, not detectable in the non-conductive reference system, has allowed a more direct examination of the phenomena leading to the generation of the photoelectrochemical response. This work lays the foundation for long-term research in which the performances of differently manufactured photoelec-

trodes could be traced back to differences in spectroscopically observable features, like the photoinduced electron injection. In the FTO|QNC anodes, the latter appeared to occur in $< 1$ ps, suggesting that the time resolution offered by TA may be insufficient to fully characterize this process. Upcoming investigations may thus be conducted by exploiting the improved time resolution of 2DES.

# Chapter 7

# Conclusions

In this thesis, ultrafast spectroscopic characterizations of biological antennae and artificial and bio-mimetic systems were presented. On the one hand, the study of photosynthetic systems revealed new details on the strategies that nature has refined, over millions of years of evolution, to maximize the collection of light energy and minimize losses in its transport and exploitation. On the other hand, the characterization of innovative artificial systems for light energy conversion has laid the foundations for a reflection on what are the main factors that determine their performance. The synthesis of these two branches of my research is summarized in the longer-term goal of adopting bio-inspired solutions to overcome the limits of current technologies based on the use of solar energy.

Due to the complexity of the systems examined, it was necessary to take advantage of spectroscopic techniques capable of gathering large amounts of information, while presenting it in the form of signals accessible to analysis. TA spectroscopy and 2DES fulfill this requirement and have in fact proved to be useful investigation tools. In particular, through the recording of time-resolved signals with remarkable time resolution, these techniques offered the possibility to track excited-state dynamics bearing the signatures of ET processes intimately connected with the function of the systems under study. The analysis of the collected data was based on the complementarity of two approaches: on the one hand, by examining time-resolved signals appearing at specific frequencies of the excited-state spectra, it was possible to characterize processes of interest, isolating them from the other contributions that crowded the spectroscopic response. On the other hand, global analyses, that took into account how the whole

excited-state spectra evolved over time, made it possible to contextualize individual processes within the framework of an ordered sequence of events following photoexcitation. The time resolution of 2DES has also enabled the characterization of vibrational wavepackets coupled with electronic excitation, revealing further pieces of information about the photophysics of the pigments and the way it is influenced by the environment.

Through 2DES investigations on PCP, an antenna of dinoflagellate algae with the peculiar characteristic of binding more Cars than Chls, it was possible to supplement the pre-existing knowledge on Car-to-Chl ET with new details. In particular, it was observed that, even altering the polarity of the environment surrounding the Car showing the strongest interaction with the Chl, the ET rate was not significantly affected. Our results suggest that such robustness stems, rather than from the performance of a single channel, from the cooperation of mutually compensating channels, that ensure high functionality even when certain pathways are obstructed. Also, the rapid descent of part of the energy absorbed by the $S_2$ state of the Car on the $S_1$ state via conical intersection would make a multitude of channels immediately available for the transport of excitation. Even more interestingly, our analysis highlighted the relevance, in the ET, of a Car state that cannot be assimilated to any of the states typically observed in isolated Cars. This adds to the growing number of shreds of evidence suggesting that protein scaffolds finely tune the electronic structure of Cars, for example, by adjusting the polarity of the binding pocket or imposing particular geometries.

The premises and the objectives of the work on the CLH antenna of *C. velia* and the far-red absorbing rCLH oligomer, expressed by *C. velia* to adapt to red light, were different. In this case, due to the lack of a crystallographic structure, significant efforts were devoted to assigning the far-red spectral feature of the acclimated rCLH complex. In fact, chromatic adaptation is a particularly interesting feature from the perspective of designing systems that can also operate under variable light conditions. While a series of spectroscopically distinguishable pools of Chl states could be recognized already in the absorption spectra, 2DES characterizations, the first ever carried out on these systems, enabled the study of their excited dynamics and helped map the network of interactions between them. The obtained results have made it possible to refine existing hypotheses and generate new suppositions about the nature of these states and the context in which the Chls are embedded within the protein. Our findings suggest that the far-red states in rCLH may arise from a partial reorganization of pre-existing Chl pools, driven

by the establishment of new inter-subunit interactions within the acclimated oligomer.

Overall, these works showed that the efficiency and versatility of biological machines for harnessing solar energy derive from the exploitation of a limited number of differently and skillfully deployed building blocks, instead of a large variety of components. Rather than being the properties of single chromophores, it is the interplay between them and between them and their surroundings that determines the overall performance. In biological systems, the protein scaffold prepares the most suitable environment and drives the interactions between the pigments. This can hardly be replicated in artificial or bio-mimetic systems. However, one can fine tune the environment in which such systems are embedded by exploiting other parameters, such as solvent polarity, pH and ionic strength, that can be changed within more limited ranges in biological samples. This possibility was explored by studying porphyrins substituted with groups of chromophores capable of enhancing their absorption in the near-UV. TA data seem to show that the excitation collected by the substituent groups can be transferred to the states of the porphyrin rings. These findings become particularly intriguing when considering the capacity of these systems to self-assemble into nano-aggregates in response to a change in solvent polarity. Tracking possible ETs in such aggregates is as challenging as it is exciting, especially considering the chance that the ET already observed in the monomers could be maintained or even amplified in the aggregates, coming to mimic the vectorial flux of energy that occurs in photosynthetic systems. While in the above-mentioned bio-mimetic samples the feasibility of harnessing light energy is still being investigated, dye-sensitized photoanodes have already proven their ability to initiate sustainable C-H bond activation after absorption of visible light. TA spectroscopy has in this case provided a mechanistic insight into the generation of the photoelectrochemical response, also suggesting that the rapid electron transfer from the excited dye to the electrode could be profitably studied via 2DES. It would be thrilling to envision ways to optimize the working conditions by analyzing possible changes in the electron injection dynamics in response to environmental changes, such as the pH of the solution. Our hope is that these results, combined with the insights gained through observation of natural systems, could provide ever new inputs to the research of sustainable technologies that harness light to meet humanity's growing energy demand.

# Bibliography


[1] Ehsanul Kabir, Pawan Kumar, Sandeep Kumar, Adedeji A Adelodun, and Ki-Hyun Kim. Solar energy: Potential and future prospects. *Renewable and Sustainable Energy Reviews*, 82:894–900, 2018.

[2] BP. *Statistical Review of World Energy.* 2023.

[3] International Renewable Energy Agency (IRENA). *Future of Solar Photovoltaics.* 2019.

[4] Nicolò Lago. Advances in photovoltaic materials and devices, 2023.

[5] Modupeola Dada and Patricia Popoola. Recent advances in solar photovoltaic materials and systems for energy storage applications: a review. *Beni-Suef University Journal of Basic and Applied Sciences*, 12(1):1–15, 2023.

[6] Elisabetta Collini. Carotenoids in photosynthesis: the revenge of the "accessory" pigments. *Chem*, 5(3):494–495, 2019.

[7] Gregory D Scholes, Graham R Fleming, Alexandra Olaya-Castro, and Rienk Van Grondelle. Lessons from nature about solar light harvesting. *Nature chemistry*, 3(10):763–774, 2011.

[8] G Steinmeyer, DH Sutter, L Gallmann, N Matuschek, and U Keller. Frontiers in ultrashort pulse generation: pushing the limits in linear and nonlinear optics. *Science*, 286(5444):1507–1512, 1999.

[9] Pierre Agostini and Louis F DiMauro. The physics of attosecond light pulses. *Reports on progress in physics*, 67(6):813, 2004.

[10] Elisabetta Collini. 2D electronic spectroscopic techniques for quantum technology applications. *The Journal of Physical Chemistry C*, 125(24):13096–13108, 2021.

[11] Agata M Brańczyk, Daniel B Turner, and Gregory D Scholes. Crossing disciplines-a view on two-dimensional optical spectroscopy. *Annalen der Physik*, 526(1-2):31–49, 2014.

[12] Elisa Fresch, Franco VA Camargo, Qijie Shen, Caitlin C Bellora, Tõnu Pullerits, Gregory S Engel, Giulio Cerullo, and Elisabetta Collini. Two-dimensional electronic spectroscopy. *Nature Reviews Methods Primers*, 3(1):84, 2023.

[13] Donatella Carbonera, Marilena Di Valentin, Riccardo Spezia, and Alberto Mezzetti. The unique photophysical properties of the peridinin-chlorophyll-a-protein. *Current Protein and Peptide Science*, 15(4):332–350, 2014.

[14] Francesco Tumbarello, Giampaolo Marcolin, Elisa Fresch, Eckhard Hofmann, Donatella Carbonera, and Elisabetta Collini. The energy transfer yield between carotenoids and chlorophylls in peridinin chlorophyll a protein is robust against mutations. *International Journal of Molecular Sciences*, 23(9):5067, 2022.

[15] Eva Kotabová, Jana Jarešová, Radek Kaňa, Roman Sobotka, David Bína, and Ondřej Prášil. Novel type of red-shifted chlorophyll a antenna complex from chromera velia. I. physiological relevance and functional connection to photosystems. *Biochimica et Biophysica Acta (BBA)-Bioenergetics*, 1837(6):734–743, 2014.

[16] David Bína, Zdenko Gardian, Miroslava Herbstová, Eva Kotabová, Peter Koník, Radek Litvín, Ondřej Prášil, Josef Tichỳ, and František Vácha. Novel type of red-shifted chlorophyll a antenna complex from chromera velia: II. biochemistry and spectroscopy. *Biochimica et Biophysica Acta (BBA)-Bioenergetics*, 1837(6):802–810, 2014.

[17] Yunshuo Yang, Giulia Alice Volpato, Elena Rossin, Nicola Peruffo, Francesco Tumbarello, Catia Nicoletti, Ruggero Bonetto, Lorenzo Paoloni, Paolo Umari, Elena Colusso, Luca Dell'Amico, Serena Berardi, Elisabetta Collini, Stefano Caramori, Stefano Agnoli, and Andrea Sartorel. Photoelectrochemical C-H activation through a quinacridone dye enabling proton-coupled electron transfer. *ChemSusChem*, 16(5):e202201980, 2023.

[18] Chiara MA Gangemi, Maria A Castriciano, Ester D'Agostino, Andrea Romeo, Paola M Bonaccorsi, Anna Barattucci, and Luigi Monsù Scolaro. Rod-like

nanostructures through amphiphilic ope-porphyrin self-organization. *Organic & Biomolecular Chemistry*, 21(40):8079–8083, 2023.

[19] Shaul Mukamel. *Principles of nonlinear optical spectroscopy*. Oxford university press New York, 1995.

[20] Robert W Boyd. *Nonlinear optics*. Academic press, 2020.

[21] Jeanne L McHale. *Molecular spectroscopy*. CRC Press, 2017.

[22] Peter Hamm and Martin Zanni. *Concepts and methods of 2D infrared spectroscopy*. Cambridge University Press, 2011.

[23] William W Parson. *Modern optical spectroscopy*, volume 2. Springer, 2007.

[24] Minhaeng Cho. *Two-dimensional optical spectroscopy*. CRC press, 2009.

[25] Vytautas Butkus, Darius Abramavicius, Andrius Gelzinis, and Leonas Valkunas. Two-dimensional optical spectroscopy of molecular aggregates. *Lithuanian Journal of Physics*, 50(3), 2010.

[26] Darius Abramavicius, Benoit Palmieri, Dmitri V Voronine, Frantisek Sanda, and Shaul Mukamel. Coherent multidimensional optical spectroscopy of excitons in molecular aggregates; quasiparticle versus supermolecule perspectives. *Chemical reviews*, 109(6):2350–2408, 2009.

[27] M Blume. Stochastic theory of line shape: generalization of the kubo-anderson model. *Physical Review*, 174(2):351, 1968.

[28] Rudi Berera, Rienk van Grondelle, and John TM Kennis. Ultrafast transient absorption spectroscopy: principles and application to photosynthetic systems. *Photosynthesis research*, 101:105–118, 2009.

[29] Tina Jingyan Miao and Junwang Tang. Characterization of charge carrier behavior in photocatalysis using transient absorption spectroscopy. *The Journal of Chemical Physics*, 152(19), 2020.

[30] Elisabetta Collini, Camilla Ferrante, and Renato Bozio. Influence of excitonic interactions on the transient absorption and two-photon absorption spectra of porphyrin J-aggregates in the NIR region. *The Journal of Physical Chemistry C*, 111(50):18636–18645, 2007.

[31] Nicola Peruffo, Fabrizio Mancin, and Elisabetta Collini. Ultrafast dynamics of multiple plexcitons in colloidal nanomaterials: The mediating action of plasmon resonances and dark states. *The Journal of Physical Chemistry Letters*, 13(28):6412–6419, 2022.

[32] Elisa Fresch, Nicola Peruffo, Mariachiara Trapani, Massimiliano Cordaro, Giovanni Bella, Maria Angela Castriciano, and Elisabetta Collini. The effect of hydrogen bonds on the ultrafast relaxation dynamics of a BODIPY dimer. *The Journal of Chemical Physics*, 154(8):084201, 2021.

[33] John D Hybl, Allison W Albrecht, Sarah M Gallagher Faeder, and David M Jonas. Two-dimensional electronic spectroscopy. *Chemical physics letters*, 297(3-4):307–313, 1998.

[34] Franklin D Fuller and Jennifer P Ogilvie. Experimental implementations of two-dimensional Fourier transform electronic spectroscopy. *Annual review of physical chemistry*, 66:667–690, 2015.

[35] Luca Bolzonello, Andrea Volpato, Elena Meneghin, and Elisabetta Collini. Versatile setup for high-quality rephasing, non-rephasing, and double quantum 2D electronic spectroscopy. *JOSA B*, 34(6):1223–1233, 2017.

[36] Frederic Verluise, Vincent Laude, Z Cheng, Ch Spielmann, and Pierre Tournois. Amplitude and phase control of ultrashort pulses by use of an acousto-optic programmable dispersive filter: pulse compression and shaping. *Optics letters*, 25(8):575–577, 2000.

[37] Pierre Tournois. Acousto-optic programmable dispersive filter for adaptive compensation of group delay time dispersion in laser systems. *Optics communications*, 140(4-6):245–249, 1997.

[38] RL Fork, OE Martinez, and JP Gordon. Negative dispersion using pairs of prisms. *Optics letters*, 9(5):150–152, 1984.

[39] Daniel J Kane and Rick Trebino. Characterization of arbitrary femtosecond pulses using frequency-resolved optical gating. *IEEE Journal of Quantum Electronics*, 29(2):571–579, 1993.

[40] Ramunas Augulis and Donatas Zigmantas. Two-dimensional electronic spectroscopy with double modulation lock-in detection: enhancement of sensitivity and noise resistance. *Optics express*, 19(14):13126–13133, 2011.

[41] David M Jonas. Two-dimensional femtosecond spectroscopy. *Annual review of physical chemistry*, 54(1):425–463, 2003.

[42] Ivo HM van Stokkum, Delmar S Larsen, and Rienk Van Grondelle. Global and target analysis of time-resolved spectra. *Biochimica et Biophysica Acta (BBA)-Bioenergetics*, 1657(2-3):82–104, 2004.

[43] Steven T Cundiff. Optical three dimensional coherent spectroscopy. *Physical chemistry chemical physics*, 16(18):8193–8200, 2014.

[44] Javier Prior, Enrique Castro, Alex W Chin, Javier Almeida, Susana F Huelga, and Martin B Plenio. Wavelet analysis of molecular dynamics: efficient extraction of time-frequency information in ultrafast optical processes. *The Journal of Chemical Physics*, 139(22):224103, 2013.

[45] Andrea Volpato, Luca Bolzonello, Elena Meneghin, and Elisabetta Collini. Global analysis of coherence and population dynamics in 2D electronic spectroscopy. *Optics Express*, 24(21):24773–24785, 2016.

[46] Gitt Panitchayangkoon, Dmitri V Voronine, Darius Abramavicius, Justin R Caram, Nicholas HC Lewis, Shaul Mukamel, and Gregory S Engel. Direct evidence of quantum transport in photosynthetic light-harvesting complexes. *Proceedings of the National Academy of Sciences*, 108(52):20908–20912, 2011.

[47] Daniel B Turner, Krystyna E Wilk, Paul MG Curmi, and Gregory D Scholes. Comparison of electronic and vibrational coherence measured by two-dimensional electronic spectroscopy. *The Journal of Physical Chemistry Letters*, 2(15):1904–1911, 2011.

[48] Daniel B Turner, Rayomond Dinshaw, Kyung-Koo Lee, Michael S Belsley, Krystyna E Wilk, Paul MG Curmi, and Gregory D Scholes. Quantitative investigations of quantum coherence for a light-harvesting protein at conditions simulating photosynthesis. *Physical Chemistry Chemical Physics*, 14(14):4857–4874, 2012.

[49] Franco V de A Camargo, Lena Grimmelsmann, Harry L Anderson, Stephen R Meech, and Ismael A Heisler. Resolving vibrational from electronic coherences in two-dimensional electronic spectroscopy: The role of the laser spectrum. *Physical Review Letters*, 118(3):033001, 2017.

[50] Roel Tempelaar, Alexei Halpin, Philip JM Johnson, Jianxin Cai, R Scott Murphy, Jasper Knoester, RJ Dwayne Miller, and Thomas LC Jansen. Laser-limited signatures of quantum coherence. *The Journal of Physical Chemistry A*, 120(19):3042–3048, 2016.

[51] Hideki Hashimoto, Chiasa Uragami, Nao Yukihira, Alastair T Gardiner, and Richard J Cogdell. Understanding/unravelling carotenoid excited singlet states. *Journal of The Royal Society Interface*, 15(141):20180026, 2018.

[52] Tomáš Polívka and Villy Sundström. Ultrafast dynamics of carotenoid excited states- from solution to natural and artificial systems. *Chemical reviews*, 104(4):2021–2072, 2004.

[53] Tomáš Polívka, Jennifer L Herek, Donatas Zigmantas, Hans-Erik Åkerlund, and Villy Sundström. Direct observation of the (forbidden) $S_1$ state in carotenoids. *Proceedings of the National Academy of Sciences*, 96(9):4914–4917, 1999.

[54] Donatas Zigmantas, Tomáš Polívka, Roger G Hiller, Arkady Yartsev, and Villy Sundström. Spectroscopic and dynamic properties of the peridinin lowest singlet excited states. *The Journal of Physical Chemistry A*, 105(45):10296–10306, 2001.

[55] Leszek Fiedor, Joanna Fiedor, and Mariusz Pilch. Effects of molecular symmetry on the electronic transitions in carotenoids. *The Journal of Physical Chemistry Letters*, 7(10):1821–1829, 2016.

[56] Miriam M Enriquez, Shohei Hananoki, Shinji Hasegawa, Takayuki Kajikawa, Shigeo Katsumura, Nicole L Wagner, Robert R Birge, and Harry A Frank. Effect of molecular symmetry on the spectra and dynamics of the intramolecular charge transfer (ICT) state of peridinin. *The Journal of Physical Chemistry B*, 116(35):10748–10756, 2012.

[57] Dariusz M Niedzwiedzki, Nirmalya Chatterjee, Miriam M Enriquez, Takayuki Kajikawa, Shinji Hasegawa, Shigeo Katsumura, and Harry A Frank. Spectroscopic investigation of peridinin analogues having different $\pi$-electron conjugated chain

lengths: exploring the nature of the intramolecular charge transfer state. *The Journal of Physical Chemistry B*, 113(41):13604–13612, 2009.

[58] Toshiyuki Kusumoto, Tomoko Horibe, Takayuki Kajikawa, Shinji Hasegawa, Takashi Iwashita, Richard J Cogdell, Robert R Birge, Harry A Frank, Shigeo Katsumura, and Hideki Hashimoto. Stark absorption spectroscopy of peridinin and allene-modified analogues. *Chemical physics*, 373(1-2):71–79, 2010.

[59] Donatas Zigmantas, Roger G Hiller, Frank P Sharples, Harry A Frank, Villy Sundström, and Tomáš Polívka. Effect of a conjugated carbonyl group on the photophysical properties of carotenoids. *Physical Chemistry Chemical Physics*, 6(11):3009–3016, 2004.

[60] Nicole L Wagner, Jordan A Greco, Miriam M Enriquez, Harry A Frank, and Robert R Birge. The nature of the intramolecular charge transfer state in peridinin. *Biophysical journal*, 104(6):1314–1325, 2013.

[61] Giampaolo Marcolin and Elisabetta Collini. Solvent-dependent characterization of fucoxanthin through 2D electronic spectroscopy reveals new details on the intramolecular charge-transfer state dynamics. *The Journal of Physical Chemistry Letters*, 12(20):4833–4840, 2021.

[62] Kipras Redeckas, Vladislava Voiciuk, and Mikas Vengris. Investigation of the $S_1$/ICT equilibrium in fucoxanthin by ultrafast pump–dump–probe and femtosecond stimulated raman scattering spectroscopy. *Photosynthesis research*, 128:169–181, 2016.

[63] James A Bautista, Robert E Connors, B Bangar Raju, Roger G Hiller, Frank P Sharples, David Gosztola, Michael R Wasielewski, and Harry A Frank. Excited state properties of peridinin: observation of a solvent dependence of the lowest excited singlet state lifetime and spectral behavior unique among carotenoids. *The Journal of Physical Chemistry B*, 103(41):8751–8758, 1999.

[64] Tomáš Polívka and Villy Sundström. Dark excited states of carotenoids: consensus and controversy. *Chemical Physics Letters*, 477(1-3):1–11, 2009.

[65] Robert G West, Marcel Fuciman, Hristina Staleva-Musto, Vaclav Sebelik, David Bina, Milan Durchan, Valentyna Kuznetsova, and Tomas Polivka. Equilibration dependence of fucoxanthin $S_1$ and ICT signatures on polarity, proticity, and

temperature by multipulse femtosecond absorption spectroscopy. *The Journal of Physical Chemistry B*, 122(29):7264–7276, 2018.

[66] Donatas Zigmantas, Roger G Hiller, Villy Sundstrom, and Tomas Polivka. Carotenoid to chlorophyll energy transfer in the peridinin–chlorophyll-a–protein complex involves an intramolecular charge transfer state.

[67] Tomas Polivka, Roger G Hiller, and Harry A Frank. Spectroscopy of the peridinin–chlorophyll-a protein: insight into light-harvesting strategy of marine algae. *Archives of biochemistry and biophysics*, 458(2):111–120, 2007.

[68] Tomas Polivka and Eckhard Hofmann. Structure-function relationship in peridinin-chlorophyll proteins. *The Structural Basis of Biological Energy Generation*, pages 39–58, 2014.

[69] Giulio Cerullo, Dario Polli, Guglielmo Lanzani, Sandro De Silvestri, Hideki Hashimoto, and Richard J Cogdell. Photosynthetic light harvesting by carotenoids: detection of an intermediate excited state. *Science*, 298(5602):2395–2398, 2002.

[70] Claudiu C Gradinaru, John TM Kennis, Emmanouil Papagiannakis, Ivo HM Van Stokkum, Richard J Cogdell, Graham R Fleming, Robert A Niederman, and Rienk Van Grondelle. An unusual pathway of excitation energy deactivation in carotenoids: singlet-to-triplet conversion on an ultrafast timescale in a photosynthetic antenna. *Proceedings of the National Academy of Sciences*, 98(5):2364–2369, 2001.

[71] Dario Polli, G Cerullo, Guglielmo Lanzani, Sandro De Silvestri, K Yanagi, H Hashimoto, and RJ Cogdell. Conjugation length dependence of internal conversion in carotenoids: role of the intermediate state. *Physical review letters*, 93(16):163002, 2004.

[72] Daisuke Kosumi, Kazuhiro Yanagi, Ritsuko Fujii, Hideki Hashimoto, and Masayuki Yoshizawa. Conjugation length dependence of relaxation kinetics in $\beta$-carotene homologs probed by femtosecond kerr-gate fluorescence spectroscopy. *Chemical physics letters*, 425(1-3):66–70, 2006.

[73] Evgeny E Ostroumov, Rachel M Mulvaney, Richard J Cogdell, and Gregory D Scholes. Broadband 2D electronic spectroscopy reveals a carotenoid dark state in purple bacteria. *Science*, 340(6128):52–56, 2013.

[74] Paul Tavan and Klaus Schulten. Electronic excitations in finite and infinite polyenes. *Physical Review B*, 36(8):4337, 1987.

[75] Evgeny Ostroumov, Marc G Müller, Christel M Marian, Martin Kleinschmidt, and Alfred R Holzwarth. Electronic coherence provides a direct proof for energy-level crossing in photoexcited lutein and $\beta$-carotene. *Physical review letters*, 103(10):108302, 2009.

[76] Takeshi Miki, Tiago Buckup, Marie S Krause, June Southall, Richard J Cogdell, and Marcus Motzkus. Vibronic coupling in the excited-states of carotenoids. *Physical Chemistry Chemical Physics*, 18(16):11443–11453, 2016.

[77] Daniil Khokhlov and Aleksandr Belov. Toward an accurate ab initio description of low-lying singlet excited states of polyenes. *Journal of Chemical Theory and Computation*, 17(7):4301–4315, 2021.

[78] Davide Accomasso, Serra Arslancan, Lorenzo Cupellini, Giovanni Granucci, and Benedetta Mennucci. Ultrafast excited-state dynamics of carotenoids and the role of the $S_x$ state. *The Journal of Physical Chemistry Letters*, 13(29):6762–6769, 2022.

[79] Zi SD Toa, Mary H Degolian, Chanelle C Jumper, Roger G Hiller, and Gregory D Scholes. Consistent model of ultrafast energy transfer in peridinin chlorophyll-a protein using two-dimensional electronic spectroscopy and forster theory. *The Journal of Physical Chemistry B*, 123(30):6410–6420, 2019.

[80] Soumen Ghosh, Michael M Bishop, Jerome D Roscioli, Jenny Jo Mueller, Nolan C Shepherd, Amy M LaFountain, Harry A Frank, and Warren F Beck. Femtosecond heterodyne transient-grating studies of nonradiative decay of the $S_2$ ($1^1Bu^+$) state of $\beta$-carotene: contributions from dark intermediates and double-quantum coherences. *The Journal of Physical Chemistry B*, 119(47):14905–14924, 2015.

[81] Soumen Ghosh, Jerome D Roscioli, Michael M Bishop, Jason K Gurchiek, Amy M LaFountain, Harry A Frank, and Warren F Beck. Torsional dynamics and intramolecular charge transfer in the $S_2$ ($1^1Bu^+$) excited state of peridinin: a mechanism for enhanced mid-visible light harvesting. *The journal of physical chemistry letters*, 7(18):3621–3626, 2016.

[82] Soumen Ghosh, Michael M Bishop, Jerome D Roscioli, Amy M LaFountain, Harry A Frank, and Warren F Beck. Excitation energy transfer by coherent

and incoherent mechanisms in the peridinin–chlorophyll a protein. *The Journal of Physical Chemistry Letters*, 8(2):463–469, 2017.

[83] Warren F Beck, Michael M Bishop, Jerome D Roscioli, Soumen Ghosh, and Harry A Frank. Excited state conformational dynamics in carotenoids: dark intermediates and excitation energy transfer. *Archives of biochemistry and biophysics*, 572:175–183, 2015.

[84] Eckhard Hofmann, Pamela M Wrench, Frank P Sharples, Roger G Hiller, Wolfram Welte, and Kay Diederichs. Structural basis of light harvesting by carotenoids: peridinin-chlorophyll-protein from amphidinium carterae. *Science*, 272(5269):1788–1791, 1996.

[85] Robielyn P Ilagan, Sumie Shima, Alexander Melkozernov, Su Lin, Robert E Blankenship, Frank P Sharples, Roger G Hiller, Robert R Birge, and Harry A Frank. Spectroscopic properties of the main-form and high-salt peridinin- chlorophyll a proteins from amphidinium carterae. *Biochemistry*, 43(6):1478–1487, 2004.

[86] Brent P Krueger, Stefania S Lampoura, Ivo HM Van Stokkum, Emmanouil Papagiannakis, Jante M Salverda, Claudiu C Gradinaru, Danielis Rutkauskas, Roger G Hiller, and Rienk Van Grondelle. Energy transfer in the peridinin chlorophyll-a protein of amphidinium carterae studied by polarized transient absorption and target analysis. *Biophysical Journal*, 80(6):2843–2855, 2001.

[87] Jerome D Roscioli, Soumen Ghosh, Amy M LaFountain, Harry A Frank, and Warren F Beck. Quantum coherent excitation energy transfer by carotenoids in photosynthetic light harvesting. *The Journal of Physical Chemistry Letters*, 8(20):5141–5147, 2017.

[88] Jerome D Roscioli, Soumen Ghosh, Amy M LaFountain, Harry A Frank, and Warren F Beck. Structural tuning of quantum decoherence and coherent energy transfer in photosynthetic light harvesting. *The journal of physical chemistry letters*, 9(17):5071–5077, 2018.

[89] Elena Meneghin, Andrea Volpato, Lorenzo Cupellini, Luca Bolzonello, Sandro Jurinovich, Vincenzo Mascoli, Donatella Carbonera, Benedetta Mennucci, and Elisabetta Collini. Coherence in carotenoid-to-chlorophyll energy transfer. *Nature Communications*, 9(1):3160, 2018.

[90] Ryan W Tilluck, Soumen Ghosh, Matthew J Guberman-Pfeffer, Jerome D Roscioli, JK Gurchiek, Amy M LaFountain, Harry A Frank, José A Gascón, and Warren F Beck. Interexciton nonradiative relaxation pathways in the peridinin-chlorophyll protein. *Cell Reports Physical Science*, 2(3):100380, 2021.

[91] Tim Schulte, Dariusz M Niedzwiedzki, Robert R Birge, Roger G Hiller, Tomáš Polívka, Eckhard Hofmann, and Harry A Frank. Identification of a single peridinin sensing Chl-a excitation in reconstituted pcp by crystallography and spectroscopy. *Proceedings of the National Academy of Sciences*, 106(49):20764–20769, 2009.

[92] Tim Schulte, Silke Johanning, and Eckhard Hofmann. Structure and function of native and refolded peridinin-chlorophyll-proteins from dinoflagellates. *European journal of cell biology*, 89(12):990–997, 2010.

[93] Alessandro Agostini, Jens Niklas, Tim Schulte, Marilena Di Valentin, Marco Bortolus, Eckhard Hofmann, Wolfgang Lubitz, and Donatella Carbonera. Changing the site energy of per-614 in the peridinin-chlorophyll a-protein does not alter its capability of chlorophyll triplet quenching. *Biochimica et Biophysica Acta (BBA)-Bioenergetics*, 1859(8):612–618, 2018.

[94] Donatella Carbonera, Giovanni Giacometti, Ulderico Segre, Eckhard Hofmann, and Roger G Hiller. Structure-based calculations of the optical spectra of the light-harvesting peridinin- chlorophyll- protein complexes from amphidinium carterae and heterocapsa pygmaea. *The Journal of Physical Chemistry B*, 103(30):6349–6356, 1999.

[95] Matthew J Guberman-Pfeffer and José A Gascón. Carotenoid-chlorophyll interactions in a photosynthetic antenna protein: A supramolecular QM/MM approach. *Molecules*, 23(10):2589, 2018.

[96] Elena Meneghin, Cristina Leonardo, Andrea Volpato, Luca Bolzonello, and Elisabetta Collini. Mechanistic insight into internal conversion process within Q-bands of chlorophyll a. *Scientific Reports*, 7(1):11389, 2017.

[97] Elena Meneghin, Danilo Pedron, and Elisabetta Collini. Raman and 2D electronic spectroscopies: A fruitful alliance for the investigation of ground and excited state vibrations in chlorophyll a. *Chemical Physics*, 514:132–140, 2018.

[98] Etienne Mangaud, Benjamin Lasorne, Osman Atabek, and Michèle Desouter-Lecomte. Statistical distributions of the tuning and coupling collective modes at a conical intersection using the hierarchical equations of motion. *The Journal of Chemical Physics*, 151(24):244102, 2019.

[99] Christoph Schnedermann, Matz Liebel, and Philipp Kukura. Mode-specificity of vibrationally coherent internal conversion in rhodopsin during the primary visual event. *Journal of the American Chemical Society*, 137(8):2886–2891, 2015.

[100] Matz Liebel, Christoph Schnedermann, and Philipp Kukura. Vibrationally coherent crossing and coupling of electronic states during internal conversion in $\beta$-carotene. *Physical Review Letters*, 112(19):198302, 2014.

[101] Lipeng Chen, Maxim F Gelin, Vladimir Y Chernyak, Wolfgang Domcke, and Yang Zhao. Dissipative dynamics at conical intersections: simulations with the hierarchy equations of motion method. *Faraday discussions*, 194:61–80, 2016.

[102] Elizabeth Kish, Maria Manuela Mendes Pinto, Daniele Bovi, Marie Basire, Leonardo Guidoni, Rodolphe Vuilleumier, Bruno Robert, Riccardo Spezia, and Alberto Mezzetti. Fermi resonance as a tool for probing peridinin environment. *The Journal of Physical Chemistry B*, 118(22):5873–5881, 2014.

[103] Tiago Buckup and Marcus Motzkus. Multidimensional time-resolved spectroscopy of vibrational coherence in biopolyenes. *Annual review of physical chemistry*, 65:39–57, 2014.

[104] JA Davis, E Cannon, L Van Dao, P Hannaford, HM Quiney, and KA Nugent. Long-lived coherence in carotenoids. *New Journal of Physics*, 12(8):085015, 2010.

[105] Minjung Son, Alberta Pinnola, Roberto Bassi, and Gabriela S Schlau-Cohen. The electronic structure of lutein 2 is optimized for light harvesting in plants. *Chem*, 5(3):575–584, 2019.

[106] Vytautas Balevičius, Arpa Galestian Pour, Janne Savolainen, Craig N Lincoln, Vladimír Lukeš, Eberhard Riedle, Leonas Valkunas, Darius Abramavicius, and Jürgen Hauer. Vibronic energy relaxation approach highlighting deactivation pathways in carotenoids. *Physical Chemistry Chemical Physics*, 17(29):19491–19499, 2015.

[107] Nila Mohan TM, Chase H Leslie, Sourav Sil, Justin B Rose, Ryan W Tilluck, and Warren F Beck. Broadband 2DES detection of vibrational coherence in the $S_x$ state of canthaxanthin. *The Journal of Chemical Physics*, 155(3):035103, 2021.

[108] Dario Polli, Piero Altoè, Oliver Weingart, Katelyn M Spillane, Cristian Manzoni, Daniele Brida, Gaia Tomasello, Giorgio Orlandi, Philipp Kukura, Richard A Mathies, et al. Conical intersection dynamics of the primary photoisomerization event in vision. *Nature*, 467(7314):440–443, 2010.

[109] Robielyn P Ilagan, Timothy W Chapp, Roger G Hiller, Frank P Sharples, Tomáš Polívka, and Harry A Frank. Optical spectroscopic studies of light-harvesting by pigment-reconstituted peridinin-chlorophyll-proteins at cryogenic temperatures. *Photosynthesis research*, 90:5–15, 2006.

[110] Manuel J Llansola-Portoles, Chiasa Uragami, Andrew A Pascal, David Bina, Radek Litvin, and Bruno Robert. Pigment structure in the FCP-like light-harvesting complex from chromera velia. *Biochimica et Biophysica Acta (BBA)-Bioenergetics*, 1857(11):1759–1765, 2016.

[111] Wenda Wang, Long-Jiang Yu, Caizhe Xu, Takashi Tomizaki, Songhao Zhao, Yasufumi Umena, Xiaobo Chen, Xiaochun Qin, Yueyong Xin, Michihiro Suga, et al. Structural basis for blue-green light harvesting and energy dissipation in diatoms. *Science*, 363(6427):eaav0365, 2019.

[112] Hideaki Miyashita, Kyoko Adachi, Norihide Kurano, Hisato Ikemot, Mitsuo Chihara, and Shigetoh Miyach. Pigment composition of a novel oxygenic photosynthetic prokaryote containing chlorophyll d as the major chlorophyll. *Plant and cell physiology*, 38(3):274–281, 1997.

[113] Radek Litvín, David Bína, Miroslava Herbstová, Marek Pazderník, Eva Kotabová, Zdenko Gardian, Martin Trtílek, Ondřej Prášil, and František Vácha. Red-shifted light-harvesting system of freshwater eukaryotic alga trachydiscus minutus (eustigmatophyta, stramenopila). *Photosynthesis research*, 142:137–151, 2019.

[114] Tomas Morosinotto, Jacques Breton, Roberto Bassi, and Roberta Croce. The nature of a chlorophyll ligand in lhca proteins determines the far red fluorescence emission typical of photosystem i. *Journal of Biological Chemistry*, 278(49):49223–49229, 2003.

[115] Elisabet Romero, Milena Mozzo, Ivo HM Van Stokkum, Jan P Dekker, Rienk Van Grondelle, and Roberta Croce. The origin of the low-energy form of photosystem i light-harvesting complex lhca4: mixing of the lowest exciton with a charge-transfer state. *Biophysical journal*, 96(5):L35–L37, 2009.

[116] Roberta Croce and Herbert Van Amerongen. Light-harvesting in photosystem i. *Photosynthesis Research*, 116:153–166, 2013.

[117] Md Wahadoszamen, Tjaart PJ Krüger, Anjue Mane Ara, Rienk Van Grondelle, and Michal Gwizdala. Charge transfer states in phycobilisomes. *Biochimica et Biophysica Acta (BBA)-Bioenergetics*, 1861(7):148187, 2020.

[118] M Faisal Khyasudeen, Paweł J Nowakowski, Hoang Long Nguyen, Jamie HN Sim, Thanh Nhut Do, and Howe-Siang Tan. Studying the spectral diffusion dynamics of chlorophyll a and chlorophyll b using two-dimensional electronic spectroscopy. *Chemical Physics*, 527:110480, 2019.

[119] Sunhong Jun, Cheolhee Yang, Tae Wu Kim, Megumi Isaji, Hitoshi Tamiaki, Hyotcherl Ihee, and Jeongho Kim. Role of thermal excitation in ultrafast energy transfer in chlorosomes revealed by two-dimensional electronic spectroscopy. *Physical Chemistry Chemical Physics*, 17(27):17872–17879, 2015.

[120] David Bína, Milan Durchan, Valentyna Kuznetsova, František Vácha, Radek Litvín, and Tomáš Polívka. Energy transfer dynamics in a red-shifted violaxanthin-chlorophyll a light-harvesting complex. *Biochimica et Biophysica Acta (BBA)-Bioenergetics*, 1860(2):111–120, 2019.

[121] Kaoru Minoshima, Makoto Taiji, Kazuhiko Misawa, and Takayoshi Kobayashi. Femtosecond nonlinear optical dynamics of excitons in J-aggregates. *Chemical physics letters*, 218(1-2):67–72, 1994.

[122] Naomi S Ginsberg, Yuan-Chung Cheng, and Graham R Fleming. Two-dimensional electronic spectroscopy of molecular aggregates. *Accounts of chemical research*, 42(9):1352–1363, 2009.

[123] Eva Rivera, Daniel Montemayor, Marco Masia, and David F Coker. Influence of site-dependent pigment–protein interactions on excitation energy transfer in photosynthetic light harvesting. *The Journal of Physical Chemistry B*, 117(18):5510–5521, 2013.

[124] Jong Min Park, Kyeong-Im Hong, Hosoowi Lee, and Woo-Dong Jang. Bioinspired applications of porphyrin derivatives. *Accounts of chemical research*, 54(9):2249–2260, 2021.

[125] Shujie Liang, Xiaohui Zhong, Zuqi Zhong, Bin Han, Weiyi Chen, Kainan Song, Hong Deng, and Zhang Lin. Biomimetic inspired porphyrin-based nanoframes for highly efficient photocatalytic $CO_2$ reduction. *Chemical Engineering Journal*, 411:128414, 2021.

[126] Hiroshi Imahori. Porphyrin–fullerene linked systems as artificial photosynthetic mimics. *Organic & Biomolecular Chemistry*, 2(10):1425–1433, 2004.

[127] Jessica S O'Neill, Lauren Kearney, Michael P Brandon, and Mary T Pryce. Design components of porphyrin-based photocatalytic hydrogen evolution systems: A review. *Coordination Chemistry Reviews*, 467:214599, 2022.

[128] J Spencer Baskin, Hua-Zhong Yu, and Ahmed H Zewail. Ultrafast dynamics of porphyrins in the condensed phase: I. free base tetraphenylporphyrin. *The Journal of Physical Chemistry A*, 106(42):9837–9844, 2002.

[129] So Young Kim and Taiha Joo. Coherent nuclear wave packets in Q states by ultrafast internal conversions in free base tetraphenylporphyrin. *The journal of physical chemistry letters*, 6(15):2993–2998, 2015.

[130] Hua-Zhong Yu, J Spencer Baskin, and Ahmed H Zewail. Ultrafast dynamics of porphyrins in the condensed phase: II. zinc tetraphenylporphyrin. *The Journal of Physical Chemistry A*, 106(42):9845–9854, 2002.

[131] P Hemant Kumar, Yeduru Venkatesh, Doddi Siva, B Ramakrishna, and Prakriti Ranjan Bangal. Ultrafast relaxation dynamics of 5, 10, 15, 20-meso-tetrakis pentafluorophenyl porphyrin studied by fluorescence up-conversion and transient absorption spectroscopy. *The Journal of Physical Chemistry A*, 119(8):1267–1278, 2015.

[132] Masahiko Taniguchi, Jonathan S Lindsey, David F Bocian, and Dewey Holten. Comprehensive review of photophysical parameters ($\varepsilon$, $\phi$f, $\tau$s) of tetraphenylporphyrin ($H_2$TPP) and zinc tetraphenylporphyrin (ZnTPP)–critical benchmark molecules in photochemistry and photosynthesis. *Journal of Photochemistry and Photobiology C: photochemistry reviews*, 46:100401, 2021.

[133] A Mokhtari, J Chesnoy, and A Laubereau. Femtosecond time-and frequency-resolved fluorescence spectroscopy of a dye molecule. *Chemical physics letters*, 155(6):593–598, 1989.

[134] Hitoshi Sumi and RA Marcus. Dynamical effects in electron transfer reactions. *The Journal of chemical physics*, 84(9):4894–4914, 1986.

[135] Hua-Wei Jiang, Takayuki Tanaka, Hirotaka Mori, Kyu Hyung Park, Dongho Kim, and Atsuhiro Osuka. Cyclic 2, 12-porphyrinylene nanorings as a porphyrin analogue of cycloparaphenylenes. *Journal of the American Chemical Society*, 137(6):2219–2222, 2015.

[136] RF Khairutdinov and N Serpone. Photoluminescence and transient spectroscopy of free base porphyrin aggregates. *The Journal of Physical Chemistry B*, 103(5):761–769, 1999.

[137] Didjay F Bruggeman, Annechien AH Laporte, Remko J Detz, Simon Mathew, and Joost NH Reek. Aqueous biphasic dye-sensitized photosynthesis cells for tempo-based oxidation of glycerol. *Angewandte Chemie International Edition*, 61(21):e202200175, 2022.

[138] Sheng Ye, Wenwen Shi, Yong Liu, Dongfeng Li, Hang Yin, Haibo Chi, Yaling Luo, Na Ta, Fengtao Fan, Xiuli Wang, et al. Unassisted photoelectrochemical cell with multimediator modulation for solar water splitting exceeding 4% solar-to-hydrogen efficiency. *Journal of the American Chemical Society*, 143(32):12499–12508, 2021.

[139] Elisabetta Benazzi, Karin Rettenmaier, Thomas Berger, Stefano Caramori, Serena Berardi, Roberto Argazzi, Maurizio Prato, and Zois Syrgiannis. Photoelectrochemical properties of $SnO_2$ photoanodes sensitized by cationic perylene-diimide aggregates for aqueous HBr splitting. *The Journal of Physical Chemistry C*, 124(2):1317–1329, 2019.

[140] Eric Daniel Głowacki, Mihai Irimia-Vladu, Martin Kaltenbrunner, Jacek Gsiorowski, Matthew S White, Uwe Monkowius, Giuseppe Romanazzi, Gian Paolo Suranna, Piero Mastrorilli, Tsuyoshi Sekitani, et al. Hydrogen-bonded semiconducting pigments for air-stable field-effect transistors. *Advanced Materials*, 25(11):1563–1569, 2013.

[141] Eric Daniel Głowacki, Lucia Leonat, Mihai Irimia-Vladu, Reinhard Schwödiauer, Mujeeb Ullah, Helmut Sitter, Siegfried Bauer, and Niyazi Serdar Sariciftci. Intermolecular hydrogen-bonded organic semiconductors—quinacridone versus pentacene. *Applied Physics Letters*, 101(2):023305, 2012.